Development of measurement procedures and analysis of data from non-destructive tests for the survey of materials and components

Original Citation:

Development of measurement procedures and analysis of data from non-destructive tests for the survey of materials and components / Tamborrino, Rosanna. - ELETTRONICO. - (2019). [10.60576/poliba/iris/tamborrino-rosanna_phd2019]

Published version

Politecnico di Bari

DOI:10.60576/poliba/iris/tamborrino-rosanna_phd2019

Department of Mechanics, Mathematics and Management
MECHANICAL AND MANAGEMENT ENGINEERING
Ph.D. Program
SSD: ING-IND/12– Mechanical and Thermal Measurement

Final Dissertation

DEVELOPMENT OF MEASUREMENT PROCEDURES AND ANALYSIS OF DATA FROM NON-DESTRUCTIVE TESTS FOR THE SURVEY OF MATERIALS AND COMPONENTS

---

by
Tamborrino Rosanna :

Referees:

Prof. Gianluca Rossi

Prof. Riccardo Nobile

Supervisors:

Prof. Gaetano Vacca

Prof. Umberto Galietti

Coordinator of Ph.D Program:
Prof. Giuseppe Pompeo Demelio

Course n°31, 01/11/2015-31/10/2018

Contents

Table of Figures

Table of Tables

Part I

Background Theory

1. Introduction

Infrared thermography is a fast, clean and safe technology that is used in a wide variety of applications. Thermography has a number of approaches differing in experiment setup, thermographic technique applied and the way the collected data are processed. Infrared thermography is highly dependent on the sensor selection and the experimental setup. Adequate setup and testing procedures are necessary to avoid questionable results in the thermographic investigation.

This thesis addresses the problems of making the right choices for each specifically application.

The thesis includes the works developed and presented in five different scientific papers.

Paper 1 deals with the use of thermography, specifically lock-in thermography (LT), for the identification of defects in adhesively bonded joints.

Paper 2 describes the use of lock-in thermography for the investigation of dynamic thermal behavior of opaque building elements.

Paper 3, 4 and 5 have explored the use of "short" and "long" pulsed thermography for the detection of disbonds and for the measurement of the thickness in two different type of coating.

This introductory chapter provides a motivation for the thesis as well as describes its contributions and outline.

1.1. Motivation

Infrared thermography, in recent times, has invaded an increasing number of new applications in our everyday lives. It is based on the study of temperature distribution and its evolution with time on the surface of the sample of interest. In most cases, the term "thermography" refers to the so-called "active" thermographic approach. Active thermography assumes the study of those temperature distributions which are induced by application of an external thermal impact, in contrast to "passive" thermography which generally deals with objects which are heated by natural sources or by other heat heat [1].

This often makes the active thermography the only possible thermographic approach for the study of objects with no internal heat sources (e.g., composite and plastic panels for automotive and aeronautic applications). Active thermographic inspection requires two basic components: (a) thermal sensor and (b) the source of thermal impact. Although almost any thermal sensing device is applicable for use in thermographic experiments, modern thermography is generally performed with the use of thermal imagers (cameras). Thermal cameras allow one to obtain two-dimensional images showing the spatial distribution of temperature on the visible surface of the sample under analysis. Modern thermal cameras allow for the fast acquisition of such images, which creates possibilities for a large spectrum of potential experiments.

The second component of a thermographic set up is the source of thermal influence. The primary function of this component is to bring the object of interest out of thermal equilibrium and initiate heat flows and temperature re-distribution in the sample. While the temperature is forced to change, the thermal sensor collects information on this variation, and necessary conclusions are made from this information either with or without additional processing. From the practical point of view, the source of thermal influence is usually the source of heat: the most widely used sources are heat guns, lasers, and powerful xenon flash lamps. The choice of the source is highly dependent on the nature of the sample to be studied.

In the past few decades, thermography has found applications in numerous scientific fields and industries, paving the way from an exotic remote sensing method of non-destructive evaluation [2,3].

Modern thermographic techniques utilize fast and high precision devices for collection of data about the surface thermal distribution. At the same time, advanced computational processing of collected data is utilized in many modern thermographic approaches for extraction of qualitative and quantitative information on structure and integrity of studied objects. Among such techniques are well-known the approaches of short pulse thermography, lock in thermography, long pulse thermography, laser spot thermography and others [4, 5, 6, 7, 8, 9].

Most of these methods utilize various post-processing techniques in order to extract information regarding the structure and properties from the raw data on surface temperature distribution.

Even if the measuring chain is almost the same in real applications, each individual part of the measuring chain affects the relation between the source of the infrared radiation and the output signal of the measuring system.

The technological requirements regarding size, design, optical conditions, thermal and spatial resolution and many other framework conditions have to be diversified with respect to a selected experiment. This results in very complex issues that users must solve when trying to design optimum measuring arrangements or conditions. There are no simple rules and the problems cannot be solved without a basic understanding of the correlations.

Besides, different algorithms have to be specifically used to extract the right information from the collected data.

In this thesis, the feasibilities of experimentation using thermography are then introduced including the experimental setup. Software and data collection and processing methods used in the current work are introduced and the importance of various variables are studied. From this investigation knowledge of the importance of the experimental parameters is obtained and used in the remainder of experimental work.

1.2. Contribution

This thesis contains the following contributions:

- A thermographic procedure based on the “lock-in” thermographic technique applied to bonded composite joints: Paper A presents the results of an experimental activity and discussion to determine the capability and reliability of lock-in thermographic techniques as non-destructive testing for the debonding evaluation in glass-fiber reinforced plastic joints.
- European Standards specify the procedures to obtain information about the thermal behavior of building in terms of decrement factor and time lag, but these procedures are based on a theoretical approach: The results of an innovative experimental procedure based on the application of stimulated lock-in thermography with the aim of investigating the thermal dynamic behavior of walls are presented in Paper B.
- A new thermal data processing procedure, developed to investigate damages in composite materials, has been applied to evaluate adhesion defects of Thermal

Barrier Coatings (TBC). Moreover, an empirical thermographic method has been developed to evaluate the thickness of the thermal coating and to discriminate between an unevenness of the thickness and a defect zone. Paper C describes two different set up for implementing “short” and “long” pulsed thermography on TBC coating and a proper computational processing of collected data in order to extract quantitative information.

- The proposal of a specific thermographic procedure based on the “long pulse” thermographic approach for the measurement of the tungsten carbide coating thickness is presented in Paper D. To the knowledge of mine this technique has been never used for the evaluation of thickness for metal/metal configuration.
- Automatic Defect Detection from thermographic Non Destructive Testing: Paper E introduce a new processing technique of the thermographic data, obtained using the stepped thermography, for the detection of possible defects. The technique includes a series of enhancements of the linear fit of the log-log cooling time history of the specimen surface temperature. Besides, additional rigorous parameters will be proposed to accurately evaluate a defect.

1.3. Thesis Outline

The thesis is divided into two parts. The rest of Part I presents the background theory for Part II, containing edited versions of published and submitted papers. Parts of the material presented in Part I has already been published by the author in conference articles.

1.3.1. Outline Part I: Background Theory

Chapter 2 gives a brief overview of the physical principles related to thermal infrared imaging as well as provides information about its wide fields of application. The contents of Chapter 2 are relevant for all included papers in this thesis.

Chapter 3 (Measuring chain: individual parts and their effects) is constituted of two sections: Section 3.1 focus on characteristics of the IR camera, the thermal properties of tested material and the characteristic of the thermal source; Section 3.2 deals with data acquisition and data processing including the description of the most popular algorithms.

Finally, concluding remarks and future work are given in Chapter 4.

1.3.2. Outline Part II: Included Publications

Preprint versions of five papers are included in Part II. The full details and abstract of these papers are summarized below.

Paper A: Lock-in thermography for debonding evaluation of composite adhesive joints

Palumbo, D., Tamborrino, R., Galietti, U., Aversa, P., Tatì, A., & Luprano, V. A. M. (2016). Ultrasonic analysis and lock-in thermography for debonding evaluation of composite adhesive joints. NDT and E International, 78, 1–9. https://doi.org/10.1016/j.ndteint.2015.09.001

Abstract:

Glass-fiber reinforced thermosetting plastic adhesive joints were characterized through ultrasonic imaging and lock-in thermographic analysis for assessing the adhesion quality before being subjected to static tensile mechanical tests and to accelerated aging cycles.

The mapping of each sample has been obtained. Visual testing were performed on all specimens after the mechanical tests in order to obtain a comparison with ultrasonic and lock-in thermography technique.

A quantitative analysis has been carried out to evaluate the ability of lock-in thermography in investigating inadequate bonding and obtaining the validation of the technique by the consistency of the results with the well-established ultrasonic testing.

Paper B: Infrared thermography for the investigation of dynamic thermal behaviour of opaque building elements: Comparison between empty and filled with hemp fibres prototype walls

Aversa, P., Palumbo, D., Donatelli, A., Tamborrino, R., Ancona, F., Galietti, U., & Luprano, V. A. M. (2017). Infrared thermography for the investigation of dynamic thermal behaviour of opaque building elements: Comparison between empty and filled with hemp fibres prototype walls. Energy and Buildings, 152, 264–272. https://doi.org/10.1016/j.enbuild.2017.07.055

Abstract:

The analysis of the thermal dynamic behavior of buildings is an important tool for reducing inefficiencies and then wasted energy. In this field, European Standards specify the procedures to obtain information about the thermal behavior of building in terms of decrement factor and time lag. However, these procedures are based on a theoretical approach that does not take into account the real factors involved in the heat exchange phenomena such as the correct knowledge of thermo-physical parameters and the presence of non-homogeneous materials or defects in the investigated walls.

In this work, we propose an innovative experimental procedure based on the application of stimulated thermography with the aim of investigate the thermal dynamic behavior of walls. In particular, two prototype walls were compared: an empty wall and one made with an insulating filler of vegetable nature (hemp fibre).

The results were then compared with those obtained with a numerical simulation and with the Standard procedure EN ISO 13786:2007, highlighting the differences between the three approaches.

Paper C: Coating defect evaluation based on stimulated thermography

Palumbo D., Tamborrino R., Galietti U.. "Coating defect evaluation based on stimulated thermography", Proc. SPIE 10214, Thermosense: Thermal Infrared Applications XXXIX, 102140X (5 May 2017); doi: 10.1117/12.2267851; https://doi.org/10.1117/12.2267851

Abstract:

Barrier Coatings are used to protect the materials from severe temperature and chemical environments. In particular, these materials are used in the engineering fields where high temperatures, corrosive environments and high mechanical stress are required. Defects present between substrate material and coating, as detachments may cause the break of coating and the consequent possibility to exposure the substrate material to the environment conditions. The capability to detect the defect zones with non-destructive techniques could allow the maintenance of coated components with great advantages in terms of costs and prediction of fatigue life.

In this work, two different heat sources and two different thermographic techniques have been used to detect the adhesion defects among the base material and the coating. Moreover, an empirical thermographic method has been developed to evaluate the thickness of the thermal coating and to discriminate between an unevenness of the

thickness and a defect zone. The study has been conducted on circular steel specimens with simulated adhesion defect and on specimens prepared with different thicknesses of thermal barrier coating.

Paper D: A thermographic procedure for the measurement of the tungsten carbide coating thickness

Tamborrino R., D'Accardi E., Palumbo D., Galietti U.

Under review on Journal of Thermal Spray Technology (Springer)

Abstract:

Mechanical components subjected to severe environments are usually coat with cermet based WC–Co–Cr thermally sprayed coating. The coating plays a very important role in improving a component's survivability and operational performance. The coatings thickness is not only a parameter of the geometrical property of the coatings itself, but also an important indicator for evaluating the coatings' quality, performance and service life. The coating thickness needs to be controlled and mastered because it has a great influence on the final product performance. Non-destructive measuring techniques are indicated for coating thickness evaluation.

In this paper, a thermographic procedure based on the "long pulse" thermographic approach for the measurement of the tungsten carbide coating thickness has been proposed and a comparison has been made with the performance of the traditional flash excitation technique. A calibration has been performed to evaluate the thickness of the coating and a prediction model has been proposed.

Paper E: Automatic Defect Detection from thermographic Non Destructive Testing

Dinardo G., Fabbiano L., Tamborrino R., Vacca G.
Submetted to II National Forum Of Measures

Abstract: In recent years, thermography has appeared particularly attractive among the nondestructive testing (NDT) methods for the detection of defects in materials. It offers the advantages of low cost, easy operation, high speed, and wide area coverage.

The most widely used form of thermographic NDT is the pulsed thermography in which the surface of a tested part is heated by a brief pulse of light usually from a high power source. Along with pulsed thermography, the step heating technique has recently received more attention. It is implemented by applying a thermal stimulation to a surface for more than few milliseconds. The time-dependent surface temperature response is captured as a series of thermal images by an infrared camera. The temperature contrast between the defective and non-defective regions enables the defect detection based on thermographic data. However, thermal images usually involve significant measurement noise and non-uniform backgrounds caused by uneven heating. Hence, different types of thermographic image analysis methods have been proposed for signal enhancement.

In this paper, the authors introduce a new processing technique of the thermographic data, obtained using the stepped thermography, for the detection of possible defects. The technique includes a series of enhancements of the linear fit of the log-log cooling time history of the specimen surface temperature. Basically, the algorithm is directly applied to the thermographic images indicating the temperature trend of each pixel. The slope (m) of the linear fit of the log-log of the surface temperature time history is going to be used as a primary indicator of the location and size of the defects. The idea inspiring this work is to significantly enhance the fit, adopting optimization techniques to better utilize the spatial information coming from the thermographic data. Besides, additional rigorous parameters will be proposed to accurately evaluate a defect.

1.4. Other Publications

The following publications by the author are related to the included papers and to the conducted research activity .

Tamborrino, R., Palumbo, D., Galietti, U., Aversa, P., Chiozzi, S., & Luprano, V. A. M. (2016). Assessment of the effect of defects on mechanical properties of adhesive bonded joints by using non destructive methods. Composites Part B: Engineering, 91, 337–345. https://doi.org/10.1016/j.compositesb.2016.01.059

D'Accardi, E., Palumbo, D., Tamborrino, R., & Galietti, U. (2018). Quantitative analysis of thermographic data through different algorithms. Procedia Structural Integrity, 8, 354–367. https://doi.org/10.1016/j.prostr.2017.12.036

D'Accardi E., Palumbo D., Tamborrino R. Galietti U. (2018). A quantitative comparison among different algorithms for defects detection on aluminium with the

Pulsed Thermography technique. Metals 2018, 8(10), 859; https://doi.org/10.3390/met8100859.

D'Accardi E., Palano F., Tamborrino R., Palumbo D., Tatì A., Terzi R., Galietti U. (2018). Capability of Pulse Phase Thermography in Evaluating Delamination in CFRP by Ultrasonic Technique Validation. Accepted by Journal of Nondestructive Evaluation.

Bibliography

[1] Gavrilov, D., & Maev, R. (2018). Extraction of Independent Structural Images for Principal Component Thermography. Applied Sciences, 8(3), 459. https://doi.org/10.3390/app8030459

[2] Vavilov, V. Thermal Non-Destructive Testing: Short History, State-of-the-Art and Trends. In Proceedings of the 10th European Conference on Non-Destructive Testing (ECNDT), Moscow, Russia, 7–11 June 2010

[3] Vavilov, V. Thermal non destructive testing: Short history and state-of-art. In Proceedings of the 1992 International Conference on Quantitative InfraRed Thermography (QIRT), Paris, France, 7–9 July 1992

[4] Delanthabettu, S.; Menaka, M.; Venkatraman, B.; Raj, B. Defect depth quantification using lock-in thermography. QIRT J. 2015, 12, 37–52

[5] Fedala, Y.; Streza, M.; Sepulveda, F.; Roger, J.-P.; Tessier, G.; Boué, C. Infrared lock-in thermography crack localization on metallic surfaces for industrial diagnosis. JNDE 2014, 33, 335–341

[6] Breitenstein, O.; Warta, W.; Langenkamp, M. Lock-in Thermography: Basics and Use for Evaluating Electronic Devices and Materials, 2nd ed.; Springer: Berlin/Heidelberg, Germany, 2010; pp. 22–26. ISBN 978-3-642-02416-0

[7] Nolte, P.; Malvisalo, T.; Wagner, F.; Schweiser, S. Thermal diffusivity of metals determined by lock-in thermography. QIRT J. 2017, 14, 218–225

[8] D'Accardi, E.; Palumbo, D.; Tamborrino, R.; Galietti, U. Quantitative analysis of thermographic data through different algorithms. Proc. Struct. Integr. 2018, 8, 354–367

[9] Ciampa, F.; Mahmoodi, P.; Pinto, F.; Meo, M. Recent Advances in Active Infrared Thermography for Non-Destructive Testing of Aerospace Components. Sensors 2018, 18, 609

2. The physics and application fields of infrared termography

Thermal infrared imaging or briefly thermography forms the basis of this thesis. The following chapter gives an overview of the applications and of the physics behind thermal infrared imaging. An in depth review of the main types of thermography that use the addition of energy from light sources is then presented.

2.1. Infrared thermography application fields

Infrared thermography (IRT) is a technology dedicated to the acquisition and processing of thermal information from non-contact measurement devices [1]. It is based on infrared radiation (below red), a form of electromagnetic radiation with longer wavelengths than those of visible light. Any object at a temperature above absolute zero (i.e., $T > 0K$) emits infrared radiation [2]. The human eye cannot see this type of radiation. Thus, infrared measuring devices are required to acquire and process this information [3].

Infrared measuring devices acquire infrared radiation emitted by an object and transform it into an electronic signal [4]. The most basic infrared device is a pyrometer, which produces a single output using a single sensor. Most advanced devices include an array of sensors to produce a detailed infrared image of the scene. The difference between a visible image and an infrared image is that the visible image is a representation of the reflected light on the scene, whereas in the infrared image, the scene is the source and can be observed by an infrared camera without light. Images acquired using infrared cameras are converted into visible images by assigning a color to each infrared energy level. The result is a false-color image called a thermogram [5].

IRT has many advantages over other technologies [6]. In general, the main advantages of IRT are the following:

- IRT is a non-contact technology: the devices used are not in contact with the source of heat, i.e., they are non-contact thermometers. In this way, the temperature of extremely hot objects or dangerous products, such as acids, can be measured safely, keeping the user out of danger.
- IRT provides two-dimensional thermal images, which make a comparison between areas of the target possible.

- IRT is in real time, which enables not only high-speed scanning of stationary targets, but also acquisition from fast-moving targets and from fast-changing thermal patterns.
- IRT has none of the harmful radiation effects of other technologies, such as X-ray imaging. Thus, it is suitable for prolonged and repeated use.
- IRT is a non-invasive technique. Thus, it does not intrude upon or affect the target in any way.

Due to all of these advantages, thermography has been established as an effective tool in many different applications [7]. However, IRT is not without its drawbacks. Fast and affordable hardware has recently become available, but an infrared camera is still an expensive device. Some very affordable models with a high enough spatial resolution for most applications have recently come onto the market. However, these inexpensive models with high spatial resolution provide lower accuracy, which makes them unusable for some applications. Infrared images can also be difficult to interpret; in general, specific training is required. IRT is also highly dependent on working conditions, such as the surrounding temperature, airflow or humidity. Therefore, IRT should be used in controlled environments.

The intensity of the infrared radiation emitted by objects is mainly a function of its temperature; the higher the temperature, the greater the intensity of the emitted infrared energy. Many different applications can take advantage of this feature [8]. Some of the main fields where infrared thermography is used include medicine [9], veterinary medicine [10], maintenance and process monitoring [11], building inspection [12] and non-destructive testing [13].

Maintenance is an area where IRT is successfully applied [14]. The electrical field, the mechanical field and insulation are three of the most common areas where IRT is used. IRT is used in electrical and mechanical maintenance to detect early signs of malfunction, so costly breakdowns can be avoided. In the electrical field, abnormal temperature patterns can indicate faulty connections [15], whereas in the mechanical field, they can indicate excessive friction due to improper lubrication or material fatigue [16,17]. In the insulation field, IRT is used to detect hidden losses of heat that can drain performance and increase costs [18]. IRT is also used in other areas of the maintenance and process monitoring field, such as monitoring of plastic deformations [19,20], evaluation of fatigue damage in materials [21], weld inspection [22] and identification of kissing defects in adhesive bonds [23].

Another area where IRT is successfully applied is building inspection. The temperature distribution on the facade of a building provides very useful information to discover many hidden conditions related to the building performance and maintenance [24]. For example, it can be used to detect where and how energy is leaking from a building envelope. Besides the detection of heat loss, IRT is also used to discover other anomalies, such as water infiltration and moisture [25,26]. A wet mass in a wall has a differentiated thermal inertia that can be discovered using IRT. Recent applications of IRT for moisture detection can be found in [27] and [28], which use IRT for sub-surface moisture detection in masonry structures and for moisture mapping in ancient buildings, respectively. Moisture detection using IRT is not limited to buildings. It can also be applied to paper [29], soil [30] or aircraft structures [31].

The presence of water inside aircraft structures may lead to ice formation with a volume variation and consequent mechanical stresses [32].

Two different approaches are employed in IRT: passive and active. In passive IRT, the radiation coming from the target object is measured without any external heat stimulation. This information can be used for temperature measurement. On the other hand, in active IRT, the specimen is subjected to external thermal stimulation [33]. The heat propagation depends on the material's thermal properties, but also on subsurface anomalies, which result in temperature differences on the surface target. In this case, the measured radiation comes from the thermal response of the target to the external excitation.

Passive IRT is used in quality control and process monitoring applications. Temperature plays a crucial role in any industrial process. Thus, temperature measurement and monitoring during and after the industrial process is critical to achieve optimal results. However, the computation of temperature from infrared images is not only based on measured radiation; it also depends on the internal camera calibration, as well as on the emissivity of the object radiating energy. Thus, a calibration setup is required to obtain accurate measurements.

Active IRT is mostly used in non-destructive testing applications, where an external stimulus is applied to the specimen in order to induce relevant thermal contrasts between regions of interest [34]. It is applied to the inspection of materials for subsurface defect detection and also to detect areas of the specimen with different properties below the surface [35]. Some subsurface anomalies are very subtle. Therefore, the signal levels associated with them can be lost in the thermographic data noise [36]. In these cases, different post-processing methods can be used to improve the signal-to-noise (SNR) content of thermographic data.

2.2. Physics of the Infrared Thermography

Infrared radiation is the energy radiated by the surface of an object whose temperature is above absolute zero. There are three ways by which the radiant energy striking an object may be dissipated: absorption, transmission and reflection. The fractions of the total radiant energy that are associated with each of these modes of dissipation are referred to as the absorptivity, transmissivity and reflectivity of the body [37]. Three parameters are used to describe these phenomena: the spectral absorptance α_λ, which is the fraction of the spectral radiant power absorbed by the object, the spectral reflectance ρ_λ, which is the fraction of the spectral radiant power reflected by the object, and the spectral transmittance τ_λ, which is the fraction of the spectral radiant power transmitted by the object. These three parameters are wavelength dependent. The sum of these three parameters must be one at any wavelength, as in Equation (1):

$$\alpha_\lambda + \rho_\lambda + \tau_\lambda = 1 \tag{1}$$

In the case of opaque materials, Equation (1) is simplified by Equation (2), that is, all of the striking energy is either absorbed or reflected. It could also be said that the striking energy that is not absorbed is reflected.

$$\alpha_\lambda = 1 - \rho_\lambda \tag{2}$$

Materials in which the transmissivity and the reflectivity are null are called blackbodies. In these materials, all of the striking radiant energy is absorbed ($\alpha_\lambda = 1$).

Electromagnetic radiation emitted from a blackbody ($W_{\lambda b}$) can be calculated using Planck's law, as in Equation (3), where C_1 and C_2 are constants, λ is the wavelength and T is the temperature. The result of Plank's law is the power emitted per unit area per unit wavelength, which is a function of λ and T.

$$W_{\lambda b} = \frac{C_1 \lambda^{-5}}{e^{\frac{C_2}{\lambda T}} - 1} \tag{3}$$

Figure 2.2-1 shows the distribution of electromagnetic radiation emitted by a blackbody at different temperatures. The curves show how much energy is radiated at each wavelength. As it can be seen, the peak of the curve for a hotter object is larger. In addition, there is an inverse relation between the temperature and the wavelength of the peak of the emission.

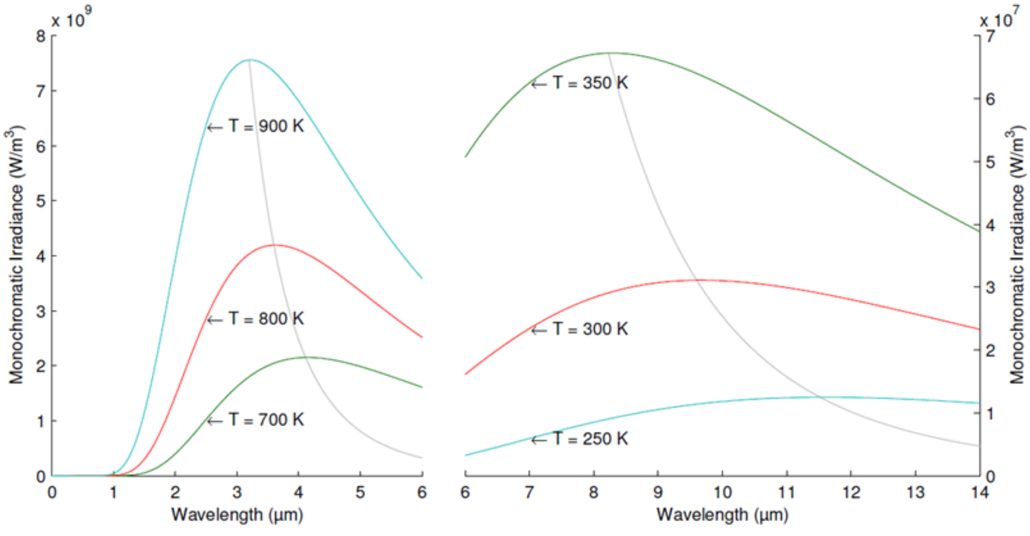

(a) (b)

Figure 2.2-1 : Planck's law: electromagnetic radiation emitted by a blackbody in thermal equilibrium at a definite temperature. (a) Objects with a high temperature emit most of the radiation in the middle wave infrared; (b) Objects with a low temperature emit most of the radiation in the long wave infrared. The two parts of the graph are scaled differently on the y-axis [38].

The wavelength at which electromagnetic radiation is emitted depends on the temperature of the object; the higher the temperature, the shorter its wavelength. The distribution is similar, but the wavelength is displaced. The peak wavelength for a specific temperature value can be calculated using Wien's law, Equation (4). Figure 2.2-2 shows a graphical representation of the relation between peak wavelength and temperature using a logarithmic scale. Wien's law is obtained by differentiating the Planck's law Equation (3) with respect to λ and by finding the maximum radiation intensity.

$$\lambda_{peak} = \frac{0.0029}{T} \tag{4}$$

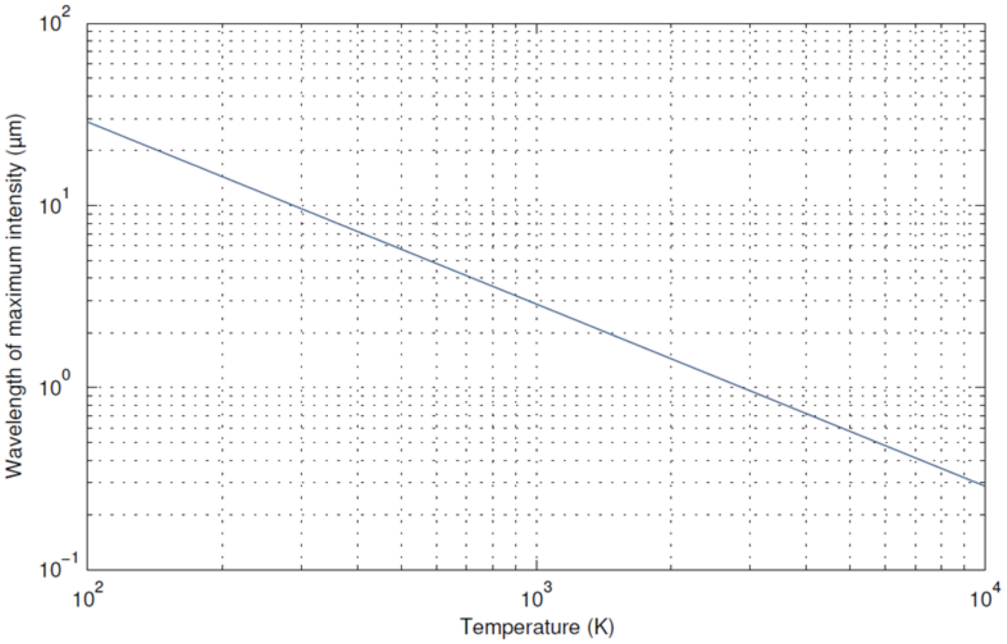

Figure 2.2-2: Wien's displacement law: the wavelength of the maximum radiation intensity by a blackbody at a given temperature [38].

In order to obtain the total hemispherical radiation intensity of a blackbody, Equation (3) is integrated through all wavelengths (λ from zero to infinity), obtaining Equation (5), where σ is a constant. This is called the Stefan–Boltzmann formula.

$$W_b = \sigma T^4 \tag{5}$$

The emissivity of a body is defined formally for a wavelength λ by Equation (6), as the ratio of the radiant energy emitted by the body to the radiation that would be emitted by a blackbody at the same temperature.

$$\varepsilon_\lambda = \frac{W_\lambda}{W_{\lambda \mathrm{b}}} \tag{6}$$

A real body emits only a fraction of the thermal energy emitted by a blackbody at the same temperature. If the emissivity is constant and independent of the wavelength, the body is a greybody. Thus, it can be expressed by Equation (7):

$$\varepsilon_\lambda = \frac{W_\lambda}{W_{\lambda \mathrm{b}}} = \frac{W}{W_b} = \varepsilon \tag{7}$$

The emissivity of real objects is not constant nor independent of the wavelength; thus, they cannot be considered greybodies. However, it is usually assumed that for short wavelength intervals, the emissivity can be considered as a constant. This assumption is used to treat real objects as greybodies. Thus, although the emissivity of real objects is wavelength dependent, and, therefore, they cannot be considered true greybodies, they are treated as such by averaging their emissivity through short intervals, in which the infrared sensor works. This average is also possible because the emissivity is a slow varying function of wavelength for solid objects. However, this does not apply to other cases, such as gases or liquids.

Combining Equation (7) and (5), Equation (8) is obtained. This equation is the Stefan–Boltzmann formula for greybody radiators. Figure 2.2-3 shows a graphical representation of this formula for different emissivities.

$$W = \varepsilon \sigma T^4 \tag{8}$$

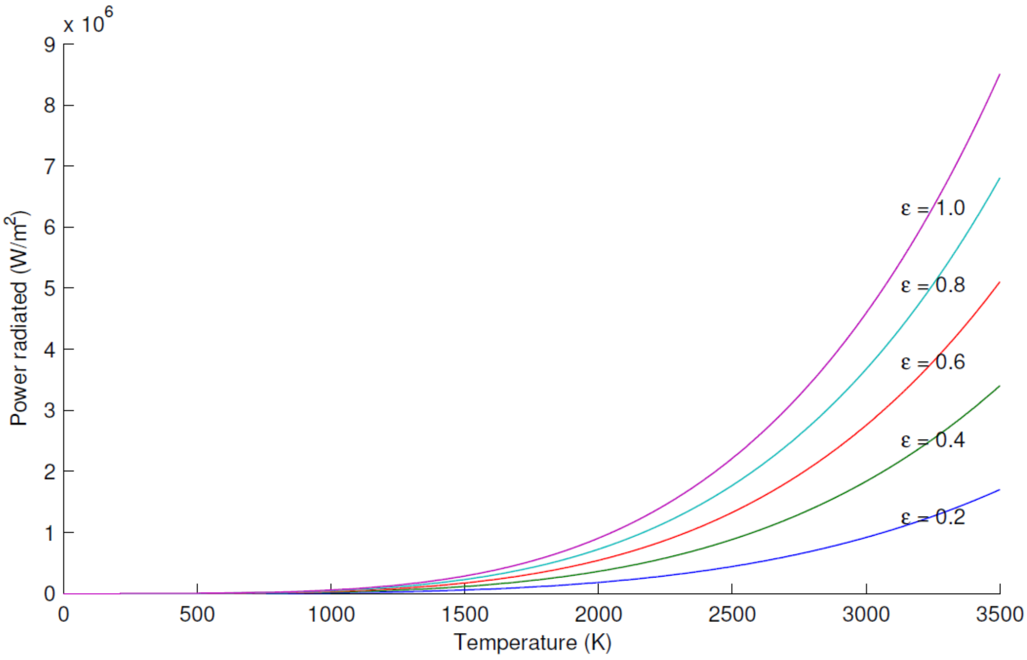

Figure 2.2-3: Stefan–Boltzmann law: power radiated by a greybody with different emissivities [38].

If all of the radiation energy falling on an object is absorbed (no transmission or reflection), the absorptivity is one. At a steady temperature, all of the energy absorbed must be re-radiated (emitted), so that the emissivity of such a body would be one. Therefore, the absorptivity in a blackbody is equal to emissivity, which is one. In general, according to Kirchhoff's law, the emissivity and absorptivity of any material are equal at any specified temperature and wavelength. This can be expressed as:

$$\varepsilon_\lambda = \alpha_\lambda \tag{9}$$

From Equations (9) and (2), Equation (10) is obtained for opaque materials.

$$\rho_\lambda = 1 - \varepsilon_\lambda \tag{10}$$

Greybodies emit only a fraction of the thermal energy emitted by an equivalent blackbody; therefore, emissivity in these bodies is always less than one and reflectivity greater than zero [38].

The electromagnetic spectrum is divided into several regions or bands according to the wavelength. Regions are not sharply defined, and they differ in different disciplines. The infrared region is approximately defined from 0.8 μm to 1000 μm, that is, from the end of visible light to microwaves. Much of the infrared range of the electromagnetic spectrum is not useful in IRT, because it is blocked by the atmosphere. The remaining portions define the usable part of the infrared by IRT:

- Near-infrared (NIR) from 0.8 μm to 1.7 μm.
- Short-wavelength infrared (SWIR) from 1 μm to 2.5 μm.
- Mid-wavelength infrared (MWIR) from 2 μm to 5 μm.
- Long-wavelength infrared (LWIR) from 8 μm to 14 μm.

Of all of these regions, MWIR and LWIR are the most commonly used in IRT. There are two reasons: the band of peak emissions and atmospheric transmittance. The first reason is due to the relation between temperature and wavelength. The most effective measurement for a particular temperature should be carried out for the wavelength at which most intensity is emitted (see Figure 1). Measuring at a different wavelength would require a much more sensitive camera to achieve identical performance. Thus, for most applications, wavelengths longer than SWIR are required. The second reason is related to the atmospheric transmittance. Infrared radiation travels through air, being absorbed by various air particles, mostly by CO_2 and H_2O [3]. The degree to which air absorbs infrared radiation depends on the wavelength. In the MWIR and LWIR bands, this absorption is low, allowing more radiation to reach the sensor of the camera.

Figure 2.2-4 shows the atmospheric transmittance for different wavelengths. As can be seen, in the visible part of the spectrum, from 0.4 μm to 0.7 μm, only 60% of the emitted radiation is transmitted. However, between 5 μm and 7.5 μm, almost no radiation is transmitted. The atmosphere absorbs all of this radiation. Therefore, infrared measuring devices use either MWIR or LWIR. MWIR devices are used for high-temperature readings, while LWIR is used for ambient temperatures.

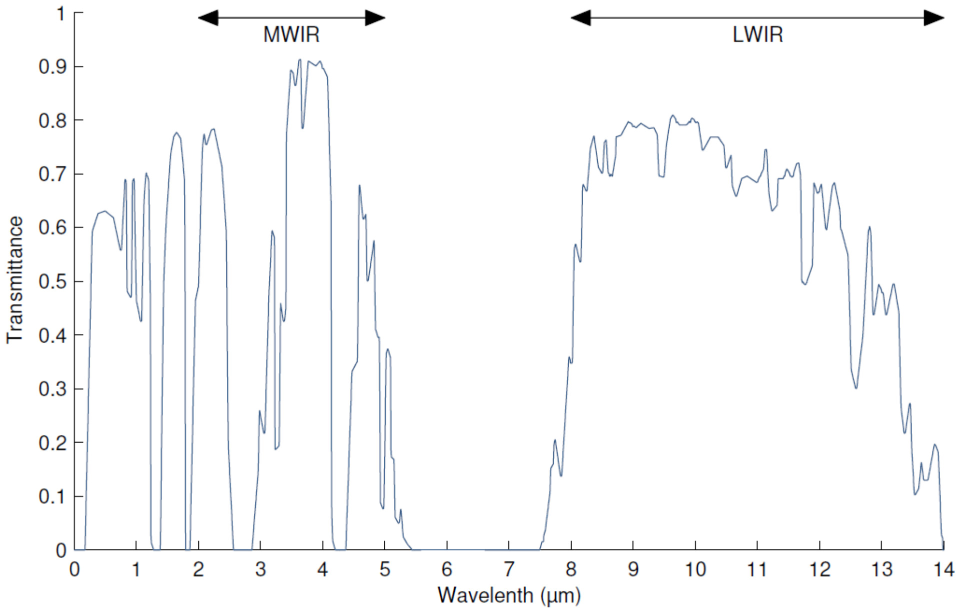

Figure 2.2-4: Atmospheric transmittance at one nautical mile, 15.5 C, 70% relative humidity and at sea level [38].

2.3. Thermographic tecniques

For the studies conducted in this research path, active thermography has been used. Contrary to passive thermography, active thermography requires an external heat sources to stimulate the materials under tests. The common types of active thermography are pulsed thermography (PT), stepped or long pulsed thermography (ST), lock-in thermography (LT) or called modulated thermography (MT), if a classification by heating function is made:

- Lock-in thermography
- Pulsed thermography
- Long pulsed thermography

PT warms or cools the material with a short duration energy pulse and a measurement of the temporal evolution of the surface temperature is performed with an IR camera.
With ST, a long pulse is used to step heat the sample and the temperature's rising and/or falling process is observed. LT uses periodic thermal excitation in order to derive information on reflected thermal wave phase and magnitude even at considerably low peak powers.
Thermal source used in active thermography testing is various, such as optical excitation, electromagnetic excitation, acoustic excitation, and stress/strain excitation.

According to excitation sources, thermography can be classified as: (1) Optical thermography using optical excitation such as flash and lamp, which is named laser thermography if using laser beam as thermal source; (2) Eddy current thermography (ECT), which uses induced eddy current as thermal sources to heat conductive materials; (3) Conduction thermography which uses electrical current as sources; (4) Magnetic induction thermography, which uses magnetic field as heat source for ferromagnetic materials; (5) Microwave thermography (MWT), which uses microwave as heat source for dielectric materials; (6) Vibrothermography using mechanical variation as excitation, which is named as ultrasound thermography (UT) if using ultrasound as excitation; and (7) Thermoelastic stress analysis, which use strain or stress as heat sources. Every thermography mentioned above can be applied as PT, ST, LT.

The reported cases of study regard the use of optical thermography and so the description of optical sources will be reported in the measurement chain.

2.3.1. Lock-in thermography

Lock-in thermography (LT) also known as modulated thermography [39] is a technique derived from photothermal radiometry [40], in which, a small surface spot is periodically illuminated by an intensity modulated laser beam to inject thermal waves into the specimen. The thermal response is recorded at the same time using an infrared detector and decomposed by a lock-in amplifier to extract the amplitude and phase of the modulation [41]. Photothermal radiometry was a raster point-by point technique that required long acquisition times (especially in the case of deep defects involving very low modulation frequencies, see below). Furthermore, extra hardware, i.e. lock-in amplifier, is needed in order to retrieve the amplitude and phase of the response.

Fortunately, it is possible to drastically simplify and speed up the acquisition process for NDT applications by replacing: (1) the laser beam with one or several modulated heating sources, e.g. halogen lamps, that cover the entire specimen surface instead of only a point; (2) the infrared detector with an infrared camera capable of monitoring the whole (or a large part of the) surface; and (3) the lock-in hardware with a software capable of recovering mathematically the amplitude and phase of the response. This is what is called lock-in thermography [42].

Sinusoidal waves are typically used in LT, although other periodic waveforms are possible. Using sinusoids as input has the advantage that the frequency and shape of the response are preserved; only the amplitude and phase delay of the wave may change (i.e. sinusoidal fidelity). The periodic wave propagates by radiation through the air until it touches the specimen surface where heat is produced and propagates through the material. Internal defects act as a sort of filter for heat propagation, which produces changes in amplitude and phase of the response signal at the surface.

Heat diffusion through a solid is a complex 3D problem that can be described by the Fourier's law of heat diffusion (or the heat equation) [43]:

$$\nabla^2 T - \frac{1}{\alpha}\frac{\partial T}{\partial t} = 0 \tag{11}$$

where $\alpha = {}^{K}\!/_{\rho c_p}$ [m^2/s] is the thermal diffusivity of the material being inspected, k [W/mK] its thermal conductivity, ρ [kg/m^3] its density and c_p [J/kgK] its specific heat at constant pressure.

The Fourier's law 1D solution for a periodic thermal wave propagating through a semi-infinite homogeneous material may be expressed as:

$$T(z,t) = T_0 exp\left(-\frac{z}{\mu}\right) cos\left(\frac{2\pi z}{\lambda} - \omega t\right) \tag{12}$$

where T_0 [°C] is the initial change in temperature produced by the heat source, $\omega = 2\pi f$[rad/s] is the modulation frequency, f [Hz] is the frequency, $\lambda \equiv 2\pi\mu$ [m] is the thermal wavelength; and μ [m] is the thermal diffusion length, which determines the rate of decay of the thermal wave as it penetrates through the material, defined by [44]:

$$\mu \equiv \sqrt{\frac{2\alpha}{\omega}} = \sqrt{\frac{\alpha}{\pi f}} \tag{13}$$

Figure 2.3-1 depicts a thermal wave as it travels from the surface through a solid. As can be seen, after the waveform travels only a distance equal to a thermal diffusion length μ, its initial intensity has been already reduced to 1/535.

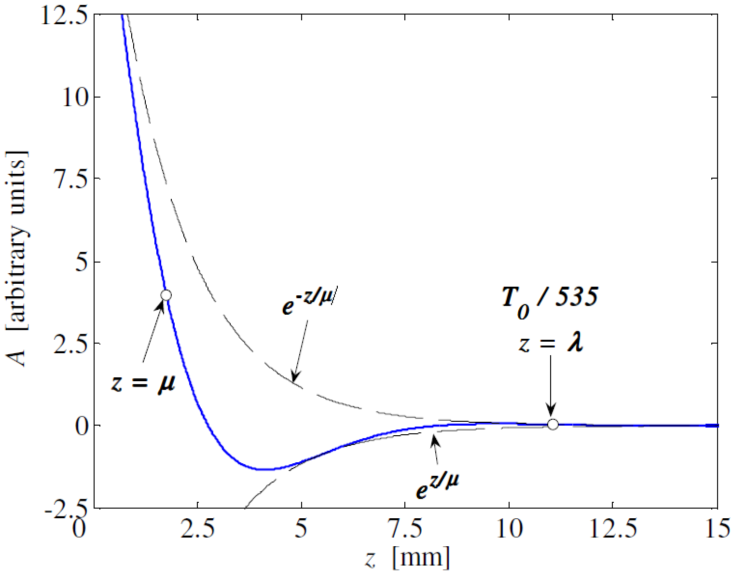

Figure 2.3-1: Thermal wave propagation by conduction through an aluminum semi-infinite plate at 10 Hz [55].

From Eq. (13), in order to cover a distance equal to a thermal wavelength l, a thermal wave at f=10 Hz will be able to travel less than 0.4 mm through plastic, slightly more than 11 mm through aluminum (see Figure 2.3-1) and almost 16 mm through air. Hence, thermal waves propagate deeper in more diffusive materials. On the other hand, information about deeper features are available when lower frequencies are used.

These two aspects are important to know when planning the inspection of a part in order to correctly select the working frequency and to determine the depth of internal defects. The experimental setup and more details of the acquisition system in more detail will be described in the paragraph 3.6.1.

2.3.2. Pulsed thermography

In pulsed thermography (PT), the specimen surface is submitted to a heat pulse using a high power source. A heat pulse can be though as the combination of several periodic waves at different frequencies and amplitudes. After the thermal front hits the specimen’s surface, a thermal front travels from the surface through the specimen. From that instant, the surface temperature will uniformly decrease in time for a sample without internal flaws. On the contrary, subsurface discontinuities (e.g. porosity, delaminations, disbonds, detachments, fiber breakage, inclusions, etc.), can be thought as resistances to the heat flow so producing abnormal temperature patterns at the surface, which can be detected with an IR camera.

The 1D solution of the Fourier equation for the propagation of a Dirac heat pulse (i.e. an ideal waveform defined as an intense unit-area pulse of so brief duration that no measuring equipment is capable of distinguishing it from even shorter pulses [45]) in a semi-infinite isotropic solid by conduction has the form [43]:

$$T(z,t) = T_0 + \frac{Q}{\sqrt{k\rho c_p \pi t}} exp\left(-\frac{z^2}{4\alpha t}\right) \tag{14}$$

where *Q,* is measured in [J/m2], is the energy absorbed by the surface and T_0 [K] is the initial temperature.

A Dirac heat pulse is composed of periodic waves at all frequencies and same amplitude. Although it is not possible to reproduce such a waveform in practice, a heat pulse provided by a powerful source such as a photographic flash having approximately a square shape, can be used. In this case, the signal is composed by periodic waves at several (3 or 4 generally) frequencies with decreasing amplitudes. The shorter the pulse, the broader the range of frequencies is.

From Eq. (14), the thermal profiles for an aluminum specimen subjected to a uniform heat pulse follows the behavior depicted in Figure 2.3-2.

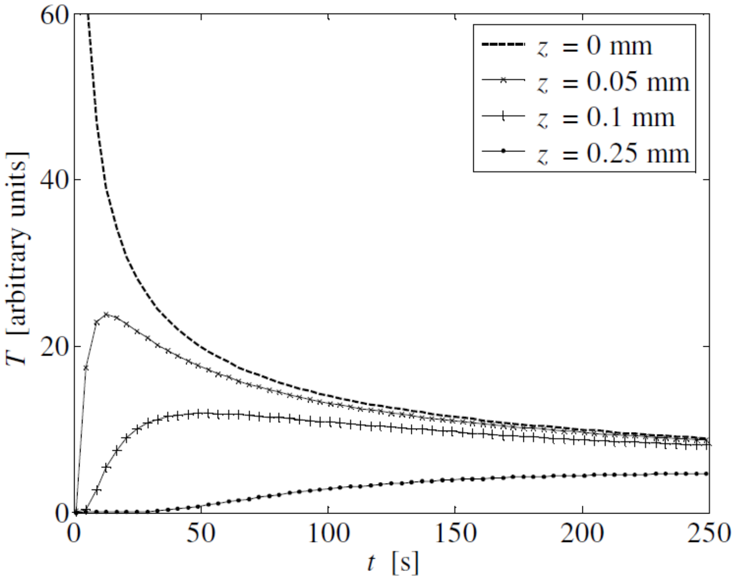

Figure 2.3-2: Thermal profiles at four depths (z = 0, 0.05, 0.1 and 0.25 mm) for an aluminum plate subjected to a uniform heat pulse.

The profiles correspond to 4 depths: z = 0, 0.05, 0.1 and 0.25 mm. Thermal evolution for deep defects starts at zero and reaches peak intensity at a given time (longer for deeper defects) and then slowly decays approximately as the square root of time.

Shallower defects show higher peak intensities earlier. At the surface the behavior is somehow different starting at a high temperature and monotonically decaying following approximately the square root of time. At the surface (z = 0 mm), Eq. (14) can be rewritten as follows:

$$T(0,t) = T_0 + \frac{Q}{e\sqrt{\pi t}} \tag{15}$$

where $e \equiv \left(k\rho c_p\right)^{1/2}$, measured in m, is the effusivity, which is a thermal property that measures the material ability to exchange heat with its surroundings.

Although Eq. (15) is only an approximation of the complex 3D diffusion problem described by Fourier's law, i.e. Eq. (11), many of the processing techniques have been based on this simplification to perform qualitative and quantitative analysis, as will be discussed in paragraph 3.7.2 The experimental setup is discussed first in paragraph 3.6.2.

2.3.3. Long pulsed thermography

Long Pulse Thermography also known as Square Pulse Thermography is defined as Pulse Thermography with relative long heating excitation period, typically at least a couple of seconds of heating compared to the traditional Pulse Thermography. The technique was introduced to extend the Pulse Thermography analysis of results. Long Pulsed Thermography is suitable for materials that required long pulsation such as buildings, plastics and thick composites. It can also be used to detect subsurface defects such as cracks, delamination, impact damage and moisture ingress or content in the aerospace and aircraft industries [46]. Generally, the technique can be processed to improve defect visibility and perform qualitative studies of defects.

Many workers in the field are aware that this long pulse excitation technique can be effective for some favourable applications. The technique has a long history [47–49] and it is offered by some commercial companies [50,51]. However, there appears to have been little detailed study of the capabilities of thermographic NDE employing this "long pulse" mode of thermal stimulation. Here we must distinguish between long pulse thermography and step heating thermography that has received more attention [52–54]in the last years . In long pulsed thermography, heating is applied for a selected period of time, i.e. 5 s, and then thermal images are collected as the test sample cools down. In step heating thermography, thermal images are collected whilst the test specimen is heated up.

Bibliography

[1] Maldague, X. Theory and Practice of Infrared Technology for Nondestructive Testing; Wiley: New York, NY, USA, 2001.

[2] Modest, M.F. Radiative Heat Transfer; Academic Press: Waltham, MA, USA, 2013.

[3] Vollmer, M.; M¨ollmann, K.P. Infrared Thermal Imaging: Fundamentals, Research and Applications; Wiley: Weinheim, Germany, 2011.

[4] Zissis, G.J.; Wolfe, W.L. The Infrared Handbook. Technical report, DTIC document, 1978.

[5] Gaussorgues, G. Infrared Thermography; Springer: Berlin/Heidelberg, Germany, 1994.

[6] Gade, R.; Moeslund, T.B. Thermal cameras and applications: A survey. Mach. Vision Appl. 2014, 25, 245–262.

[7] Meola, C. Infrared Thermography: Recent Advances and Future Trends; Bentham Science: New York, NY, USA, 2012.

[8] Meola, C.; Carlomagno, G.M. Recent advances in the use of infrared thermography. Meas. Sci. Technol. 2004, 15, R27.

[9] Lahiri, B.; Bagavathiappan, S.; Jayakumar, T.; Philip, J. Medical applications of infrared thermography: A review. Infrared Phys. Technol. 2012, 55, 221–235.

[10] Purohit, R.; Turner, T.A.; Pascoe, D.D. Use of infrared imaging in veterinary medicine. In Medical Infrared Imaging; Diakides, N.A., Bronzino, J.D., Eds.; CRC Press: Boca Raton, FL, USA, 2008.

[11] Bogue, R. Sensors for condition monitoring: A review of technologies and applications. Sens. Rev. 2013, 33, 295–299.

[12] Al-Kassir, A.R.; Fernandez, J.; Tinaut, F.; Castro, F. Thermographic study of energetic installations. Appl. Therm. Eng. 2005, 25, 183–190.

[13] Ibarra-Castanedo, C.; Tarpani, J.R.; Maldague, X.P. Nondestructive testing with thermography. Eur. J. Phys. 2013, 34, S91.

[14] Bagavathiappan, S.; Lahiri, B.; Saravanan, T.; Philip, J.; Jayakumar, T. Infrared thermography for condition monitoring—A review. Infrared Phys. Technol. 2013, 60, 35–55.

[15] Chou, Y.C.; Yao, L. Automatic diagnostic system of electrical equipment using infrared thermography. In Proceedings of the SOCPAR’09 International Conference of IEEE Soft Computing and Pattern Recognition, Malacca, Malaysia, 4–7 December 2009; pp. 155–160.

[16] Luong, M.P. Fatigue limit evaluation of metals using an infrared thermographic technique. Mech. Mater. 1998, 28, 155–163.

[17] La Rosa, G.; Risitano, A. Thermographic methodology for rapid determination of the fatigue limit of materials and mechanical components. Int. J. Fatigue 2000, 22, 65–73.

[18] Grinzato, E.; Vavilov, V.; Kauppinen, T. Quantitative infrared thermography in buildings. Energy Build. 1998, 29, 1–9.

[19] Palumbo, D., De Finis, R., Demelio, P. G., & Galietti, U. (2017). Early detection of damage mechanisms in composites during fatigue tests. In Conference Proceedings of the Society for Experimental Mechanics Series (Vol. 8, pp. 133–141).

[20] Badulescu, C.; Gr´ediac, M.; Haddadi, H.; Mathias, J.D.; Balandraud, X.; Tran, H.S. Applying the grid method and infrared thermography to investigate plastic deformation in aluminium multicrystal. Mech. Mater. 2011, 43, 36–53.

[21] Pastor, M.; Balandraud, X.; Gr´ediac, M.; Robert, J. Applying infrared thermography to study the heating of 2024-T3 aluminium specimens under fatigue loading. Infrared Phys. Technol. 2008, 51, 505–515.

[22] Meola, C.; Carlomagno, G.M.; Squillace, A.; Giorleo, G. The use of infrared thermography for nondestructive evaluation of joints. Infrared Phys. Technol. 2004, 46, 93–99.

[23] Grosso, M., Marinho, C. A., Nesteruk, D. A., Rebello, J. M. A., Soares, S. D., & Vavilov, V. P. (2013). Evaluating quality of adhesive joints in glass fiber plastic piping by using active thermal NDT. Proceedings of SPIE - The International Society for Optical Engineering, 8705, 1–11.

[24] Balaras, C.; Argiriou, A. Infrared thermography for building diagnostics. Energy Build. 2002, 34, 171–183.

[25] Bomberg, M.; Shirtliffe, C. Influence of moisture and moisture gradients on heat transfer through porous building materials. ASTM STP 1978, 660, 211–233.

[26] Ljungberg, S.A. Infrared techniques in buildings and structures: Operation and maintenance. Infrared Methodol. Technol. 1994, 7, 211.

[27] Maierhofer, C.; Roellig, M. Active thermography for the characterization of surfaces and interfaces of historic masonry structures. In Proceedings of the 7th International Symposium on Non-destructive Testing in Civil Engineering (NDTCE), Nantes, France, 30 June–3 July 2009.

[28] Grinzato, E.; Bison, P.; Marinetti, S. Monitoring of ancient buildings by the thermal method. J. Cultural Herit. 2002, 3, 21–29.

[29] Kiiskinen, H.T.; Kukkonen, H.K.; Pakarinen, P.I.; Laine, A.J. Infrared thermography examination of paper structure. Tappi J. 1997, 80, 159–162.

[30] Sugiura, R.; Noguchi, N.; Ishii, K. Correction of low-altitude thermal images applied to estimating soil water status. Biosyst. Eng. 2007, 96, 301–313.

[31] Vavilov, V.P.; Nesteruk, D.A. Detecting water in aviation honeycomb structures: The quantitative approach. Quant. InfraRed Thermogr. J. 2004, 1, 173–184.

[32] Hsu, D. K., Barnard, D. J., Kite, A. H., & Kim, K. B. (2008). NDE for water ingression in composite radomes on aircraft. In AIP Conference Proceedings (Vol. 975, pp. 982–987).

[33] Ibarra-Castanedo, C.; Genest, M.; Piau, J.M.; Guibert, S.; Bendada, A.; Maldague, X.P.; Chen, C. Ultrasonic and Advanced Methods for Nondestructive Testing and Material Characterization. In Active Infrared Thermography Techniques for the Non-

Destructive Testing of Materials; Chen, C.H., Ed.; World Scientific: Singapore, Singapore, 2007; pp. 325–348.

[34] Ibarra-Castanedo, C.; Galmiche, F.; Darabi, A.; Pilla, M.; Klein, M.; Ziadi, A.; Vallerand, S.; Pelletier, J.F.; Maldague, X.P. Thermographic nondestructive evaluation: Overview of recent progress. Proc. SPIE 5073, 2003; doi:10.1117/12.485699.

[35] Bison P.G., Marinetti S., Grinzato E., Vavilov V.(2003). “Inspecting Thermal Barrier Coatings by IR thermography”, Thermosense, vol.22, pp.2012-2018.

[36] Usamentiaga, R.; Garc´ıa, D.F.; Molleda, J. Real-time adaptive method for noise filtering of a stream of thermographic line scans based on spatial overlapping and edge detection. J. Electron. Imaging 2008, 17, 033012.

[37] Howell, J.R.; Siegel, R.; Menguc, M.P. Thermal Radiation Heat Transfer, 5th ed.; Taylor and Francis: New York, NY, USA, 2010.

[38] Usamentiaga, R., Venegas, P., Guerediaga, J., Vega, L., Molleda, J., & Bulnes, F. G. (2014). Infrared thermography for temperature measurement and non-destructive testing. Sensors (Basel, Switzerland).

[39] Giorleo G. and Meola C. “Comparison between pulsed and modulated thermography in glass-epoxy laminates”, NDT&E International, 35:287–292, 2002.

[40] Nordal P. E. and Kanstand S. O. “Photothermal radiometry,” Physica Scripta, 20:659- 662, 1979.

[41] Busse G. “Techniques of infrared thermography: Part 4. Lockin thermography,” in Nondestructive Handbook, Infrared and Thermal Testing, Volume 3, X. Maldague technical ed., P. O. Moore ed., 3rd edition, Columbus, Ohio, ASNT Press, 2001, 718 p.

[42] Wu D. and Busse G. “Lock-in Thermography for NonDestructive Evaluation of Materials,” Rev. Gén. Therm., 37:693-703, 1998.

[43] Carslaw H. S. and Jaeger J. C. Conduction of Heat in Solids, 2nd edition, Clarendon Press, Oxford, 1986.

[44] Favro L. D. and Han X. "Thermal Wave Materials Characterization and Thermal Wave Imaging," in Birnbaum G., Auld B. A. (eds.): Sensing for Materials Characterization, Processing and Manufacuring, ASNT TONES, 1:399-415, 1998.

[45] Bracewell R. The Fourier Transform and its Applications, McGraw-Hill, USA, 1965.

[46] S. Stefano, P.A. Nicolas, I.C. Clemente, S. Carlo, T. Panagiotis, B. Abdelhakim P. Alfonso, P. Domenica, K Maria and M. Xavier. Surface and Subsurface Defects Detection in Impacted Composite Materials Made by Natural Fibers, Using Non-destructive Testing Methods, International Journal Composite Material, 2014, 4(5A), pg.1-9.

[47] Valivov VP. Infrared NDT of bonded structures. Brit J Ndt 1981:175–83.

[48] Vavilov VP, Taylor R. Theoretical and practical aspects of the thermal nondestructive testing of bonded structures. Research Techniques in Nondestructive testing, 5. London: Academic Press; 1982. p. 239–79.

[49] Almond DP, Delpech P, Peng Wang, Behesty M. Quantitative determination of impact damage and other defects in carbon fiber composites by transient thermography. Proc SPIE 1996;2944:256–64.

[50] Thermal Wave Imaging, Inc. Ferndale MI, USA.

[51] C-Checkir, Automation technology GmbH, Bad Oldesloe, Germany.

[52] Osiander R, Spicer JWM. Time resolved radiometry with step-heating – a review. Rev Gen De Therm 1998;37:680–92.

[53] Badghaish AA, Fleming DC. Non-destructive inspection of composites using step heating thermography. J Compos Mater 2008;42:1337–57.

[54] Roche J–M, Balageas D. Common tools for quantitative pulse and step-heating thermography-Parts l and ll. QIRT Conference, Bordeaux, France, 1-28; 2014.

[55] Clemente Ibarra-Castanedo, Marc Genest, J.-M. P., & Stéphane Guibert, A. B. and X. P. V. M. (2015). ACTIVE INFRARED THERMOGRAPHY TECHNIQUES FOR

THE NONDESTRUCTIVE TESTING OF MATERIALS. In Active infrared thermography NDT techniques.

3. Measuring chain: individual parts and their effects

This chapter presents a brief overview of the radiation detector principles used in thermal imaging systems. It gives the background knowledge of the operation principles, the limiting factors for the detector performance, and the imaging systems. The acquisition procedure and the processing algorithms are then introduced for interpretation of the thermal data to extract the features of interest and discussed.
Background material for all produced papers is mainly presented in this chapter.

3.1. Infrared cameras

The basic component of an infrared measurement chain is an infrared camera.
The essential elements of an original form of infrared imager are illustrated as a block diagram in Figure 3.1-1. They are:

- An optical system that can form an image of an external scene using radiation in the infrared wavelength range.
- One or more detector elements that can convert this radiation into electrical signals proportional to the radiation falling onto them.
- Some systems require a scanning mechanism that scans the infrared image in a regular pattern across the detector element(s), although most modern imagers do not require this, since they use large detector arrays that completely cover the field of view of the imager (the detectors are arranged in a matrix of columns and rows: focal plane arrays (FPA)).
- An electronic processor that processes the detector outputs and converts them into a video signal.
- A display unit that generates a visual image from the video signal [1].

The understanding of the complete camera operation requires a more detailed discussion of these main camera components and their interaction in the measurement process.

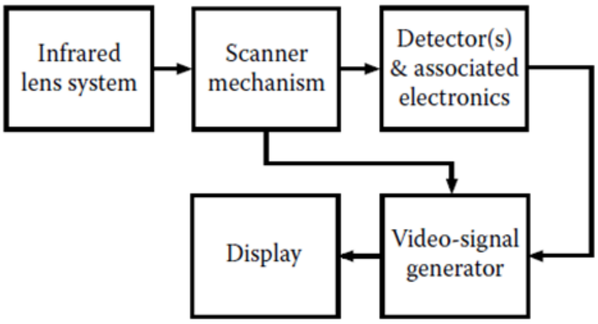

Figure 3.1-1: Block diagram illustrating the main subunits that make up a thermal imaging camera [1]

3.1.1. Optical Systems

The optical systems used in thermal imagers are designed and function in the same way as optical systems for visible wavelengths. The main difference is that most of the materials used for thermal wavelengths are different from those used for visible wavelengths, and in fact, there are differences between optical materials used in the 3–5 µm band and those used in the 8–14 µm band.

Table 3.1-1 lists some of the optical materials that are used and their suitability for each of these bands.

An important aspect of some of the lens materials is their relatively high refractive index compared with those of the glasses used for visible wavelength optics. This has an important effect: uncoated surfaces have a high reflectivity. The high reflectivity means that these materials must be used with an antireflection coating, in order to both obtain good transmission through the optical system and reduce levels of unwanted glare radiation caused by multiple reflections between optical surfaces. Unwanted reflections at optical surfaces are usually the cause of the narcissus effect in a thermal imager, where a cooled detector element virtually sees an image of itself. This usually results in a dark or bright halo in the center of the image. Developing efficient coatings for some of these materials has been an important aspect of thermal imaging.

In many applications it is desirable to have a plane-parallel-sided window between the thermal imager and the scene being imaged. Such a window will be designed to protect the imager from the external environment. The same materials listed above (Table 3.1-1) will of course be suitable for windows, but the choice of material and its coating will depend on the particular application and very specifically the conditions it will have to withstand.

Table 3.1-1: Commonly Used Materials for Optical Systems Working at Thermal Wavelengths [2]

Material	**Useful Wavelength Range in μm**	**Refractive Index**	Comments
Silicon	1.4–7 and 20–25	3.43 at 4 μm 3.42 at 10 μm	Has significant absorption bands from approximately 7 to 20 μm; however, it can be used in the 8–12 μm range in thin sections
Germanium	1.6–20	4.02 at 4 μm 4.01 at 10 μm	Most commonly used material for lenses and windows in the 8–14μm band
Zinc sulfide	0.4–12	2.25 at 4 μm 2.20 at 10 μm	
Zinc selenide	0.5–20	2.43 at 4 μm 2.41 at 10 μm	Used extensively in conjunction with Ge in multielement objectives for the 8–14 μm band
Calcium fluoride	0.13–12	1.41 at 4 μm 1.31 at 10 μm	
Sapphire (aluminum oxide)	0.17–6.5	1.67 at 4 μm	Very hard and abrasive resistant
KRS5 (thallium bromoiodide)	0.5–40	2.38 at 4 μm 2.37 at 10 μm	Note that thallium salts are very toxic
Sodium chloride	0.17–18	1.52 at 4 μm 1.49 at 10 μm	Very hygroscopic, but can be coated with protective films

3.1.2. Radiation detectors

Possibly the most important part of a thermal imager is the detector or detector array. It largely determines the potential level of thermal and spatial resolution that can be achieved as well as the complexity that is required to fulfill this potential.

There are basically two types of thermal infrared (IR) detectors. The first depends on the IR radiation heating the detector element, with the resulting temperature rise then triggering some other physical mechanism that is taken as a measure of the radiation falling onto the element. This type of detector is generally known as a thermal detector. The second type of detector is one where the photons, which are the incident radiation, interact at an atomic or molecular level with the material of the detector to produce charge carriers that generate a voltage across the detector element, or a change in its electrical resistance or current. The mechanism usually involves an electron absorbing a photon and, as a result, moving from one quantum energy level to another. The signal is generated by the direct interaction of photons with charge carriers such as electrons, to change their energy state. The energy of the photon must be greater than the quantum level change that produces the effect.

This level determines the long-wavelength cutoff of the detector. Since the energy of a photon is given by hc/λ, where h is Planck's constant, c is the velocity of light, and λ is the wavelength of the photon, we have that the cutoff wavelength is given by equation (16):

$$\lambda_0 = {}^{hc}/_{E_g} \tag{16}$$

where E_g is the energy gap corresponding to the quantum level change. We note that since the signal response in this type of detector depends on the number of incident photons and not on the total photon energy, the responsivity of the detector (expressed as signal output per unit radiant energy input) will therefore fall off linearly as the wavelength decreases, in theory.

This type of detector is usually referred to as a photon or quantum detector.

Photon detectors are mainly semiconductors with suitable doping to achieve the desired characteristics. They usually operate either as photoconductors, where the incident radiation varies the electrical conductivity of the detector element, or as photovoltaic devices, where the radiation actually generates a voltage, usually across a p-n junction. A third mode of operation consists in generating the voltage across a metal - semiconductor junction known as a Schottky barrier. Most photon detectors operating at thermal wavelengths need to be cooled (at least if they are to have a good responsivity). For the 3–5 μm band a temperature of the order of 195K is usually satisfactory, and this can be achieved by means of three-stage thermoelectric devices requiring only a few watts of power to provide the necessary cooling. For the 8–12 μm band temperatures of the order of 77 K are required.

In general, photon detectors provide greater sensitivity than thermal detectors. However, to achieve this better performance they usually need to be cooled to permit the charge carriers to populate the quantum energy levels where they can have the desired interaction with the incident photons. The need to cool detectors of this type is a major factor in both the design and application of thermal imagers that use photon detectors, and there are different methods of cooling.

Thermal detectors have the great advantage that they do not normally require cooling, although some types of thermal detectors require their temperature to be controlled to ensure that they operate under optimum conditions.

These detectors are also called energy detectors, or photon absorbers, because they absorb the incident energy and warm up; their temperature changes are measured through the variation of a temperature-dependent property of the material such as the electrical resistance. The main advantage is their response at room temperature and over a large band of the IR spectrum. The main disadvantage is their relatively slow response time (of the order of milliseconds), which makes them not suitable for high frequency events. An example of detector that belong to this family is the bolometer/microbolometer.

The microbolometer technology is based on the resistance change with temperature of a resistor element and is the mostly employed in handheld IR systems. Basically, a microbolometer consists of two platinum strips, covered with lampblack; one strip is shielded from the radiation and the other one is exposed to it. The two strips form two branches of a Wheatstone bridge; the resistance in the circuit varies when the strip, which is exposed to IR radiation, heats up and changes its electrical resistance [3]. These thermal imagers meet the demands of most practical applications and are much less expensive than photon detector cameras. Microbolometers are characterized by relatively low sensitivities/detectivities, broad/flat spectral response curves, and slow response times of the order of 10 ms. Microbolometer detectors are mostly temperature stabilized by a Peltier element. Because of their operation as thermal detectors, bolometers do not offer the possibility to fix the integration time. Rather, the ‘‘integration time’’ is given by their thermal time constant. The frame rate of these cameras cannot be changed by the user.

In selecting the type of detector to use in a thermal imager there are several factors to consider, mainly :

- The wavelength band in which it operates
- The frequency response; i.e., can it operate at sufficiently high frequencies to provide standard video frame rates or even higher frame rates for some applications?

- The thermal sensitivity and spatial resolution that can be achieved
- Cooling requirements and the associated complexity, cost, and possible inconveniences
- Reliability and cost

3.2. Performance parameters for an infrared camera

An user of such technology must have some background knowledge of the limiting factors for the camera parameters such as temperature accuracy, temperature resolution (NETD, noise equivalent temperature difference), spatial resolution, and so on.

The system performance evaluation of thermal imagers is well standardized and much work of research has been done on characteristics and testing of imaging systems [4-8]. In general, it is, however, difficult for most practitioners to relate the relevance of the system performance parameters to their applications and the measurement results.

The performance of a thermal imaging system is described by several parameters such as thermal response, detector and electronic noise, geometric resolution, accuracy, spectral range, frame rate, integration time, and so on. These parameters can be divided into two groups: objective and subjective parameters (Table 3.2-1).

The temperature resolution given by NETD and the spatial resolution given by IFOV are important objective performance parameters. They both significantly affect the image quality.

An evaluation of the quality and performance limits of thermal imagers more oriented to practical applications requires a combination of these parameters.

Additionally, the subjective factor (the ability to detect, recognize, and identify temperature differences while using the camera system) due to the human observer must be taken into consideration. The minimum resolvable temperature difference (MRTD) and the minimum detectable temperature difference (MDTD) combine the objective and subjective parameters and are directly related to applications.

For any practical thermal imaging, the following question must eventually be answered: Is the camera suited to my application based on its performance parameters?

The accurate knowledge of the most important performance limits of the thermal imaging system used and their relevance to the application is crucial for correct temperature measurements and interpretation of the results. Therefore, camera performance parameters and their influence on practical measurement results are discussed in more detail in the following paragraphs.

Temperature Accuracy

The specification of accuracy (or, more precisely, inaccuracy) gives the absolute value of the temperature measurement error for blackbody temperature measurements. For most thermocameras, the absolute temperature accuracy is specified to be ±2 K or ±2% of the temperature measured. The larger value is valid. The temperature measurement errors arise because of errors in radiometry connected with the calibration procedure, the long- and short-term variability of the camera sensitivity, the limited accuracy of object radiation calculation from the measured radiant power and so on. For the short-term reproducibility of a temperature measurement, a value of ±1% or ±1 K is typical.

Field of View (FOV)

The object field is transformed into an image within the FOV of the camera. The FOV is the angular extent of the observable object field (Figure 3.2-1). Sometimes the FOV is also given as the area seen by the camera.

The FOV can be easily constructed by the geometrical optics. Rays passing through the center of a (thin) lens are not refracted. Therefore, rays that finally hit the four edges of the detector array limit the FOV.

Table 3.2-1: Camera performance parameters [9].

	Name	Definition, description	Unit	Significance
Objective parameters	Temperature accuracy	Absolute error of blackbody temperature measurement	K,◦C,◦F	Absolute measurement accuracy
	NETD (noise equivalent temperature difference)	Minimum temperature difference for SNR = 1	K,◦C,◦F	Temperature resolution
	FOV (field of view)	Angular extent of camera observable object field	degree,°	Detected object field
	IFOV (instantaneous field of view)	Angular extent of object field from which radiation is incident on the detector	mrad	Spatial resolution
	Frame rate	Frequency at which unique consecutive images are produced	1/s, Hz	Time resolution
	Integration time	Period of signal integration	s	Time resolution, Sensitivity
	MTF (modulation transfer function)	Fourier transform of the camera response when viewing an ideal point source.		Spatial resolution
Subjective parameters	MRTD (minimum resolvable temperature difference)	Minimum temperature difference at which a 4 bar target can be resolved by a human observer dependent on the spatial frequency of the bar target.	K,◦C,◦F (dependent on spatial frequency)	Recognition of temperature difference
	MDTD (minimum detectable temperature difference)	Minimum temperature difference at which a circular or square object can be detected by a human observer dependent on the object size.	K, ◦C, ◦F (dependent on object size)	Detection of small size objects with low temperature difference

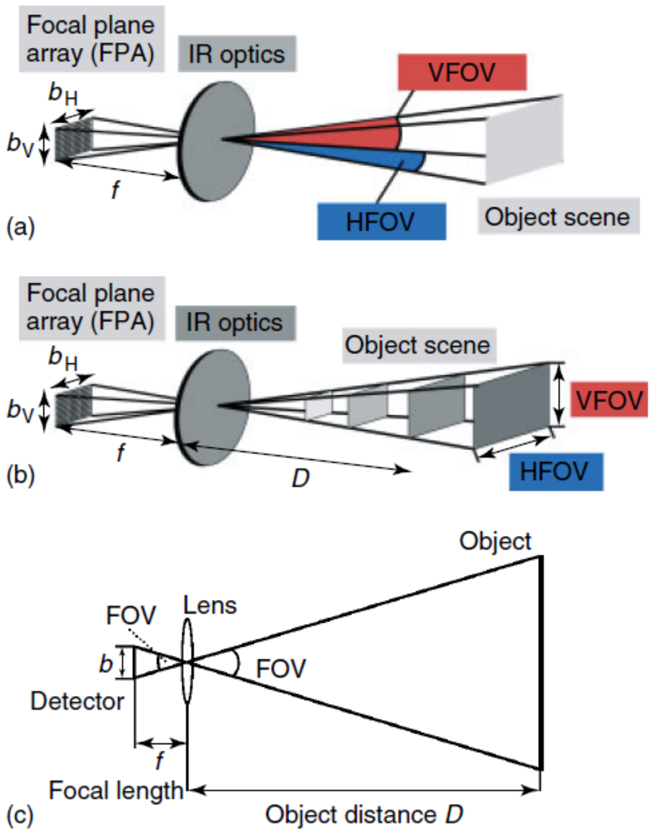

Figure 3.2-1: Calculation of the cameras angular field of view (a) and the area seen by the camera (b). Two-dimensional cross section (c) [9].

The FOV depends on both the camera lens and the FPA dimensions. For a camera lens with focal length f and FPA with the linear dimension b, the FOV can be calculated as follows:

$$FOV = 2\arctan\left(\frac{b}{2f}\right) \tag{17}$$

The object area with the length x seen by the camera at a given object distance D can be calculated from:

$$x = 2Dtan\left(\frac{FOV}{2}\right) \tag{18}$$

The rectangular shape of the FPA causes different horizontal field of view (HFOV) and vertical field of view (VFOV).

The smaller the FOV of the camera, the better the spatial resolution of the IR image is. The knowledge of the camera FOV is necessary to estimate the smallest object that can be detected and to ensure a correct temperature measurement. From the FOV, IFOV can be determined by dividing the FOV by the number of FPA pixels in a line (horizontal or HIFOV) or in a column (vertical or VIFOV; see Section on *Spatial resolution*).

Narcissus Effect

In IR imaging, an optical reflection effect occurs which is unknown from imaging in the visible spectral range. The so-called narcissus effect occurs if there is a reflection from the camera lens, a window, or an object such that the camera detects the reflection of itself. The narcissus effect becomes pronounced if the reflecting object is in the focus of the camera. This effect results in a dark (cold) or a bright spot (warm) in the infrared image depending on the detector temperature. One possibility to avoid this effect is to change the viewing angle to a value such that there is no incident reflected radiation from the camera detector area on the camera objective.

Calibration

The infrared camera as a radiometer allows to measure some radiometric quantities such as radiance or radiant power. The purpose of calibration is to determine the accurate quantitative relations between camera output and incident radiation. For the calibration procedure, black bodies (emissivity close to unity) at different temperatures are used, since their radiometric quantities and their spectral quantities are well defined. Therefore, the calibration process gives a relation between camera signal and blackbody temperature. During camera calibration, the signal of each pixel depending on the blackbody temperature is determined. After the camera calibration, all pixels will give the correct temperature information of the object.

During calibration, the camera aperture is completely covered by the black body. The distance between the camera and the black body is small so that an atmospheric transmittance of unity can be assumed [9].

Noise Equivalent Temperature Difference (NETD)

This is the difference between the temperature of the observed object and the ambient temperature that generates a signal level equal to the noise level. It is also called the temperature resolution. NETD is defined as the ratio of the RMS noise voltage U_n to the voltage increment ΔU_s generated by the difference in temperature between the measurement area of a technical black body (or test body) T_{ob} and background temperature T_o, divided by such a difference:

$$NEDT = \frac{U_n}{\frac{\Delta U_s}{T_{ob}-T_o}} = \frac{T_{ob}-T_o}{\frac{\Delta U_s}{U_n}}, \mathrm{K} \tag{19}$$

The temperature of a technical black body measurement area is usually equal to 30 °C, with a background temperature of 22 °C, and the difference $T_{ob} - T_o$ should be within 5–10K (Figure 3.2-2).

There is also another, slightly different definition of the NETD parameter: it is defined as the difference of temperatures T_{ob} and T_o observed by the detector, which results in a change in the output signal equal to the noise of the detector. NETD is determined from observation of the area of a technical black body, whose temperature T_{ob} is close to the background temperature T_o (Figure 3.2-2a). An example of a signal coming from a detector along line N is presented in Figure 3.2-2b. The value of NETD is determined when signal U_s is equal to noise level U_n.

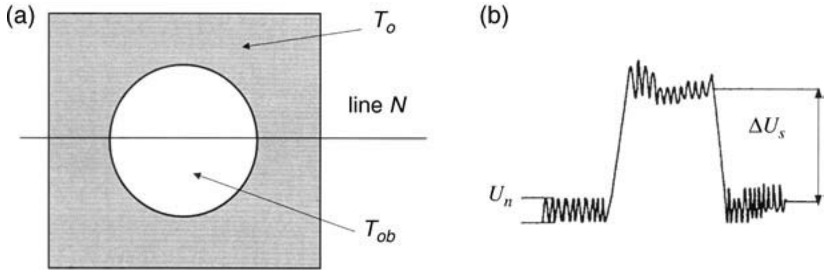

Figure 3.2-2: Interpretation of determination of the NETD parameter [10]

In both cases NETD is defined as the minimum increment of the temperature difference, or as the minimum difference of temperatures T_{ob} and T_o that can be distinguished by a point (single) detector (or a linear or array detector) for a given amplifier bandwidth. According to the theory presented in [11], narrowing of the amplifier bandwidth results in a decrease of the noise voltage (i.e. a decrease of NETD), but on the other hand it deteriorates the spatial resolution (e.g. for a constant scanning speed). Circular or rectangular test fields of stabilized temperature T_{ob} can be used in measurements instead of a technical black body measurement field. The presented definitions of NETD do not take into consideration the size of an object, physiology of human perception or properties of the display system.

A greater value of NETD indicates a lower sensitivity of the camera. Therefore, in the technical data of IR cameras, the NETD parameter is called 'thermal sensitivity' or ‘temperature resolution’. The catalogue value of the temperature resolution should be accompanied by the value of T_{ob} at which NETD was evaluated.

NETD is one of the most popular parameters for assessing the metrological properties of an IR camera [12].

Spatial Resolution – IFOV

The IFOV gives the angle over which one detector element of the focal plane array senses the object radiation [5] (Figure 3.2-3). Using the small angle approximation, the minimum object size whose image fits on a single detector element for a given distance can be calculated as: object size = IFOV · distance (Table 2.5).

For example, a focal length of f = 50 mm and a single pixel size of 50 µm give an IFOV of 1 mrad. At a distance D = 5.5 m, this IFOV refers to a minimum object size of 5.5mm.

It is important to have in mind that the IFOV is only a geometric value calculated from the detector size and the focal length of the optics (Figure 3.2-4). The IFOV can also be determined by dividing the FOV by the number of pixels, for example, the IFOV amounts to 1 mrad for 20◦ FOV and 320 pixels.

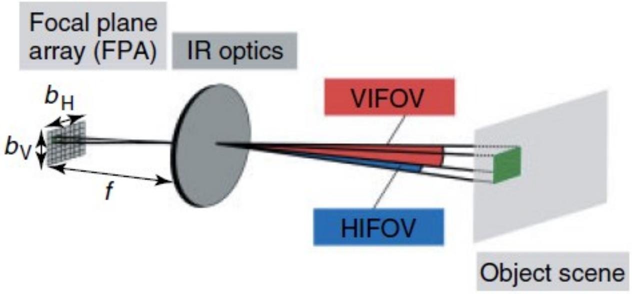

Figure 3.2-3: Angular IFOV for a detector pixel [9].

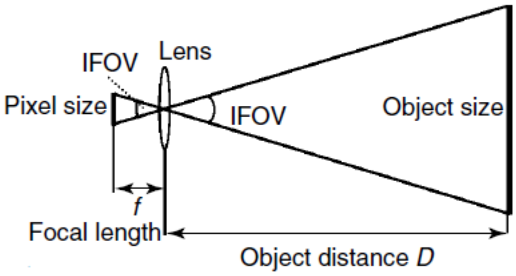

Figure 3.2-4: Spatial resolution, two-dimensional definition of IFOV [9].

Image Quality: MTF, MRTD, and MDTD

The minimum resolvable temperature difference (MRTD) measures the compound ability of a thermal imaging system and an observer to recognize periodic bar targets within the image shown on a display. It is the minimum temperature difference between the test patterns and the blackbody background at which the observer can detect the pattern. This capability is governed by the thermal sensitivity (NETD) and the spatial resolution (IFOV) of the imaging system but strongly depends on other influencing variables such as the used palette, the ability of the observer to distinguish between different colors, and so on. The MDTD measures the compound ability of the thermal imaging system and an observer to detect a small size object. It is the minimum temperature difference between a circular or square object and the background necessary to detect the object.

ASTM standards MRTD and minimum detectable temperature difference (MDTD) test methods have been described in [13, 14].

Time Resolution – Frame Rate and Integration Time

The accurate analysis of transient thermal processes requires a sufficient time resolution of thermal imaging compared to the characteristic thermal time constant of the process to be investigated. Most practitioners use bolometer cameras that do not offer the possibility of a selectable integration or exposure time in contrast to photon detector.

In data sheets of imaging systems equipped with bolometer focal plane arrays, the time resolution is usually just characterized by the frame rate as the relevant camera parameter. Mostly this value is assumed to be related to the time resolution for the imaging analysis [9]. A detector with a high integration time responds more slowly to temperature changes; as a consequence, the maximum signal is much lower than the correct 100% signal. If the detector time constants are much lower (nanoseconds to microseconds), these detectors respond much faster and the temperature of an object can be correctly determined.

3.3. Camera Software – Software Tools

IR cameras without an analysis software would just provide qualitative false color images of objects. However, whenever quantitative results are needed like temperatures, line plots, or reports, software tools are indispensable.

All manufacturers of thermal imaging systems provide a variety of software tools ranging from general-purpose software packages including, for example, thermal image analysis and generation of infrared inspection reports to sophisticated software packages which, for example, offer camera control functions, real-time image storage at selectable integration times, and frame rates or radiometric calculations.

The general-purpose software mostly contains the following key features:

- level and span adjustment;
- selectable color palette and isotherms;
- definition of spot analysis, lines, and areas with temperature measurements for maximum, minimum, and average temperatures;
- adjustment of object parameters (emissivity) and measurement parameters (e.g., humidity, object distance, ambient temperature);
- creation of professional customized reports with flexible design and layout (e.g., export to other software such as Microsoft Office, including visible images).

For a very detailed analysis of static or transient thermal processes sophisticated software especially designed for R&D is available. Beyond the features of the general-purpose software, such software usually includes more complex data storage, analysis, and camera operation tools:

- remote control of the camera from the PC (most or all camera parameters can be controlled by the PC);
- high-speed IR data acquisition, analysis, and storage;
- digital zoom of the infrared image, use of subframes;
- raw data acquisition and analysis, radiometric calculations;

- automatic temperature vs time and three-dimensional temperature profile plotting, additional graphic, and image processing tools;
- different data format export, automatic conversion to, for example, JPEG, BMP, AVI, or MATLAB-format;
- data export to other common software applications such as Microsoft Office;
- thermal image subtraction;
- definition of different regions of interests (ROIs) with different shapes, separate emissivity, and so on.
- customized camera calibration

3.4. Optical excitation sources

The excitation source is crucial for the thermographic measuring chain. Its performance has a decisive effect on the detection results.

Optical thermography has gained increasing attention because of its non-destructive imaging characteristics with high precision and sensitivity [15].

Optical heaters include lasers, LEDs, Xenon flash tubes, halogen lamps, and common (incandescent) electrical bulbs. Such heaters are well controlled and may deliver a considerable amount of energy onto the surface of a test object. The most powerful heat sources are high power CO2 and diode lasers used for materials processing [16]. The drawbacks of optical heaters are the presence of reflected radiation during heating/cooling, which may be significantly reduced in the case of lasers and LEDs, and a need for high material absorptance in the spectral range of their output. The optical heaters typically used in active thermography are Xenon flash tubes, which provide up to 0.5 millionWm^2 per pulse and halogen lamps which provide up to 30 kWm^2 (halogen lamps) [17].

In PT, the sample surface is stimulated by a short pulse with a high-power light lamp. The thermal wave propagates from the sample surface into the inner part by diffusion. The resultant sequence of infrared images has potential to indicate defects in the sample at different depths [18]. The non-uniform application of heat and variation of surface emissivity might affect the results [19].

In LT, the sample is heated using a mono-frequency sinusoidal thermal excitation. The magnitude of the periodic temperature change at the surface and its phase with respect to the applied modulated heating is extracted by using post-processing algorithms for defect detection [20]. This method has as advantages a better signal-to-noise (S/N) ratio and an adjustable depth range for inner defect visualization. However, it demands a selection of a suitable frequency to avoid the blind frequencies and repetitive experiments are required to resolve the defects location at different depths [22].

ST based on temporal temperature analysis caused by step excitation in time domain is similar to PT in heating excitation mode which has longer heating time.

Those methods usually use flash lamps, halogen lamps or laser beam as heating source powered by an excitation source such as power amplifier with signal generator.

Figure 3.4-1 shows the diagram of an optical thermography system. Halogen lamps, flash lamps or laser beam are driven from pre-set current which is generated by excitation source. Generally, a synchronous trigger receives the “start” command from the PC and then triggers the IR camera and the excitation source to work synchronously. According to the different pre-set excitation current, it can work in LT mode, PT, ST mode.

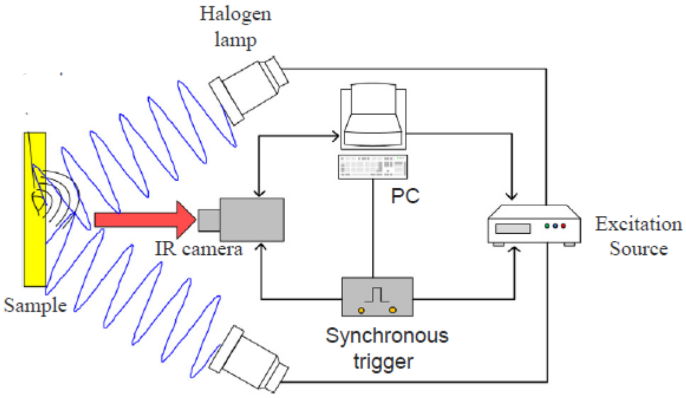

Figure 3.4-1: Diagram of the optical thermography [22]

In LT mode, the pre-set current is an amplitude-modulated current i_{ex}, obtained by combining a low-frequency sinusoidal signal with a high-frequency signal which can be expressed as:

$$i_{ex} = I_m sin(2\pi f_{lock} t) sin(2\pi f_{carr} t) \tag{20}$$

where I_m is the maximum of the amplitude. f_{lock} and f_{carr} are lock-in frequency and carrier frequency, respectively. The excitation current profile is shown in Figure 3.4-2.

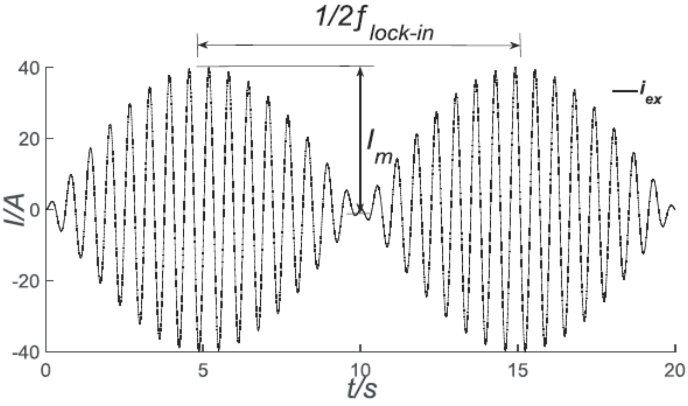

Figure 3.4-2: Profile of the lock-in excitation current [22]

According to the theory of thermal wave, the probing depth of defects depends on the length of the thermal diffusion which can be given by:

$$\mu_{th} = \sqrt{\frac{\alpha}{\pi f_{lock}}} = \sqrt{\frac{k}{\pi f_{lock} \rho c_p}} \tag{21}$$

where α is thermal diffusity (m^2/s), k is the thermal conductivity of the material (W/mK), ρ is the density (kg/m^3), c_p is specific heat (J/(kg·K)) at costant pressure. For a specific material, the value of μ_{th} is determined by the lock-in frequency. Thus, the sample is heated periodically and the temperature on the surface of the sample varies periodically as well. Due to fact that the variation of frequency is nearly equal to the lock-in frequency, the interference such as non-uniform heating, environmental reflections and surface emissivity variations can be suppressed extensively by using Fourier analysis [23]. Thus, the lock-in frequency of the excitation source should be set manually for the specific sample with different structure and characteristics. The range of lock-in frequency is usually adjusted between 0.01 Hz to dozens Hz and the carrier frequency range is dozens to hundreds Hz [20,21].

In PT and ST mode, the pre-set current $i\ (t)$ can be expressed by the equation (22) and its profile is shown in Figure 3.4-3.

$$i\ (t) = I_m \cdot sin(2\pi f t) \tag{22}$$

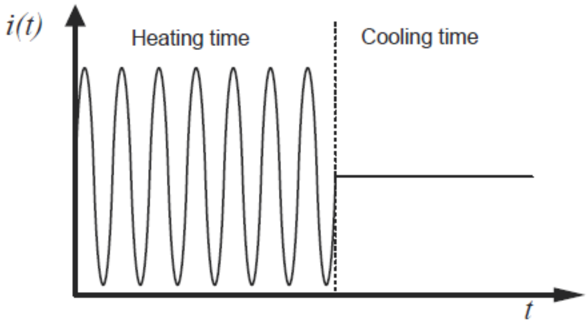

Figure 3.4-3: Profile of the pulsed excitation current [20]

where I_m and f are the current amplitude and frequency, respectively. A pulse of energy is generated by the lamps or flashes which is driven by the excitation current. The duration of the pulse is variable from μs to s depending on the thickness of the material to be probed and its thermal properties.

The excitation source is an important element for the optical thermographic measuring chain whose performances directly influence the accuracy of the detection results. Thus, it is necessary to use a high efficiency and lower cost excitation source.

3.5. Properties of tested materials

A tested material can be described by a few specific properties: emissivity, reflectivity, transmissivity, effusivity and diffusivity.

The emissivity (ε) is the relative ability of its surface to emit energy by radiation. It is the ratio of energy radiated by a particular material to energy radiated by a black body at the same temperature. A true black body would have $\varepsilon = 1$ while any real object would have $\varepsilon < 1$. Emissivity is a dimensionless quantity. In general, the duller and blacker a material is, the closer its emissivity is to 1. This is a surface property and surfaces with high emissivity are the most attractive for thermography as the optical energy applied is fully absorbed, after which the surface can emit thermal radiation.

Accurate emissivity measurement is particularly important in low-emissivity materials. In objects with high emissivity, slight variations in the chosen emissivity value cause only minor changes in the resulting surface temperatures. However, in low-emissivity objects, such as polished steel or aluminum, temperature measurement is particularly complicated, because small variations in emissivity lead to large variations in the resulting temperatures.

The thermal reflectivity (r) determines the amount of energy which can be reflected by a material with respect to the total incident energy. A low value of this parameter indicates that a large fraction of the incident energy is absorbed.

The transmissivity (τ) indicates how much energy passes through a material. Almost all materials tested by transient thermography are significantly opaque to energy being applied so they do not transmit radiation (transmissivity $\tau = 0$).

The relation among thermal emissivity, reflectivity and transmissivity of a surface has been described in the paragraph 2.2.

Many surfaces reflect a high proportion of the incident illumination. Therefore, only a small proportion of the incident light is absorbed and converted to heat ($\varepsilon << 1$). The emissivity can be not only much less than unity but its value can also vary across the same surface. As a solution to both these issues, surfaces which are inspected by using transient thermography are very often covered by black paint. This paint increases and equalizes emissivity and therefore it substantially reduces the reflectivity of the surface.

The thermal diffusivity α (m^2/s) is a measure of the material thermal inertia and is described by:

$$\alpha = \frac{k}{\rho c_p} \tag{23}$$

where k is the thermal conductivity (W/mK), ρ is the density (kg/m^3), c_p is the heat capacity (J/kgK).

The higher the value of thermal diffusivity, the shorter time energy takes to diffuse through a material. This parameter affects the required sampling rate of the IR camera (discussed above in the paragraph 3.2) which needs to be high for highly diffusive materials. The total sampling time required to allow for diffusion to the back wall of a layer is specified by:

$$t_{exp} = \frac{L^2}{\pi\alpha} \tag{24}$$

where L is the thickness of the layer and α is the thermal diffusivity [24, 25].

The thermal diffusivity is a measure of the thermal energy diffusion rate through the material. The diffusion rate will increase with the ability to conduct heat and decrease with the amount of thermal energy needed to increase the temperature. Large values of diffusivity mean that objects respond fast to changes of the thermal conditions. Therefore, this quantity governs the timescale of heat transfer into materials. If a material has voids or pores in its structure, then both the thermal conductivity and density decrease, so the thermal diffusivity changes. This implies a variation of the heat transfer within the material is affected, leading to observable changes of surface temperatures in the vicinity of the defects.

Thermal effusivity (e) (J/m^{2}K^{2}s$^{0.5}$) is a measure of the ability of the material to exchange thermal energy with its surroundings and is described by:

$$e = \sqrt{k\rho c_p} \tag{25}$$

This quantity will govern how much the temperature of an object changes if invested with thermal energy. Low values of effusivity lead to high surface temperatures after the pulse deposition [26].

The effusivity also has another effect on heat transfer within a material. Considering a thermal contact between two materials with different effusivities e_1 and e_2 one often characterizes the thermal behavior with the thermal mismatch factor Γ:

$$\Gamma = \frac{e_1 - e_2}{e_1 + e_2} \tag{26}$$

$\Gamma = 0$, that is, equal effusivities, implies that there is no thermal mismatch (the interface of the two materials cannot be detected by a temperature measurement at the surface). For a perfect thermally conducting first material, $\Gamma = 1$ and for a perfect thermally insulating material, $\Gamma = -1$.

If the transient thermal behavior of a composite material is analyzed, the thermal mismatch factor will describe the change in thermal transit time compared to a homogeneous material. The effusivity, in this respect, behaves like, for example, the refraction index in optics when describing the reflection of optical waves being incident onto the interface between two media. An optical interface cannot be detected if the two indices of refraction are identical. In this case, the wave just passes the interface undisturbed without changing its speed. In an even more general scheme, any wave is characterized by a wave resistance or impedance, which depends on the material properties. If the wave hits an interface to another material, reflections can only be observed if there is a change in impedance.

3.6. Data acquisition

According to relative position of excitation and camera, there are two possible configurations for acquiring the data: (1) reflection mode, where excitation and camera are located on the same side, and (2) transmission mode, where excitation and camera are located on the opposite sides. Usually, there is no direct access to both sides of the components. Hence reflection mode configuration is more practical. And, for surface heated by optical sources (optical thermography), defect depth can be quantified under reflection mode while not under transmission mode. However, transmission mode generally yields more accurate results than reflection mode for some components (like thin plate). Another advantage of transmission mode is that the excitation does not block the camera view to sample surface[27].

Various deployments are possible:

- point inspection (example: laser or focused light beam heating);
- line inspection (example: heating with line lamps, heated wire, line of air jets (cool or hot), scanning laser);
- surface inspection (example: heating using lamps, flash lamps, scanning laser); either in reflection (thermal source and detector located on the same side of the inspected component) or in transmission (heating source and detector located on each side of the component).

After the set up configuration is completed a sequence of thermograms can be acquired. A thermogram is a thermal map or image of a target where the grey tones or color hues represent the distribution of infrared thermal radiant energy emitted by the surface of the target.

Thermographic data result in sequences of IR images that reflects the evolution of temperature (after the conversion of the energy detected into a temperature value) in time: $T(x, y, \tau)$. Mathematically, such a sequence can be regarded as a 3D matrix of temperature: $T(i, j, k)$, where i, j are surface coordinates, and k is the discrete time.

3.6.1. Experimental setup and data acquisition for lock-in experiments

Figure 3.6-1 depicts a lock-in thermography experiment (reflection mode). Two lamps are shown although it is possible to use several lamps mounted on a frame to reduce the non-uniform heating and/or to increase the amount of energy delivered to the surface. It is also possible, as previously remarked, to use different optical sources. The lamps send periodic waves (e.g. sinusoids) at a given modulation frequency ω, for at least one cycle, ideally until a steady state is achieved, which depends on the specimen's thermal properties and the defect depth, see Eq. (13) in the paragraph 2.3.1. In practice, however, only a few cycles are needed to adequately retrieve phase and amplitude data, much before attaining steady state conditions.

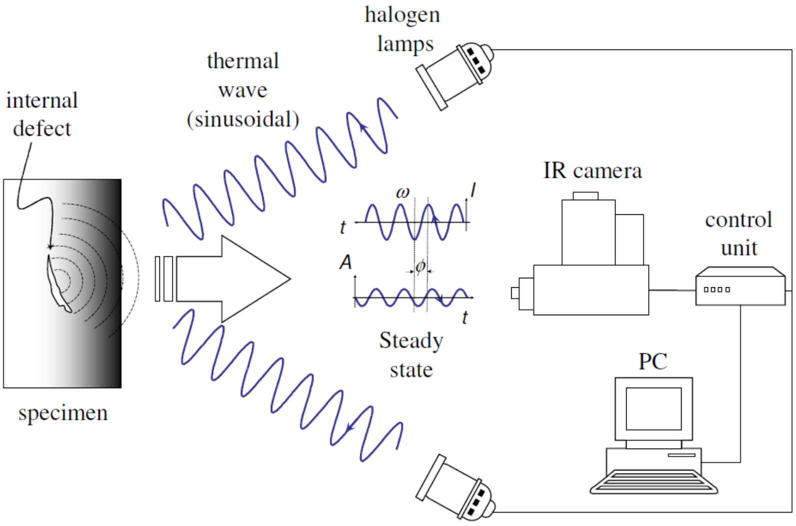

Figure 3.6-1: Experimental set-up for lock-in thermography (reflection mode) [28]

Figure 3.6-2 shows an example of the raw output signal for a sinusoidal input at two different points (pixels). As can be seen, noise is omnipresent and processing is required not only to extract the amplitude and/or phase information but also to de-noise the signal.

A complete LT experiment is carried out by inspecting the specimen at several frequencies, covering a wide range from low to high frequencies, and then a fitting function can be used to complete the amplitude or phase profiles for each point (i.e. each pixel). Nevertheless, there exists a direct relationship between depth and the inspection frequency that allows depth estimations to be performed from amplitude or phase data without further processing. Furthermore, the energy required to perform an LT experiment is generally less than in other active techniques, which might be interesting if a low power source is to be used or if special care has to be given to the inspected part [29].

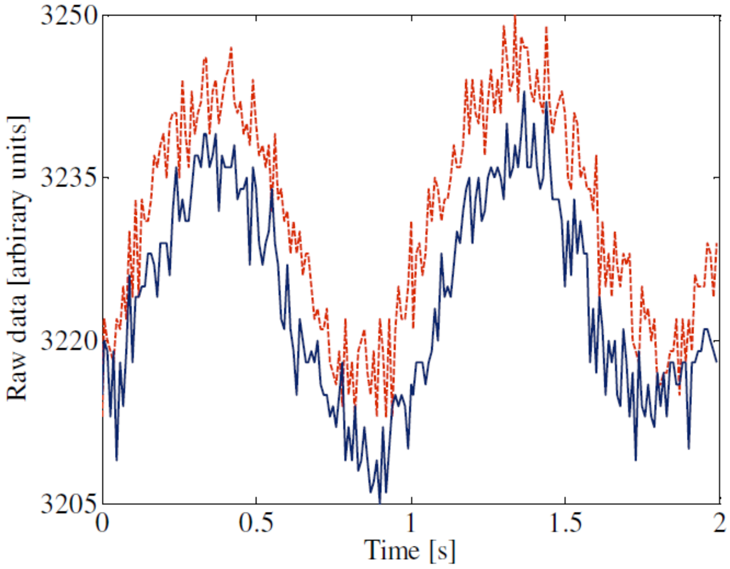

Figure 3.6-2: Lock in raw data output signal [28]

3.6.2. Experimental setup and data acquisition for pulsed and stepped/long pulsed thermography

When compared to LT, data acquisition in PT/ST is fast and straightforward as illustrated in Figure 3.6 3.

Two photographic flashes are used to heat up the specimen's surface, and the thermal changes are recorded with an infrared camera. A synchronization unit is needed to control the time between the launch of the thermal pulse and the recording with the IR camera. Data is stored, as described above, as a 3D matrix. Temperature decreases approximately with the square root of time (at least at early times), as predicted by Eq. (15), except for the defective areas, where the cooling rate is different.

Although heat diffusion is a complex problem, the relationship between defect depth and time, simplified through Eq. (15), has been exploited by many researchers to develop qualitative and quantitative techniques. These techniques were considered to be some of the most promising ones among many others and they are currently subjected to extensive investigation [28].

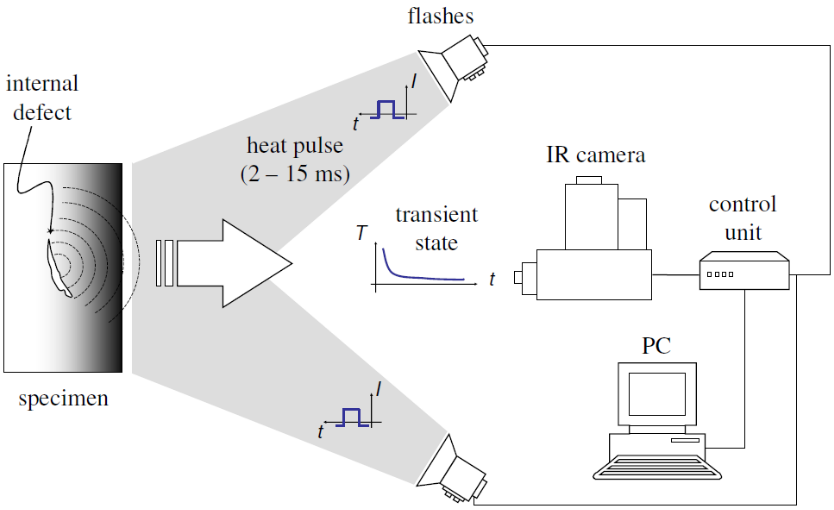

Figure 3.6-3: Experimental set-up for PT/ST thermography (reflection mode) [28]

3.7. Data processing

More recently a new research line began to gain great importance. This new line deals with data processing algorithms, which are used not only to improve the level of detection of the IRT technology, but also to characterize the detected defects in order to automate the inspection process [30].

The first part of this section focuses on signal processing, the second one is concerned with image processing.

3.7.1. Lock-in data processing

Contrary to PT for which a great variety of processing techniques are available, as described below, only a few signal processing techniques are commonly used for LT data. A four-point methodology for sinusoidal stimulation is frequently cited [31, 32] as a tool to retrieve amplitude and phase. Another possibility is to fit the experimental data using least squares regression, [33] and to use this synthetic data to calculate the amplitude and the phase. Alternatively, as for the case of PT, the discrete Fourier transform (DFT) can be used to extract amplitude and phase information from LT data [34].

The four point methodology for sinusoidal stimulation is illustrated in Figure 3.7-1.

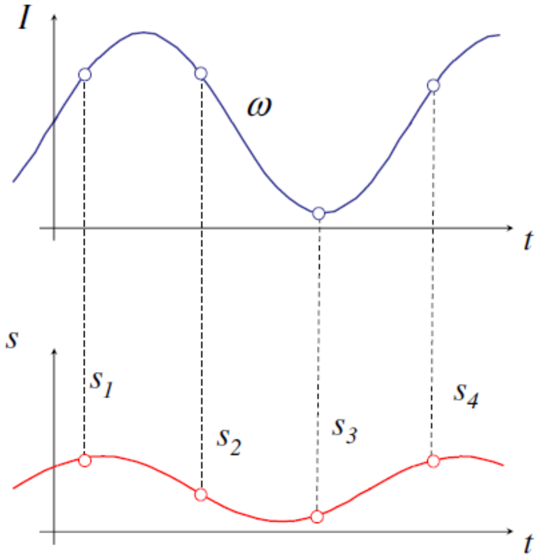

Figure 3.7-1: Four point methodology for amplitude and phase delay estimation by lock-in thermography.

The sinusoidal input signal I is represented on top of the Figure 3.7-1, the response signal S is depicted at the bottom. As mentioned before, input and output have the same shape when sinusoids are used, there is only a change in amplitude and phase that can be calculated as follows [33]:

$$A = \sqrt{(S_1 - S_3)^2 + (S_2 - S_4)^2} \tag{27}$$

$$\Phi = arctan\left(\frac{S_1 - S_3}{S_2 - S_4}\right) \tag{28}$$

The 4-point method is fast but it is valid only for sinusoidal stimulation and is affected by noise. The signal can be de-noised in part by averaging of several points and/or by increasing the number of cycles. The possibility is to fit the experimental data using least squares regression and to use this synthetic data to calculate the amplitude and the phase. This two alternatives contribute to reduce the calculations.

The discrete Fourier transform (DFT) can also be used to extract amplitude and phase information from LT data, as mentioned before. Initially proposed for pulsed thermography data [35] (see pulsed phase thermography below), the DFT can be written as [28]:

$$F_n = \Delta t \sum_{k=0}^{N-1} T(K\Delta t) exp^{\left(-j2\pi nk/N\right)} = Re_n + Im_n \tag{29}$$

where j is the imaginary number ($j^2 = -1$), n designates the frequency increment ($n = 0,1, \ldots N$); Δt is the sampling interval; and Re and Im are the real and the imaginary parts of the transform, respectively.

In this case, real and imaginary parts of the complex transform are used to estimate the amplitude and the phase [35]:

$$A_n = \sqrt{Re_n^2 + Im_n^2} \tag{30}$$

$$\Phi = tan^{-1}\left(\frac{Im_n}{Re_n}\right) \tag{31}$$

The DFT can be use with any waveform (even transient signals as in pulsed phase thermography) and has the great advantage of de-noising the signal. Although very useful, Eq. (29) is time consuming.

Fortunately, the fast Fourier transform (FFT) algorithm is available [36] to be implemented and it can be found (integrally or simplified) in common software packages.

3.7.2. Pulsed and stepped/long pulsed data processing

PT is probably the most extensively investigated approach because of its ease of deployment. Raw PT data however, are difficult to handle and analyze. There are a great variety of processing techniques that have been developed to enhance the subtle IR signatures [35, 37, 38]. A brief discussion is provided for most common applications.

Thermal Contrast Based Techniques

Thermal contrast is a basic operation that despite its simplicity is at the origin of most of the PT analysis. Various thermal contrast definitions exist, but they all share the need to specify a sound area S_a, i.e. a non-defective region within the field of view. For instance, the absolute thermal contrast $\Delta T(t)$ is defined as [39]:

$$\Delta T(t) = T_d(t) - T_{S_a}(t) \tag{32}$$

with $T(t)$ being the temperature at time t, $T_d(t)$ the temperature of a pixel or the average value of a group of pixels, and $T_{S_a}(t)$ the temperature at time t for the S_a. No defect can be detected at a particular t if $\Delta T(t) = 0$.

The main drawback of classical thermal contrast is establishing S_a, especially if automated analysis is needed. Even when S_a definition is straightforward, considerable variations on the results are observed when changing the location of S_a as is well-known [40].

Pulsed Phase Thermography

Pulsed phase thermography (PPT), is another interesting technique, in which data are transformed from the time domain to the frequency spectra using the one-dimensional discrete Fourier transform (DFT), i.e. Eq. (29). The use of the DFT, or more precisely the FFT on thermographic data was first proposed by Maldague and Marinetti in 1996 [35]. Since then, it has been applied to other thermographic data, such as lock-in, described in section 3.7.1. As for the case of LT, the amplitude and the phase can be computed from Eqs. (29) and (30). The frequency components can be derived from the time spectra as follows:

$$f = \frac{n}{N\Delta t} \tag{33}$$

where n designates the frequency increment ($n = 0,1, \dots N$), Δt is the time step and N is the total number of frames in the sequence recorded.

Phase Φ is of particular interest in NDE given that it is less affected than raw thermal data by environmental reflections, emissivity variations, non-uniform heating, surface geometry and orientation. These phase characteristics are very attractive not only for qualitative inspections but also for quantitative characterization of materials.

The FFT is typically used to extract amplitude and phase information.

Thermographic Signal Reconstruction

Thermographic signal reconstruction (TSR) is an attractive technique that allows increasing spatial and temporal resolution of a sequence, reducing at the same time the amount of data to be manipulated. TSR is based on the assumption that, temperature profiles for non-defective pixels should follow the decay curve given by the one-dimensional solution of the Fourier Equation, i.e. Eq. (12), which may be rewritten in the logarithmic form as:

$$ln(\Delta t) = ln\left(\frac{Q}{e}\right) - \frac{1}{2} ln(\pi t) \tag{34}$$

Next, an n-degree polynomial is fitted for each pixel [41]:

$$ln(\Delta t) = a_0 + a_1 ln(t) + a_2 ln^2(t) + \cdots + a_p ln^p(t) \tag{35}$$

Typically, n is set to 4 or 5 to avoid "ringing" and to insure a good correspondence between data and fitted values. Synthetic data processing brings interesting advantages such as: significant noise reduction, possibility for analytical computations, considerably less storage is required since the whole data set is reduced from N to $p + 1$ images (one per polynomial coefficient), and calculation of first and second time derivatives from the synthetic coefficients are straightforward.

Slope and correlation coefficient R^2

By plotting the equation (34), the trend is the following (Figure 3.7-2):

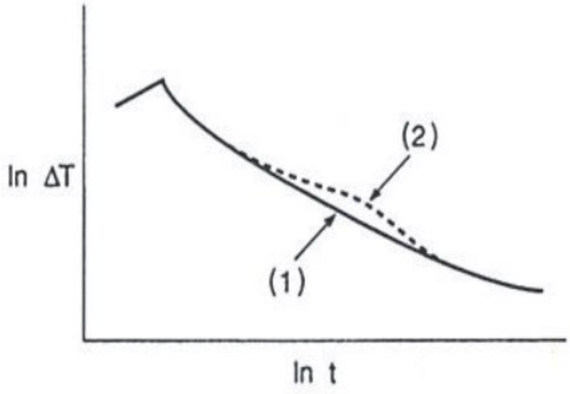

Figure 3.7-2: Trend of cooling curve in a double logarithmic scale

If there is a defect in the depth (sub-surface) (2), the decay of the temperature variation is "deviate" from the homogeneous condition without defects and, in general, the slope is different from $(-1/2)$. In the presence of a defect, it is possible to notice a deviation of the cooling curve from a linear trend in a double logarithmic diagram, such as shown in Figure 3.7-2. A measure of this deviation is the square correlation coefficient R^2 [42].

Principal component thermography

As explained above, the Fourier transform provides a valuable tool to convert the signal from the temperature-time space to the phase-frequency one by the use of sinusoidal basis functions, which may not be the best choice for representing transient signals, that are the tipical temperature profiles found in pulsed thermography. Singular value decomposition (SVD) is an alternative tool to extract spatial and temporal data from a matrix in a compact or simplified manner. Instead of relying on a basis function, SVD is an eigenvector-based transform that forms an orthonormal space. SVD technique is close to the principal component analysis (PCA) with the difference that SVD simultaneously provides the PCAs in both row and column spaces.

The SVD of an MxN matrix A $(M > N)$ can be calculated as follows [43]:

$$A = URV^T \tag{35}$$

where U is a MxN orthogonal matrix, R being a diagonal NxN matrix (with singular values of A present in the diagonal), VT is the transpose of an NxN orthogonal matrix (characteristic time).

Hence, in order to apply the SVD to thermographic data, the 3D thermogram matrix representing time and spatial variations has to be reorganized as a 2D MxN matrix A. This can be done by rearranging the thermograms for every time as columns in A, in such a way that time variations will occur column-wise while spatial variations will occur row-wise. Under this configuration, the columns of U represent a set of orthogonal statistical modes known as empirical orthogonal functions (EOF) that describes the spatial variations of data [43, 44]. On the other hand, the principal components (PCs), which represent the time variations, are arranged row-wise in matrix VT. The first EOF will represent the most characteristic variability of the data; the second EOF will contain the second most important variability, and so on. Usually, original data can be adequately represented with only a few EOFs. Typically, a 1000 thermogram sequence can be replaced by 10 or less EOFs.

3.7.3. Evaluation of thermal images

Image processing for automation or other purposes can be divide into three major parts: first, preprocessing of images (noise reduction); second, segmentation (locate relevant information); and third, feature extraction and reduction.

Preprocessing - Noise Reduction

The most important part in any image processing for pattern recognition or image classification is the preprocessing of the raw data. On the one hand, it is necessary to reduce noise and eliminate pixel artifacts in the images; on the other hand, phenomena like distortion, twisting, scaling, or translation can occur regarding the object geometry. This requires the input images to be transformed geometrically.

Noise in IR images is given by random changes of pixel signals caused by single pixel noise as well as fixed pattern noise. The filters used to reduce noise are characterized as low-pass filters. The frequency information refers to the spatial frequency of the system. Fixed pattern noise is characterized by a spatial periodicity referring to the pixel size, which can be regarded as analogous to the wavelength λ. Then, 2π/λ is referred to as wave vector or spatial frequency. A small value λ implies high spatial frequency and vice versa. Obviously, the pixel size is the smallest possible spatial periodicity in IR images, that is, it resembles the highest possible frequency f_{max}. Therefore, fixed pattern noise (as well as single pixel errors) refers to high spatial frequencies. Consequently, it may be reduced by applying low-pass filters, which suppress high frequencies, while at the same time preserving edges and contours. The easiest low-pass filters are just averaging pixels with their neighbor pixels, for example, fixed pattern noise (as well as single pixel errors) refers to high spatial frequencies.

Geometrical Transformations

For comparing a processed object with a reference object (e.g., manufactured products), both must have identical geometrical properties (position and orientation). But before that, it is appropriate to start with the challenging and exciting part of defect detection and image classification. Mathematically, the possible geometric variations are described by projective and affine transformations.

Affine transformations consist of a multiplication of the original Cartesian coordinates by a (2 × 2) matrix and a vector addition to represent a translation.

Segmentation

Typically, the first step after preprocessing is the segmentation of the input data, that is, searching for ROI (region of interest). The main goal is to determine the zones in the image where the relevant information are located. There are several possibilities for the image segmentation like region-growing segmentation, histogram-based segmentation, and edge detection. The decision on which type of segmentation procedure must be applied depends on the concrete goals of the image-processing procedure. In some cases, only a segmentation between foreground and background zones is necessary by using a histogram method; in others, one may need to locate certain objects by edge detection algorithms.

All pixels that are classified as belonging to a ROI have one or more similar properties.

Feature Extraction and Reduction

After the segmentation, that is, defining ROIs in the image, the procedure of feature extraction can start. Pixels in the signal matrix that represent noncontinuous jumps represent existing structures or edges in the image. To emphasize these discontinuities with sizes of the order of 1 pixel a high-pass filtering is needed by applying several local pixel operators.

Most of the different methods used may be grouped into two categories: gradient and Laplacian. The gradient methods detect edges by looking for extreme values (maxima and minima) of the first derivative of the image. In principle, the Laplacian method, which searches for positions where the second derivative of the image becomes zero, is equivalent.

The most important goal of image processing is to find optimal edge detection algorithms. The most popular edge detection procedure is the so-called Canny algorithm, which claims to combine good detection, good localization, and minimal response. This means, that as many existing edges as possible should be marked exactly at the correct position and independent of noise. In addition, no false edges should be detected due to noise or pixel errors.

Pattern Recognition

In some applications, the acquired images contain specific patterns or geometrically parameterizable objects like, for example, straight lines, parabola, circles, and so on. In these cases, a coordinate transformation from the original x-y-space to a so-called Hough space can be applied to extract these patterns. All pixels in the gradient matrix (result of feature extraction) with intensities above a certain threshold are used for the transformation. The simplest case is to search for collinear points or nearly straight lines.

The paragraph has been built based on the references [45–51].

Bibliography

[1] Williams, T. L. 2009. Thermal imaging cameras characteristics and performance. New York. CRC Press Taylor & Francis Group.

[2] Klocek, P. 1991. Handbook of infrared optical materials. New York: Marcel Dekker.

[3] A. Rogalski, “Infrared detectors: an overview,” Infrared Physics & Technology, vol. 43, no. 3, pp. 187–210, 2002.

[4] Holst, G.C. (1993) Testing and Evaluation of Infrared Imaging Systems, JCD Publishing Company.

[5] Holst, G.C. (2000) Common Sense Approach to Thermal Imaging, SPIE Press, Bellingham.

[6] Chrzanowski, K. (2002) Evaluation of commercial thermal cameras inquality systems. Opt. Eng., 41(10), pp. 2556–2567.

[7] Sousk, S., O’Shea, P., and Van Hodgkin (2004) Measurement of uncooled thermal imager noise. Infrared Imaging Systems: Design, Analysis, Modeling and Testing XV, SPIE vol. 5407, pp. 1–7.

[8] Levesque, P., Br´emond, P., Lasserre, J.-L., Paupert, A., and Balageas, D.L. (2005) Performance of FPA IR cameras and their improvement by time, space and data processing. QUIRT-Quant. Infrared Thermography J., 2 (1), 97–111.

[9] Mollmann, K.; Vollmer, M. (2014). Infrared Thermal Imaging: Fundamentals, Research and Applications. Igarss 2014.

[10] Nowakowski A. (2001) Advances in thermography – medical applications, Gdan´skie Publisher, Gdan´sk (in Polish).

[11] Bielecki Z. and Rogalski A. (2001) Detection of optical signals, WNT, Warsaw (in Polish).

[12] Minkina, W., & Dudzik, S. (2009). Infrared Thermography: Errors and Uncertainties. Infrared Thermography: Errors and Uncertainties.

[13] ASTM E 1213-2002. Standard Test Method for Minimum Resolvable Temperature Difference for Thermal Imaging Systems 2002.

[14] ASTM E 1311-2002. Standard Test Method for Minimum Detectable Temperature Difference for Thermal Imaging Systems 2002.

[15] Y.K. Zhu, G.Y. Tian, R.S. Lu, H. Zhang, A review of optical NDT technologies, Sens. Basel 11 (8) (2011) 7773–7798.

[16] The theory of laser material processing. Heat and mass transfer in modern technology. Springer series in material science 119. Ed. J. Dowden, Netherlands. 380 p; 2009.

[17] Standard Practice for Infrared Flash Thermography of Composite Panels and Repair Patches Used in Aerospace Applications.ASTME2582-07;2014.

[18] D'Accardi, E., Palumbo, D., Tamborrino, R., & Galietti, U. (2018). Quantitative analysis of thermographic data through different algorithms. Procedia Structural Integrity, 8, 354–367.

[19] W.B. Larbi, C. Ibarra-Castanedo, M. Klein, A. Bendada and X. Maldague, Experimental comparison of lock-in and pulsed thermography for the nondestructive evaluation of aerospace materials. In 6 th International Workshop, Advances in Signal Processing for Non Destructive Evaluation of Materials (IWASPNDE), Ontario, Canada. Citeseer. 2009, August.

[20] S. Pickering, D. Almond, Matched excitation energy comparison of the pulse and lock-in thermography NDE techniques, NDT E Int. 41 (7) (2008) 501–509.

[21] A. Gleiter, C. Spiessberger, G. Busse, Lockin thermography with optical or ultrasound excitation, J. Mech. Eng. 56 (10) (2010) 619–624.

[22] Zhua Y., Gaoa B., Wua S., Zhangc Y., Wanga M., W.L. Woob, Liaoa Y., A desig of multi-mode excitation source for optical thermography nondestructive sensing, Infrared Physics and Technology 94 (2018) 23–31

[23] X. Maldague, S. Marinetti, Pulse phase infrared thermography, J. Appl. Phys. 79 (5) (1996) 2694–2698.

[24] Maldague X. P. (2001). "Theory and Practice of Infrared Technology for Nondestructive Testing", A Willey-Interscience Publication, New York.

[25] Krapez J., Belegeas D., Deom A., Lepoutre F.(1994). "Early detection by stimulated infrared thermography", Advances in Signal Processing for Nondestructive Evaluation of Materials, vol.22, pp.303-321.

[26] Almond D.P., Petel P.M. (1996). "Photothermal Science and Technique", Chapman & Hall, London.

[27] Yang R., He Y., Optically and non-optically excited thermography for composites: A review, Infrared Physics & Technology 75 (2016) 26–50.

[28] Clemente Ibarra-Castanedo, Marc Genest, J.-M. P., & Stéphane Guibert, A. B. and X. P. V. M. (2015). ACTIVE INFRARED THERMOGRAPHY TECHNIQUES FOR THE NONDESTRUCTIVE TESTING OF MATERIALS. In Active infrared thermography NDT techniques.

[29] Carlomagno G. M. and Meola C. “Comparison between thermographic techniques for frescoes NDT”, NDT&E International, 35:559–565, 2002.

[30] Ibarra-Castanedo, C.; Gonz´alez, D.; Klein, M.; Pilla, M.; Vallerand, S.; Maldague, X. Infrared image processing and data analysis. Infrared Phys. Technol. 2004, 46, 75–83.

[31] Busse, G.: Techniques of infrared thermography: Part 4. Lockin thermography. In: Maldague, X., Moore, P.O. (eds.) Nondestructive Handbook, Infrared and Thermal Testing, vol. 3, 3rd edn. p. 718, ASNT Press, Columbus (2001)

[32] Favro, L.D., Han, X.: Thermal wave materials characterization and thermal wave imaging. In: Birnbaum, G., Auld, B.A. (eds.): Sensing for Materials Characterization, Processing and Manufacuring, ASNT TONES, vol. 1, pp. 399–415 (1998)

[33] Busse, G., Wu, D., Karpen, W.: Thermal wave imaging with phase sensitive modulated thermography. J. Appl. Phys. 71(8), 3962–3965 (1992)

[34] Ibarra-Castanedo, C., Piau, J. M., Guilbert, S., Avdelidis, N., Genest, M., Bendada, A., & Maldague, X. P. V. (2009). Comparative study of active thermography techniques for the nondestructive evaluation of honeycomb structures. Research in Nondestructive Evaluation.

[35] Maldague X. P. and Marinetti S. “Pulse Phase Infrared Thermography,” J. Appl. Phys., 79(5):2694–2698, 1996.

[36] Cooley J. W. and Tukey J. W. “An Algorithm for the Machine Calculation of Complex Fourier Series,” Mathematics of Computation, 19(90):297–301, 1965.

[37] Ibarra-Castanedo C., Bendada A. and Maldague X. “Image and signal processing techniques in pulsed thermography,” GESTS Int'l Trans. Computer Science and Engr., 22(1): 89-100, November 2005.

[38] Ibarra-Castanedo C., González D., Klein M. Pilla M., Vallerand S. and Maldague X. “Infrared Image Processing and Data Analysis,” Infrared Phys. Technol., 46(1–2):75–83, 2004.

[39] Maldague X. P. V., Theory and Practice of Infrared Technology for NonDestructive Testing, John Wiley-Interscience, 684 p., 2001.

[40] Martin R. E., Gyekenyesi A. L., Shepard S. M., “Interpreting the Results of Pulsed Thermography Data,” Materials Evaluation, 61(5):611–616, 2003.

[41] Shepard S. M. “Advances in Pulsed Thermography”, Proc. SPIE - The International Society for Optical Engineering, Thermosense XXVIII, Orlando, FL, 2001, Eds. A. E. Rozlosnik and R. B. Dinwiddie, 4360:511–515, 2001.

[42] Palumbo D. and Galietti U. (2016). Damage Investigation in Composite Materials by Means of New Thermal Data Processing Procedures. Strain 52(4):276-285.

[43] Rajic N. “Principal component thermography for flaw contrast enhancement and flaw depth characterization in composite structures,” Compos. Struct., 58:521-528, 2002.

[44] Marinetti S., Grinzato E., Bison P. G., Bozzi E. Chimenti M. Pieri G. and Salvetti O. “Statistical analysis of IR thermographic sequences by PCA,” Infrared Phys. & Technol., 46:85-91, 2004.

[45] Jaehne, B. (2004) Practical Handbook on Image Processing for Scientific and technical Applications, CRC Press LLC.

[46] Steger, C., Ullrich, M., and Wiedemann, C. (2008) Machine Vision Applications and Algorithms, Wiley-VCH Verlag GmbH.

[47] Gonzalez, R.C. and Woods, R.E. (2008) Digital Image Processing, 3rd edn, Prentice Hall.

[48] M¨ollmann, S. and G¨artner, R. (2009) New Trends in Process Visualization with fast line scanning and thermal imaging systems. Proceedings of the Conference Temperatur, PTB Berlin, ISBN 3-9810021-9-9.

[49] Parker, J.R. (1997) Algorithms for Image Processing and Computer Vision, John Wiley & Sons, Inc.

[50] Russ, J.C. (2007) The Image Processing Handbook, 5th edn, CRC Press Taylor and Francis Group, LLC.

[51] Ballard, D.H. (1981) Generalizing the hough transform to detect arbitrary shapes. Pattern Recognit., 13 (2), 111–122.

4. Concluding Remarks

In Part I, the background of the material included in this thesis has been provided. Chapter 1 motivates the research and presents the included publications.

Chapter 2 gives an introduction to the principles of thermal infrared imaging and its applications.

Chapter 3 gives an overview of the radiation detector principles used in thermal imaging systems: the background knowledge of the operation principles, the limiting factors for the detector performance, and the imaging systems. The acquisition procedure and the processing algorithms have been also introduced for interpretation of the thermal data to extract the features of interest from and there discussed.

The results are presented in the papers in Part II. Discussions from papers are summarized in Section 4.1 and conclusions are provided in Section 4.2.

4.1. Results and Discussion

Case study: Quality assessment of composite bonded joints

The ability of the infrared thermography to characterize defects in adhesively bonded composite joints has been demonstrated in various works [1, 2]. It has been assessed that in general the optical techniques, PT and LT, performed well and were able to detect most defects with acceptable resolution and reliability.

In paper A [3], it has been analyzed, the results of an experimental investigation aimed at determining the capability and reliability of the lock-in thermography as a non-destructive check method for assessing the integrity of glass-fiber reinforced thermosetting plastic (GFRP) adhesive joints used for the construction of wind rotor blades.

The used specimens have been single lap adhesive joints which have been prepared as per ASTM D 3165 standard using glass fiber reinforced thermosetting plastic (vinyl ester GFRP) as substrate and a two part epoxy adhesive: AME6000 INF (Ashland Composite Polymers) and ADH 90.91 (Altana Electrical Insulation). Adherends were characterized by multiple layers of quadriaxial 0 ° / +45 ° / 90 ° / -45 ° fabric glass fiber and were obtained from a laminate fabricated using the technique of infusion of the resin under vacuum (VARI). The thickness of the adherends is set to a value of 2.5 mm, while the thickness of the adhesive is equal to 0.76 mm

The configuration chosen to implement the lock-in technique is the reflection one: the excitation source and the infrared camera are located on the same side. The inspection has regarded the entirely surface of the specimens. The set-up used (Figure 4.1-1) is coherently with what described in section 3.6.1, Figure 3.6-1. In particular two 500W halogen lamps provided the heating flux emitting sinusoidal of 0.00125Hz frequency. A preliminary test has been carried out to assess the optimum value of the modulation frequency, the value that ensure the right thermal diffusion length to reach the defects, according to theoretical explanation reported in section 2.3.1 and resumed in Equation (13).

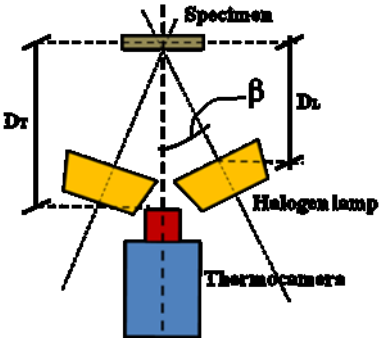

Figure 4.1-1: Top view of set-up used for lock-in thermography (β = 30°, DT = 30 cm, DL = 20 cm) [3]

The FLIR T640 infrared camera has been used in the experiment, equipped with a focal plane array (640 x 480 pixels) uncooled microbolometer detector. The spectral range is from 7.5 to 14μm.

Its temperature measurement range is from -40 °C to 2000 °C and the NEDT < 0.035°C at 30°C enables quick and accurate imaging of targets.

A rule of thumb for lock-in acquisition is to acquire almost 100 frames per cycle and for the reported experimental study the number of cycles was three, so with a simple calculation the acquisition rate to be use was between 2 and 3 Hz. Since the maximum frame rate of the chosen camera is fixed at 30 Hz, it surely allowed to perform the required acquisition frequency [4].

The small FOV (25° x 19°) of the camera, for a 24.6mm focal length of the lens, allows a good spatial resolution of the IR image necessary to compare the thermographic results with the ultrasonic results.

The discrete Fourier transform (DFT) has been used to extract amplitude and phase information from LT acquired data. In the extracted phase images the defects appear with a different phase signal respect to the homogeneous material, moreover the phase of thermal wave is related directly to defects depth (Figure 4.1-2).

Finally, a simple segmentation algorithm, based on a threshold derived from a statistical analysis of data, has been implemented to search for ROI (region of interest) and to determine the defected zones in the phase images.

In Figure 4.1-2, pictures of the broken specimens are reported and compared with the non-destructive results (thermographic investigation and ultrasonic one). Mechanical tests were conducted according to ASTM D3039. For samples whose images give a response symptomatic of the absence of imperfections in bonding (white areas), the observation of the optical photos after the breakup confirms the goodness of the bonding, as in the case of samples that show the presence of defects (black areas), which appear located in the identified positions and with correct shapes and size. The dotted red lines, drawn in Figure 4.1-2, help to recognize the bonded/debonded area.

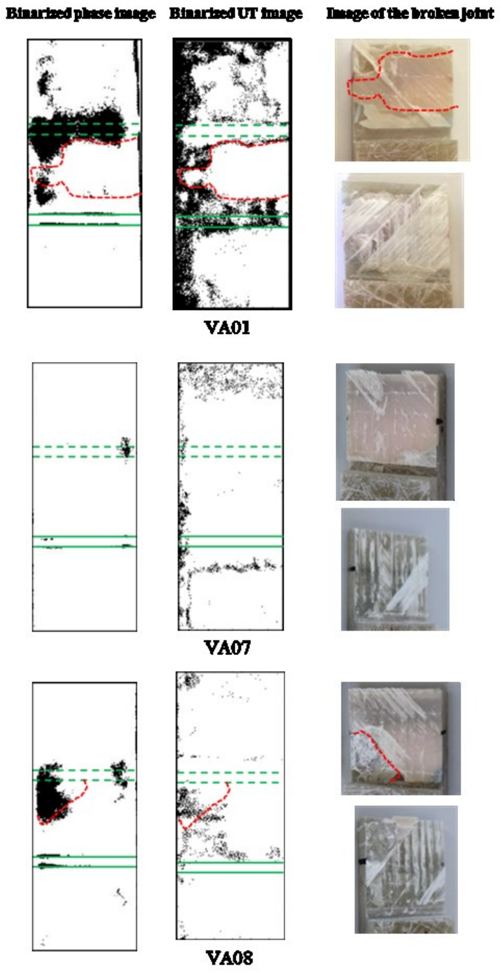

Figure 4.1-2: Phase images, UT images and images of the broken joints of three investigated samples [3]

The goodness of the choices made in implementing the thermographic technique is proved by the agreement of lock-in thermographic results with the results of the well established UT C-scan inspection and those from the mechanical tests.

Case study: Investigation of dynamic thermal behavior of opaque building elements

In Paper B [5], the thermography technique is proposed to study the thermal behavior of opaque walls by adopting an innovative set up based on an active/stimulated thermography. In literature, a passive approach technique was already applied for thermal behavior evaluation of opaque building walls, but exclusively with regard to thermal transmittance and not for dynamic regime analysis. The aim of paper B is to evaluate the effectiveness of stimulated thermography on studying the dynamic behavior of opaque elements, delegating to a successive work the optimization of the experimental technique for in situ application.

The proposed procedure is based on the application of a periodic heat source on one side of two walls: one made with an insulating filler of vegetable nature (hemp fibre) and one without this insulation. The stimulation applied returns that one of the thermographic lock in technique. The schematic representation of proposed experimental set-up is shown in Figure 4.1-3.

Two thermal camera have been employed: Flir T620 and Flir A20 thermocameras.

The first camera has a focal plane array uncooled microbolometer detector (640 × 680 pixels image resolution) and it is sensitive in the spectral range from 7.8 to14 µm. Its thermal sensitivity is less than 0.04°C at 30°C; the range of measurements is from −40°C to 650°C and it is calibrated within an accuracy of +/– 2°C or +/– 2% of reading. The maximum frame rate is fixed at 30 Hz. The FOV is (25° x 19°), for a 24.6mm focal length of the lens [4].

The second one, Flir A20, has a focal plane array uncooled microbolometer detector (160 × 120 pixels image resolution, spectral range from 7.5to 13 µm, thermal sensitivity less than 0.05°C at 30°C, range of measurements from −40◦C to 150◦C with an accuracy of ±5°C . The FOV is 19° x 14°/0.3 m (with 17 mm lens). Its maximum frame rate is equal to 60 Hz [4].

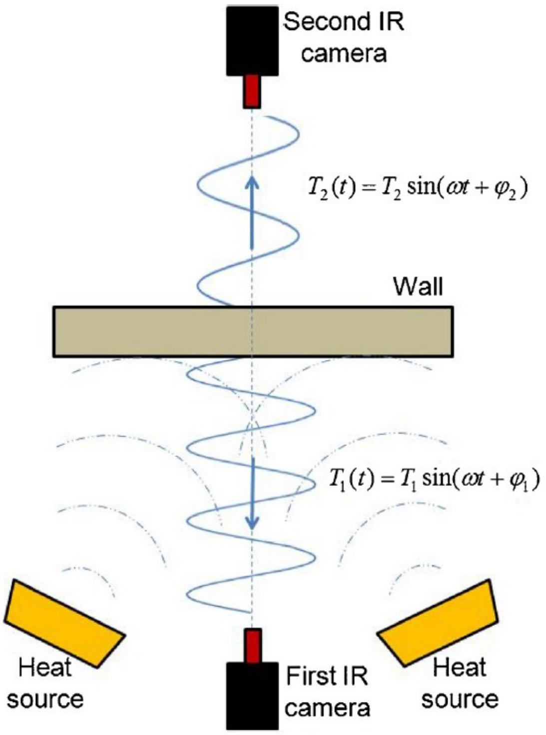

Figure 4.1-3: Schematic representation of experimental set-up proposed to study the thermal behaviour of the wall [5].

The performance parameters of the two cameras are quite different. In particular, the thermal camera Flir T620 seems to be more performant regarding the thermal sensitivity and achievable the spatial resolution. However, this experimental study doesn't need a high performance thermal imaging system because the interest is versus mean measurements of the involved quantities. Hence, the cost of the investigation can be reduced by choosing a cheaper infrared sensor.

Two 1000W halogen lamps have been provided the heating flux, emitting a periodic square wave signal for three cycles. In this case, each cycle consisted in 4h working period and 4h pause period of the lamps; therefore the overall duration of wall stimulation has been 24 h.

Simultaneous acquisitions, on the front and rear side of the wall, of the thermal signal has been made by means of the two infrared cameras with a same frame rate of 0.033 Hz for both of them.

The thermographic data acquired have not been processed by using the usual algorithm dedicated to lock in analysis as the knowledge of the time lag, the time shift between the maximum temperature peaks, and the decrement factor, the ratio between the oscillation amplitude of the temperatures, are necessary for evaluating the dynamic behavior of the walls. The values of the temperatures have been directly obtained by the thermal sequences. In particular, the emissivity of surfaces has been taken equal to 0.92 with a good approximation.

In Figure 4.1-4 are shown the results obtained with the proposed experimental procedure in terms of temperature evolution in front and rear side of the two considered walls. In particular, the trend of the max value of temperature on the heating area at the center of the wall has been considered Figure 4.1-5.

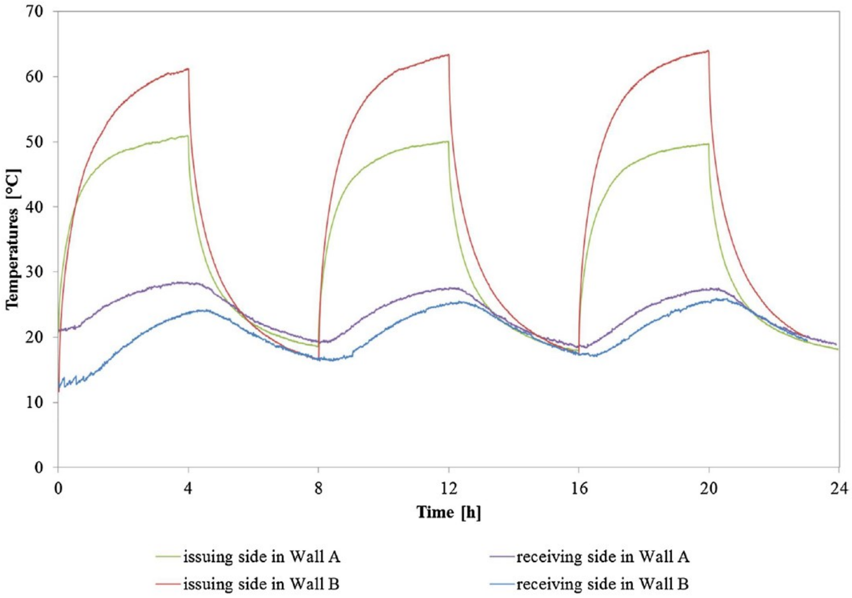

Figure 4.1-4: Comparison among temperatures for both the sides of prototype walls [5].

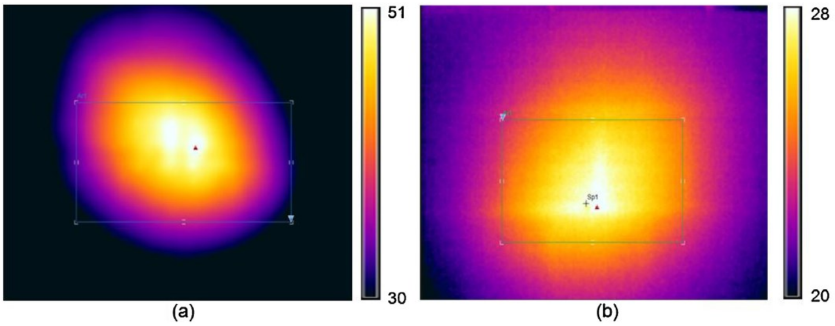

(a) (b)

Figure 4.1-5: Thermographic images of the wall (Temperatures in◦C): Temperature map on the side of input stimulation (a) and temperature map on the side of output response(b) [5].

The presence of the hemp fibres determines an increasing of time shift between the temperature waves with respect to the shift for the empty brick (19 min) and a decreasing in the decrement factor (32%, defined as the difference between the decrement factors on the filled and the empty walls, with respect to the empty one), therefore improving the thermal behavior of the wall.

Case study: Adhesion quality and thickness measurement on Thermal Barrier Coating (TBC)

The thermographic techniques used to achieve the outcomes in paper C [6] are the both pulsed thermography and stepped/long pulsed one. The outcomes are the detection of the adhesion defects among the base material and the Thermal Barrier Coating (TBC), and the thickness of TBC evaluated by an appositively developed empirical thermographic method to discriminate between an unevenness of the thickness and a defect zone.

A TBC system contains two thermally different solid materials in which Zirconia is a thermally resistive ceramic and a nickel supper alloy which is a thermally conductive metal. The thermal conductivity of nickel–super alloy is 7 times greater than Zirconia. Differences in thermal conductivity between TBC and the substrate cause significant changes in the surface cooling. This difference can be advantageously used for the application of transient thermography to TBC systems. Moreover, the propagating heat front in a thin and thick coating will have different distance to reach the highly conductive substrate. The applied signal processing techniques have been thought in order to take advantage of this thermophysical difference to investigate damages in the adhesion and to evaluate the thickness of the coating by analyzing thermal profile during the cooling stage.

The specimens used are ten discs with metallic bondcoat and a ceramic topcoat which is yttria stabilized zirconia (YSZ), deposited by High Velocity Oxy Fuel (HVOF) technique. They have different thickness. Two of these have been realized with an adhesion defect (2mm and 5mm of diameter).

The two thermographic techniques have been implemented by using three different set up.

The configuration chosen for all the set up’s is the reflection one: the excitation source and the infrared camera are located on the same side. The inspection has regarded the entirely surface of the specimens.

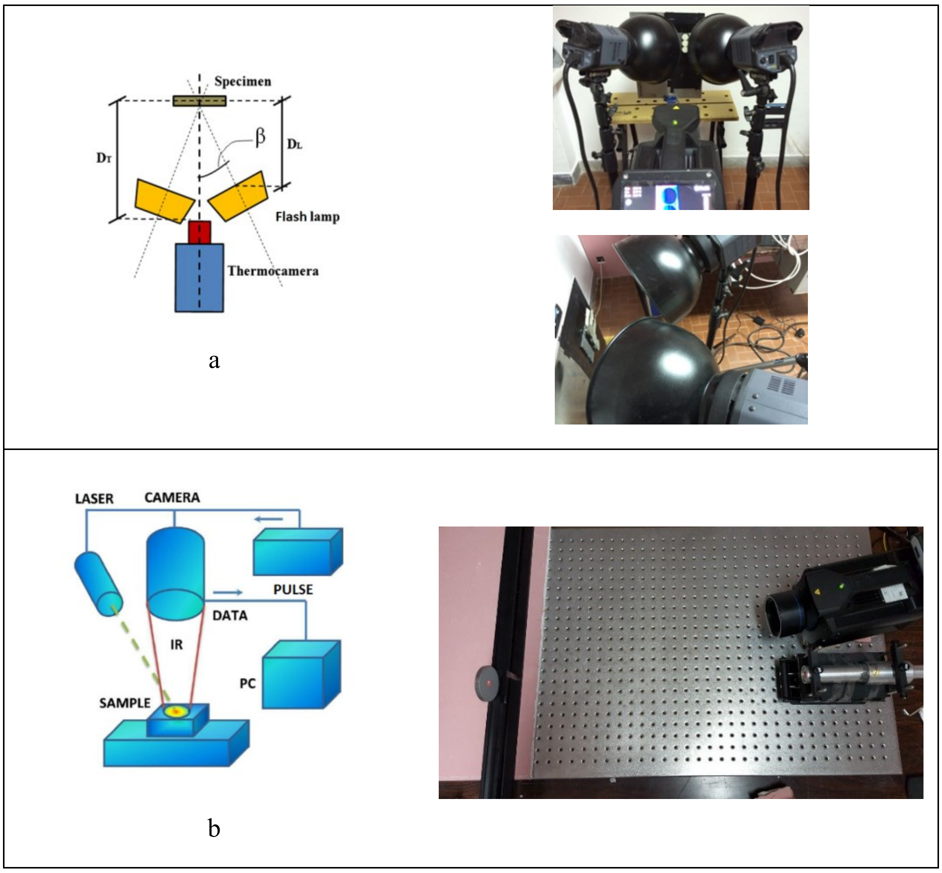

Figure 4.1-6: Experimental set up for thermographic data acquisition. a. Set up referred to flash heating source; b. Set up referred to laser heating source (used with two different diameter of the spot and power) [6]

The three set up's differ for the excitation source, while the thermal detector used is the same. They are shown in Figure 4.1-6.

A flash source (2 flash lamps of power 1500W) generating a pulse of 5ms has been used for implementing the pulsed thermography technique and a 1064 nm wavelength Ytterbium pulsed fiber laser generating a pulse of 500ms for implementing the stepped thermography. The energy and the diameter of the heating shot were fixed equal to 30W and 25mm, to cover the entirely surface of the specimens, respectively. This two different excitation modes (flash lamps and laser beam) have been use for investigating the detachment defects.

The excitation source employed for evaluating the coating thickness is again a 1064 nm wavelength Ytterbium pulsed fiber laser. This time it pulses beams of 100ms, 200ms and 500ms. The energy and the diameter of the heating shots have been fixed equal to 7.5W and 8 mm, respectively: while heating the entirely surface of the specimens is not necessary for evaluating the coating thickness, focusing the laser beam to 8mm needs a reduction of the power to avoid the damage of the material.

The infrared camera used for this study is the same for all the set up: FLIR X6540sc.

It has a focal plane array cooled indium-antimonium detector (image resolution 640 × 512 pixels) and it is sensitive in the spectral range from 3 to 5 μm. Its sensitivity is less than 25mK (18mK typical value); it is calibrated within an accuracy of +/– 1°C or +/– 1% of reading. The maximum image frequency (full frame) of the camera is 126 Hz, but it is possible adopting a windowing (reduction of the size of the frame) to change the frame rate up to very high frequency [4]. This last is a useful characteristic for this study in which it has been necessary to acquire with a frame rate of 300Hz for the pulsed technique an 150Hz for the stepped/long pulsed technique.

As above cited, the presence of the defects determines a modification of thermal profile during cooling stage with a typical non-linear behavior. In particular, the sound areas show a different behavior of the temperature decay curve respect to the defective areas: indeed, the cooling curves of the defective areas are more linear. Thermal data have been processed using the algorithms described in section 3.7.2 in order to obtain slope and R-Square images, which describe objectively the trend of the cooling curve. The thermal images obtained have been also post processed using a segmentation algorithm to quantify the dimension of the defected area. The results are reported in Figure 4.1-7 and Figure 4.1-8.

Slope (Diameter of defect 2mm)	Slope (Diameter of defect 5mm)
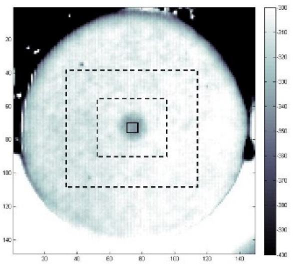	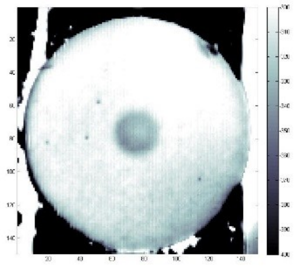
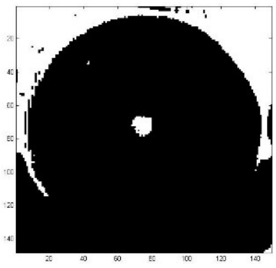	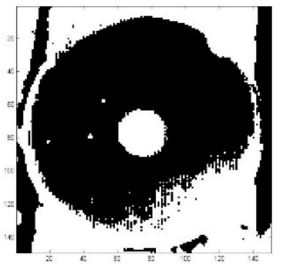
R- Square (Diameter of defect 2mm)	R- Square (Diameter of defect 5mm)
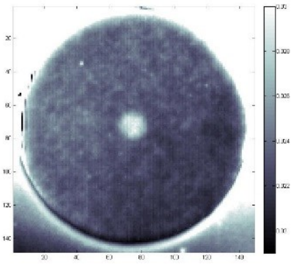	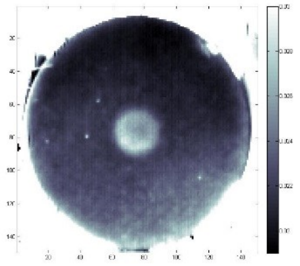
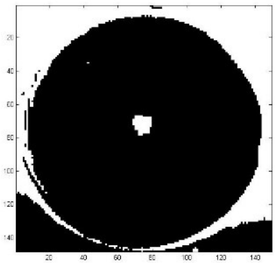	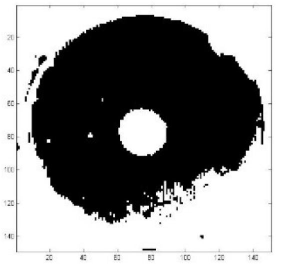

Figure 4.1-7: Maps of slope and R-Square obtained by thermographic data coming from flash-pulsed investigation for the two defected sample (diameter of defects 2mm and 5mm) [6].

Slope (Diameter of defect 2mm) | Slope (Diameter of defect 5mm)

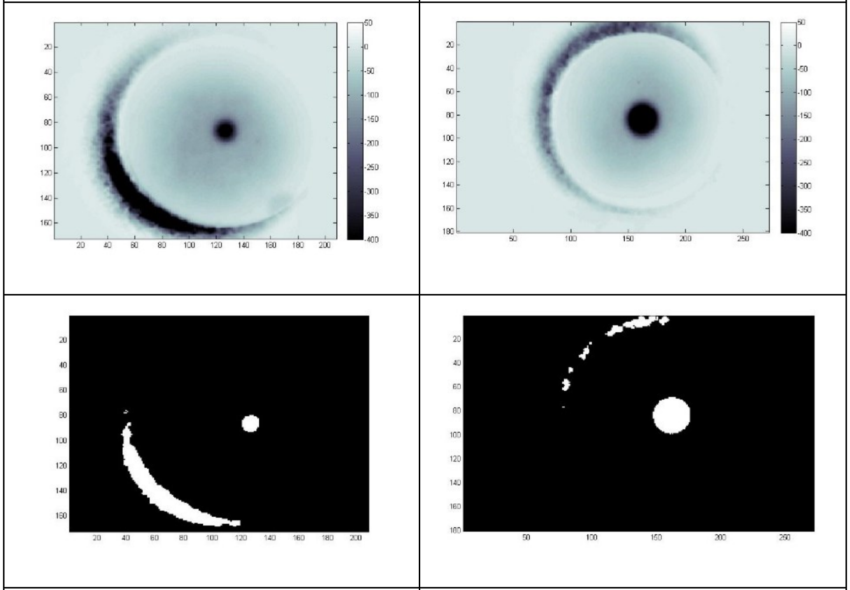

R-Square (Diameter of defect 2mm) | R-Square (Diameter of defect 5mm)

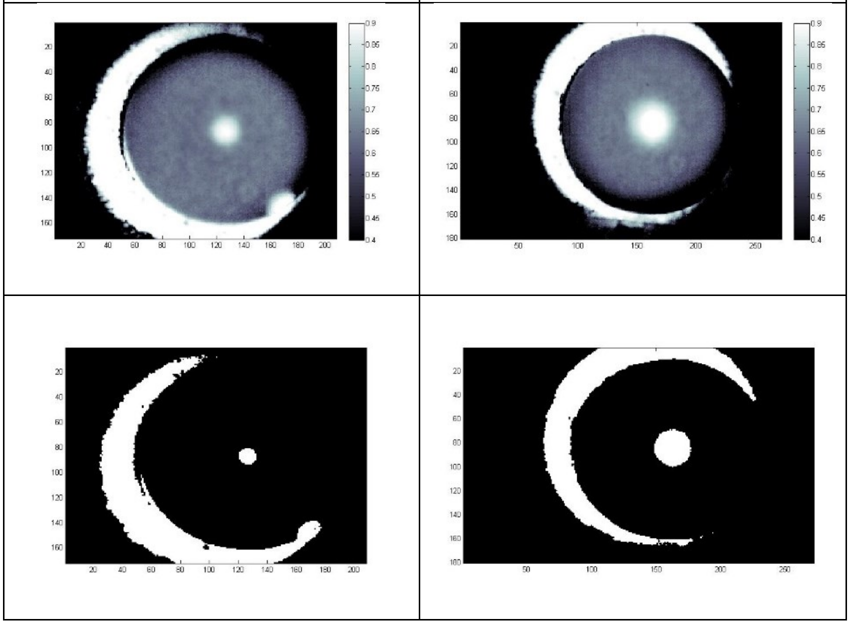

Figure 4.1-8: Maps of slope and R-Square obtained by thermographic data coming from laser-stepped investigation for the two defected sample (diameter of defects 2mm and 5mm) [6].

Also the variation of thickness emerges by processing the thermal sequence with the algorithm to extract the slope of the cooling curves. The slope results a good indicator to discriminate the different thickness. It has been demonstrated that a quadratic relationship exists between the coating thickness and the slope of the cooling curves (Figure 4.1-9).

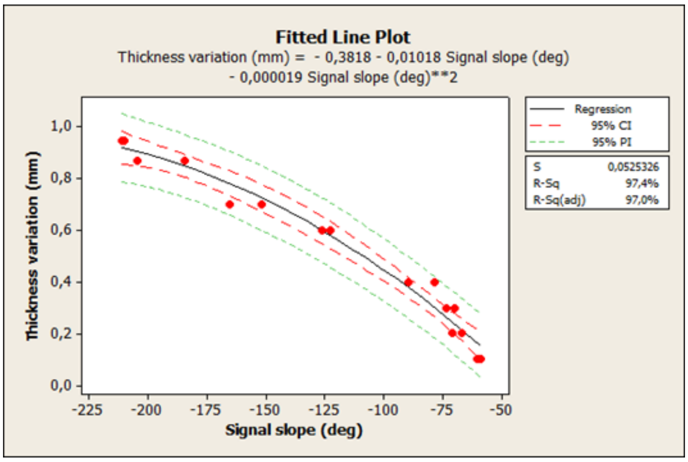

Figure 4.1-9: the second order polynomial model of the TBC thickness as a function of the slope values [6].

The proper use of infrared thermography allows for evaluating defects and thickness in TBC.

Case study: Thickness evaluation of tungsten carbide coatings (WC-Co-Cr)

The approach used in paper C for evaluating TBC thickness has been applied also in paper D [7] for evaluating the thickness of tungsten carbide coatings (WC-Co-Cr) on steel substrates. The metal/metal configuration of this systems is very difficult to investigate by using thermographic techniques because the substrate and the coating have very similar thermophysical properties.

The samples considered in this study are disks composed by a steel substrate with 9.75 mm thickness coated with WC 86% - Co10% - Cr 4%.

A comparison has been made with the performance of the traditional flash excitation technique and the long pulse excitation one: two different setup have been realized.

The first test bench for implementing the pulsed Infrared thermography consists of a flash source (2 flash lamps 1500 W) generating a pulse excitation of duration 5ms and a cooled IR camera (Flir X6540 SC) with an indium-antimonium detector and resolution of 640-512 pixel of resolution, sensitive in the range of 3-5 µm with Noise Equivalent Temperature Difference (NETD) <25mK (Figure 1) [4]. The distance between the camera and the sample is 70 cm. The lamps have been placed as close as possible to the sample. The camera has been used with a lens of 50mm to reach a small spatial target and hence to obtain sufficient spatial resolution.

The use of such a high performance thermal imaging camera has allowed to obtain a reduced window (64x80 pixels) for the observation of the phenomenon, achieving a mm/pixel ratio of 0.19. The windowing is necessary to reduce the acquired data and allow the use of a higher frame rate (980Hz).

The other test bench for implementing the “long pulse” Infrared thermography consists of a 1064 nm wavelength Ytterbium pulsed fiber laser generating a pulse excitation of duration 500ms. The collimated laser spot has a diameter of about 8 mm. The acquisition system of the equipment is an A655 FLIR ‘‘long waves” (7.5–14 µm spectral range) infrared camera selected for its good ratio price/performance. This camera uses an uncooled microbolometeric detector and records the infrared thermal images that have a size of 640 × 480 pixel. Its NETD equals about 30mK. The distance between the camera and the sample is 100cm. The laser source has been placed at a distance of 15cm from the sample and the laser beam hits the sample perpendicularly. The camera has been used with a lens of 13.1mm to reach a spatial resolution of 0.37 mm/pixel. Though the used camera allow to reduce the window of observation, it has been and forced to acquire the thermal sequences at a frame rate of 50Hz, avoiding the windowing. The aim has been to acquire at the most slow frame rate. The two test benches are shown in Figure 4.1-10.

The apparent thermal effusivity algorithm, based on the 1D solution of the Fourier equation for the propagation of a Dirac heat pulse reported in section 2.3.2, has been applied to the thermal sequences obtained by implementing the pulsed thermographic technique. This approach fails because it can not be able to discriminate thickness that are too thin or to thick. Indeed, the apparent effusivity profiles, extracted for the different thickness and reported in Figure 4.1-11, overlap for both thin and thick coating.

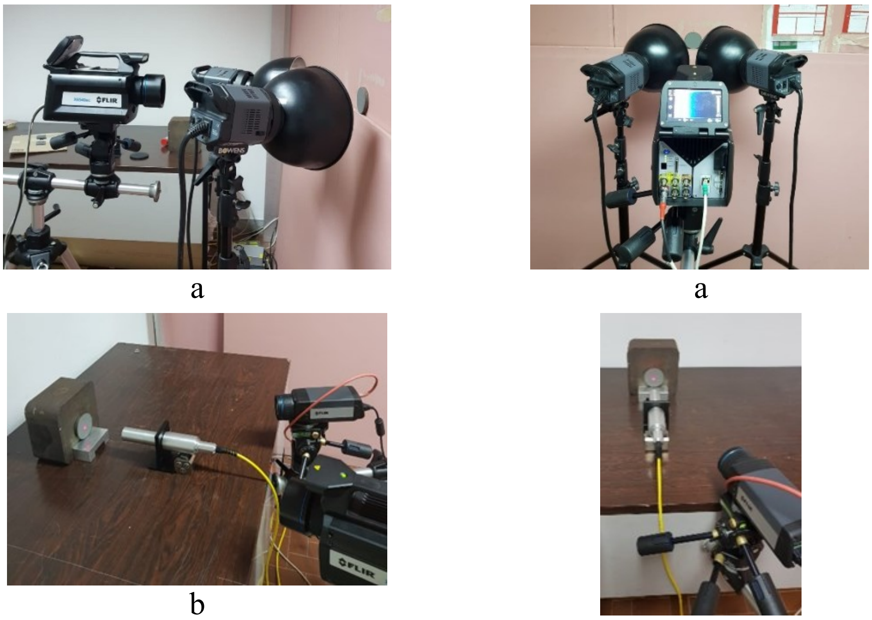
a a

b b

Figure 4.1-10: Pulsed Infrared thermography setup (a) and “Long pulse” Infrared thermography setup (b) [7]

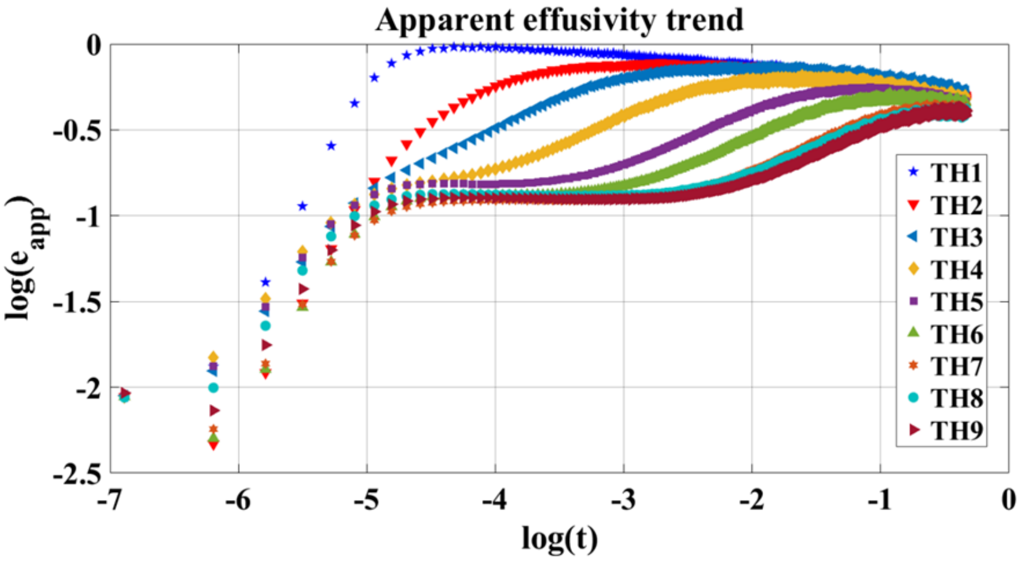

Figure 4.1-11: Influence of the variation of the thickness of the coating on the apparent effusivity profiles [7].

In the long pulsed thermographic approach, the premise of heating by a Dirac pulse falls and the role that the thermo-physical properties (thermal conductivity, density, specific heat capacity) of the whole sample has in determining the capability of the technique in estimating the coating thickness becomes notable (see section 3.5). The propagation of the heat wave into the test-piece is governed by the thermal properties of the entire test-piece because the long heat excitation involved both the materials constituting the sample (coating and substrate). In this regard, the thickness variation of coating must result in a change of the cooling rate of the material.

By analyzing the cooling curves on a logarithmic scale graphic (Figure 4.1-12), it can be notice that the central portion of the temperature decay has a linear behavior. The value of the slope of the different lines has a correspondence with the different coating thickness. Also, for this kind of coating, it has been demonstrated that a quadratic relationship exists between the coating thickness and the slope of the cooling curves (Figure 4.1-13). Besides, this approach is capable to evaluate all the investigated thickness.

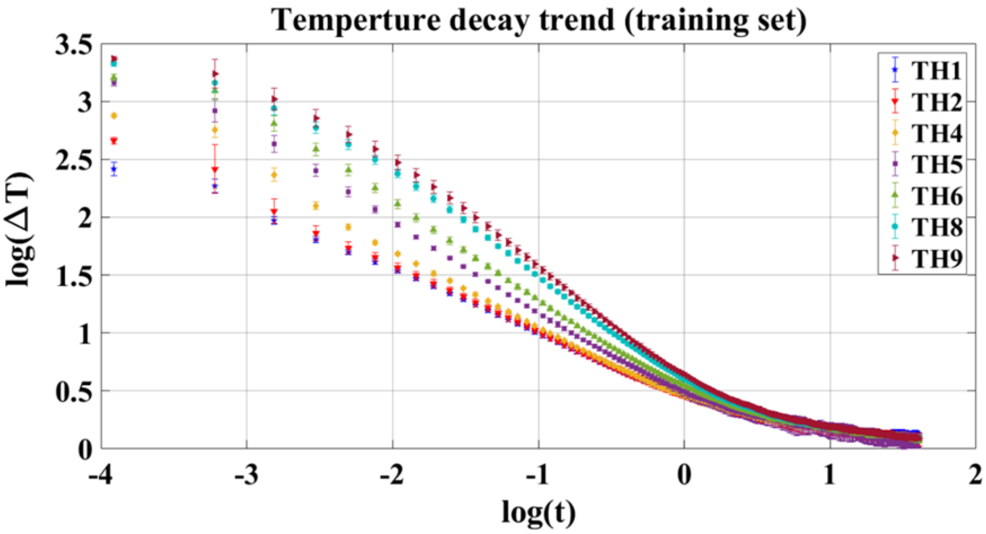

Figure 4.1-12: Mean temperature decay referred to the pixel with maximum temperature of the training samples [7].

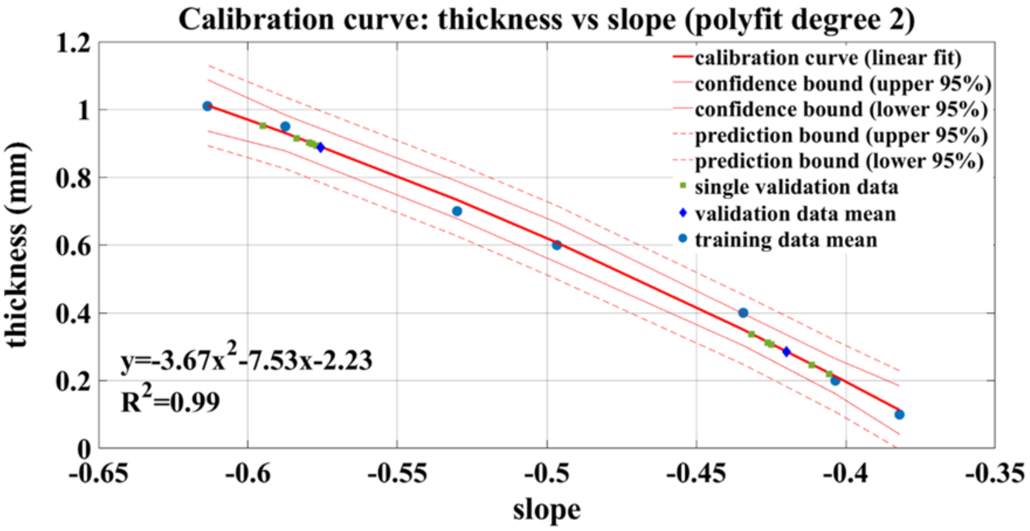

Figure 4.1-13: Data dispersion plot (thickness vs slope) with the estimated regression line (second order polynomial model) [7].

Case study: Thermographic algorithms optimization

Finally, an attention has been dedicated to the long pulse technique and on its capability of accurately detecting defects.

Many workers in the field are aware that this long pulse excitation technique can be effective for some favourable applications.

Thermal images providing by long pulse data acquisition usually involve significant measurement noise and non-uniform backgrounds caused by uneven heating. As a result, it is difficult to recognize the defective regions clearly by naked eyes.

It has been shown how the processing tools, commonly used for pulse-heating, can be applied to step/long-heating, less popular than pulse-heating.

All the algorithms are efficient. In paper E [8], the defect detection efficiency of the slope (m) and the linearity R^2 of the log-log cooling decay will be significantly enhanced adopting an optimizated algorithm to better utilize the spatial information coming from thermographic data. Besides, the fit standard deviation (Sρ) and fit intercept (q) of the log-log cooling curve have been introduced as new indicators of a defective pixel. The performance of the indicators can be appreciate in the images derived by the application of the algorithms to the thermal sequences (Figure 4.1-14). The obtained results have been compared with those deriving from the Thermographic Signal Reconstruction algorithm, TSR (see section 3.7.2) (Figure 4.1-15).

The study has been conducted using experimental data from a campaign of measurements carried out on thermal barrier coatings (TBCs). The defect on which it has been focused the attention is the debonding between the coating and the substrate simulated in cylindrical specimens. The defects have three different diameter: 2mm, 3mm and 5mm.

The test bench for implementing the long pulsed Infrared thermography consists of a 1064 nm wavelength Ytterbium pulsed fiber laser generating a pulse excitation of duration 500ms, and of a cooled IR camera (Flir X6540 SC) with an indium-antimonium detector and resolution of 640-512 pixel sensitive in the range of 3-5 µm with Noise equivalent temperature difference (NETD) <25mK. The camera temperature measurement accuracy is ±1°C or ±1% of reading [4]. The distance between the camera and the sample is 70cm. The laser source has been placed at a distance of 70cm from the sample and the laser beam hits the sample perpendicularly. The camera has been used with a lens of 50mm to reach a small spatial target and hence to obtain enough spatial resolution.

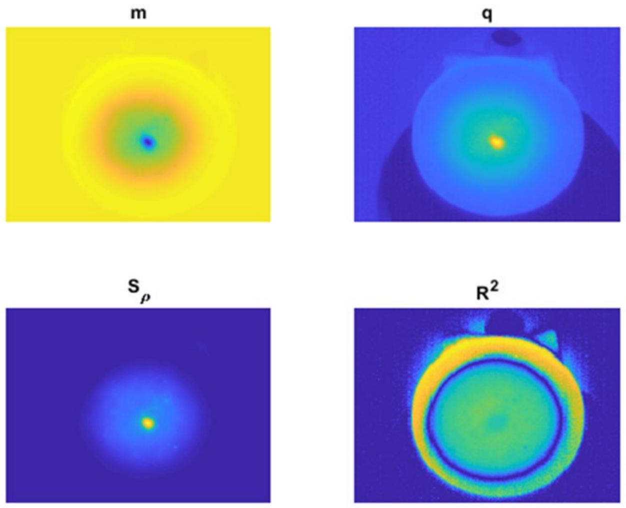

Figure 4.1-14: Linear fit coefficients, according to the proposed technique (diameter of defect 2mm) [8].

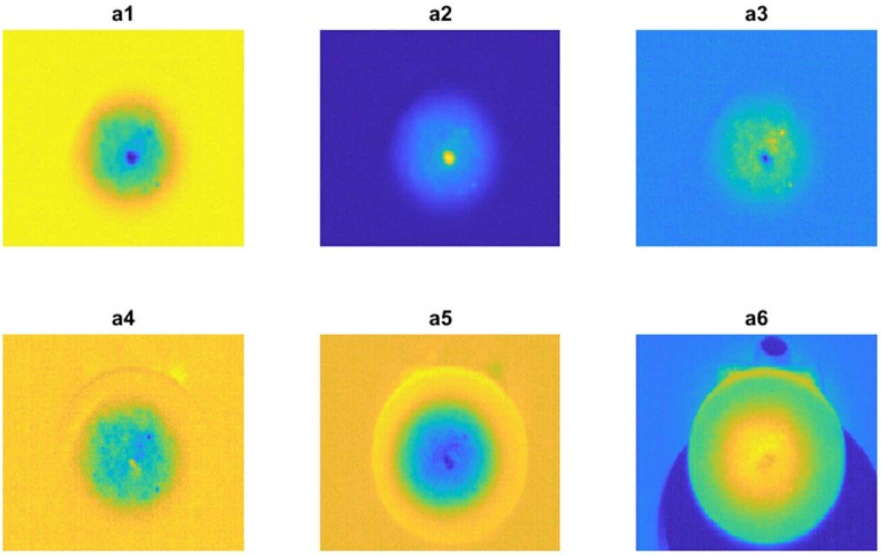

Figure 4.1-15: Coefficient maps from TRS algorithm (diameter of defect 2mm) [8]

Basically, the algorithm is directly applied to the thermographic images indicating the temperature trend of each pixel.

The optimized algorithm not only improves the detection resolution, but also facilitates automated selection of the suspected regions avoiding manual selection.

Further details are discussed in the publications derived from each case study and attached to this thesis.

4.2. Conclusions

Infrared thermography is a fast, clean and safe technology that is used in a wide variety of applications.

A group of active techniques is available for a wide variety of applications. The selection of the most adequate approach depends on the application and the available experimental and expertise resources.

These thesis has implemented infrared thermography in the important fields of non-destructive testing.

The principles and essential theoretical background in this field have been reviewed. This background information are useful in a better understanding of the problems.

Infrared thermography has experienced a great evolution in a relatively short time. Important improvements were achieved in different fields. However, there is a variety of limitations that need to be considered. Infrared thermography is highly dependent on the sensor selection and the experimental setup. It may be affected by the instrumentation and by the environment. These problems can be minimized, but only with adequate setup, testing procedures and processing algorithms, which mostly depend on the operator's skill.

Infrared thermography is a mature technique for varius testing. The case studies show that, with an opportune choice of the experimental parameters, this technology can be employed to detect many types of defects and investigates many type of materials.

Bibliography

[1] Krishnapillai, M., Jones, R., Marshall, I.H., Bannister, M., and Rajic, N., Thermography as a tool for damage assessment. Composite Structures, 67: p. 149-155. 2005.

[2] Dumoulin, J., Ibarra-Castanedo, C., Quiertant, M., Taillade, F., Bendada, A., and Maldague, X. Evaluation of FRP gluing on concrete structures by active infrared thermography. in 10th International Conference on Quantitative Infrared Thermography. Quebec, Canada. 2010

[3] Palumbo, D., Tamborrino, R., Galietti, U., Aversa, P., Tatì, A., & Luprano, V. A. M. (2016). Ultrasonic analysis and lock-in thermography for debonding evaluation of composite adhesive joints. NDT and E International.

[4] https://www.flir.com

[5] Aversa, P., Palumbo, D., Donatelli, A., Tamborrino, R., Ancona, F., Galietti, U., & Luprano, V. A. M. (2017). Infrared thermography for the investigation of dynamic thermal behaviour of opaque building elements: Comparison between empty and filled with hemp fibres prototype walls. Energy and Buildings.

[6] Palumbo D., Tamborrino R., Galietti U.. "Coating defect evaluation based on stimulated thermography", Proc. SPIE 10214, Thermosense: Thermal Infrared Applications XXXIX, 102140X (5 May 2017); doi: 10.1117/12.2267851

[7] 11. Tamborrino R., D’Accardi E., Palumbo D., Galietti U. “A thermographic procedure for the measurement of the tungsten carbide coating thickness.” Under review on Journal of Thermal Spray Technology (Springer)

[8] Dinardo G., Fabbiano L., Tamborrino R., Vacca G. AUTOMATIC DEFECT DETECTION FROM THERMOGRAPHIC NON DESTRUCTIVE TESTING. Proceedings II forum nazionale delle misure 17/19 settembre 2018, Padova

Part II

Included Publications

A Lock-in thermography for debonding evaluation of composite adhesive joints

Abstract

Glass-fiber reinforced thermosetting plastic adhesive joints were characterized through ultrasonic imaging and lock-in thermographic analysis for assessing the adhesion quality before being subjected to static tensile mechanical tests and to accelerated aging cycles.

The mapping of each sample has been obtained. Visual testing were performed on all specimens after the mechanical tests in order to obtain a comparison with ultrasonic and lock-in thermography technique.

A quantitative analysis has been carried out to evaluate the ability of lock-in thermography in investigating inadequate bonding and obtaining the validation of the technique by the consistency of the results with the well-established ultrasonic testing.

Keywords: Glass-fiber reinforced plastic (GFRP), adhesive joints, ultrasonic C-scan, lock-in thermography

1. Introduction

Wind turbine blades are made from polymer composites to provide high specific stiffness, strength, and good fatigue performance. However, large composite structures are prone to manufacturing defects such as delamination and adhesive failure, which can lead to crack initiation and propagation [1].

Adhesive bonding failure is a key manufacturing defect typical of blade joined using adhesives paste of several millimeters thick. In fact, they can be expected to experience significant static and fatigue loads under various environmental conditions over their service life. National renewable energy laboratory, USA statistics shows in Fig.1 that manufacturing defects and in-service damages are the main reason for early blade failure [2].

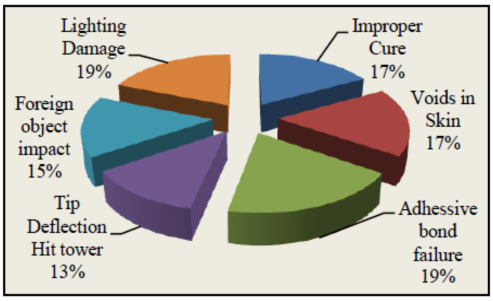

Figure 1. Blade damages at manufacturing and operational stage [2].

Despite great attention given to maintain quality in manufacturing processes, the data available for joints of this class with composite adherents indicate significant sensitivity to adhered properties and surface preparation, adhesive composition (chemistry, additives, mixing, curing), adhesive thickness, temperature, and moisture, as well as joint geometry [3].

Many researchers have done extensive work to identify different types of defects in adhesive joints and have suggested suitable non-destructive test methods to evaluate them [4–8].

Although, the influence of overlapped reflections, scattering and attenuation of the reflected ultrasonic waves from the multi-layered structure appears and the scattering effect also has a negative impact to the propagating ultrasonic waves and requires to use lower frequencies [9], ultrasonic methods have been widely used in the non-destructive testing and inspection of adhesive joints showing a high sensitivity to the defects commonly found in wind rotor blade.

The propagation characteristics of ultrasonic waves are used to determine material properties throughout the volume of turbine blade and to detect and characterize the surface and subsurface flaws and also are suitable for quality control and for estimation of the adhesion level between composite layers. The ultrasonic C-scan imaging can be used for the area mapping of the component [10]. C-scan is 2D image representation using ultrasonic wave signal acquired point-by-point as A-scan signal from the structure. For automated inspection, C-scan system consists of motorized scanner to move ultrasonic probe over the structure. Manual A-scan provides qualitative information whereas C-scan provides quantitative information about damage extent, type of damage, etc [11].

Thermal techniques can be also used to investigate defects in adhesively bonded components [12], [13]. Stimulated Thermography is able to detect defects in homogeneous materials thanks to different thermal behavior that they have if subjected to a thermal stimulation. This behavior is due to the different thermal- physical properties involved in the heat transmission phenomena such as the thermal conductivity, the heat capacity at constant pressure and the density of material [12], [13].

In literature many works regard the application of stimulated thermography for the NDE of FRP strengthening system bonded on concrete structures [14-16]. In these works it was shown the capability of thermography for the estimation of defects and the strong and weak points with respect to other NDT techniques were highlighted.

The ability of thermography to characterized defects in adhesively bonded composite joints was demonstrated in various works [17], [18]. In particular, Genest *et al.*, [19] used flash thermography and a novel signal processing to improve the debond visibility and reduces the influence of the repair edges. The new technique was demonstrated considering simulated and real debonding in CFRP bonded patches. Quantitative analysis shows results in good agreement with ultrasonic and destructive technique.

In the work of Schroeder *et al.*, [20] Pulsed Thermography was used to evaluate large automotive assemblies, composite parts and bonded joints. All tests were carried out with Flash Thermography technique that requires short cycle time and then can be used for on-line tests for part validation.

Johnson [21] proposes a new approach based on TSA (Thermoelastic Stress Analysis) technique to characterized the damage initiation and progression in FRP single lap shear joints. This technique allows to obtain information about the damage extent of material and can be used for the monitoring of damage during the fatigue test.

In this paper we analyze, the results of an experimental investigation aimed at determining the capability and reliability of the lock-in thermography [12], [13], [22], [23] as a non-destructive method of assessing the integrity of glass-fiber reinforced thermosetting plastic (GFRP) adhesive joints used for the construction of wind rotor blades.

Different tests were carried out on single lap adhesive joints designed according to ASTM D 3165 [24], using lock-in thermography and ultrasonic C-scan technique. It was carried out a quantitative analysis in order to evaluate the ability and the advantages of lock-in thermography with respect to the ultrasonic C-scan technique that is considered well established in literature for the debonding detection of joints.

2.Materials and methods

2.1 Specimens

Single lap adhesive joints were prepared as per ASTM D 3165 [24] standard using glass fiber reinforced thermosetting plastic (vinyl ester GFRP) as substrate and a two part epoxy adhesive: AME6000 INF (Ashland Composite Polymers) and ADH 90.91 (Altana Electrical Insulation). Adherends were characterized by multiple layers of quadriaxial 0 ° / +45 ° / 90 ° / -45 ° fabric glass fiber and were obtained from a laminate fabricated using the technique of infusion of the resin under vacuum (VARI). Surface preparation was carried out according to ASTM D 2093 [25] standard for surface preparation of plastics. The panels, properly cleaned and treated, were placed inside a tool for bonding where they were lined up by reference pins. After spreading a thin layer of adhesive, the assembly was closed and the pressure was applied. As regards the conditions of care, they are observed as indicated by the manufacturer of adhesive.

The planar and three-dimensional geometry of the joints are shown in Figure 2.

The single-lap samples were cut from the panels according to scheme imposed by ASTM D 3165.

Since the legislation provided for the use of metals, while the present study is based on adherends in composite materials, changes have been made, in the thickness of the adherends, which are set to a value of 2.5 mm, while the thickness of the adhesive remains equal to 0.76 mm.

A total of 12 single lap joints were used for the experimental tests and they were denoted by the initials VA followed by a sequential cardinal number and the indication of the production lot.

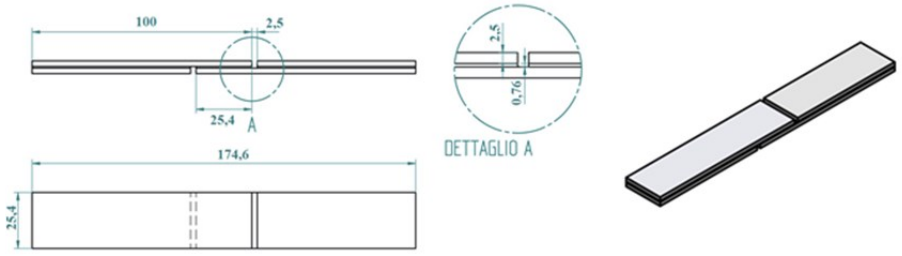

Figure 2. Planar and three-dimensional geometry of the joints

2.2 Hygrothermal aging

The aging cycles for testing were determined on the basis of the monthly average of maximum temperature, minimum temperature, and moisture percentage of the last thirty years in Alpine and Apennines Italian region at about 1500 meters above sea level. The cycle time was 4 months. Within 24 hours there were 3 sub-cycles, which had been assigned a specific weight according to their average duration in a year. The sub-cycles were:

- Cool: the temperature was set to the average of the minimum of the months January, February, March, October, November, December, which was -6 ° C;
- Mild: the temperature was set to the average of the maximum of the months of April and September, corresponding to 5 ° C;
- Warm: the temperature was set to the average of the maximum of the months of May, June, July, August, or 15 ° C.

Figure 3 shows the daily cycle of aging.

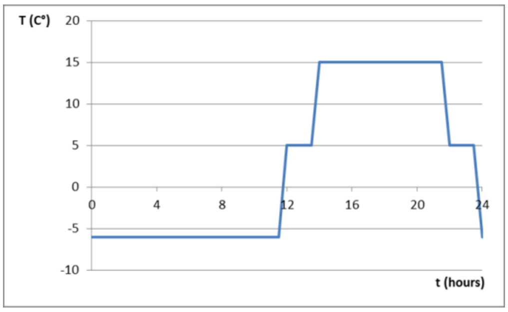

Figure 3. Daily hygrothermal aging: cool, mild and warm sub-cycles within 24 hours

The described accelerated aging was implemented in a climatic chamber.
The 12 adhesive joints studied in this paper were aged for 4 months.

2.3 Ultrasonic testing

Before carrying out thermographic and mechanical testing, all single-lap joint sample were subjected to a volumetric UT scanning analysis procedure. The ultrasonic inspections were performed with an automatic acquisition system developed in the laboratories of ENEA and available in the Brindisi Research Center. The system, by means of a management software implemented in LabVIEW^{TM}, acquires the radio-frequency signal (RF) coming from the instrument through the UT oscilloscope and controls a movement system (two axes at a time) in order to associate the RF signal with the spatial position. At the end of scan, UT data are saved in files containing the whole set of complete UT waveforms. From the UT file, UT images for any portion of the material thickness can be obtained and analyzed. The software allows the visualization in the A-Scan, B-Scan, C-Scan mode.

The experimental apparatus consists of the following elements:

- digital oscilloscope generating the voltage pulses, acquisition, visualization and digitalization of UT pulses;
- transmitter/receiver UT probe;
- PC for UT data processing and mechanical displacement control;
- mechanical displacement system, consisting of a 3-axis for UT probe motioning and control;
- immersion pump for coupling ultrasound with driven jets of water.

The UT inspection technique chosen for this study was the "pulse - echo" and the coupling of ultrasound has been realized with driven jets of water. This choice was necessary to avoid the specimen to stay in the water for not altering the physical and chemical characteristics and for preventing the absorption of water in the material. The probe for this application was a focused immersion transducer of 1 MHz frequency. Water and GFRP material UT speed were 1483m/s and 2578m/s, respectively. The correct focal distance, to focus the UT beam at mid joint, has been established experimentally evaluating the maximum amplitude of the reflected signal.

For each single lap joint sample, a 80 mm x 24 mm area over the bonding was scanned with a 0.2 mm scan step (Figure 4).

The UT scanning was performed before aging the joints and after 4 months aging.

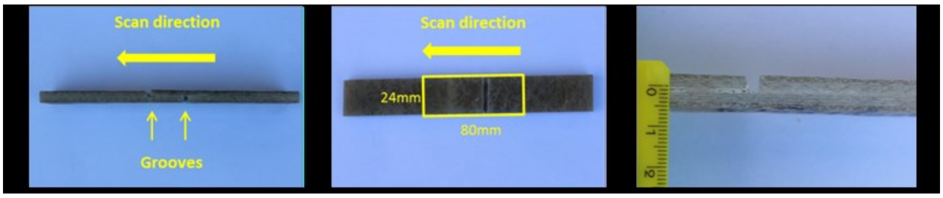

Figure 4. Scan direction and scanned area

2.4 Lock-in thermographic analysis

Lock-in thermography is based on the generation of thermal waves inside the specimen, for example, by depositing heat periodically on the specimen surface [12], [13]. The resulting oscillating temperature field in the stationary regime can be recorded remotely through its thermal infrared emission by an IR camera. Thermal wave can be reconstructed by measuring temperature evolution over the specimen surface: by a suited algorithm, information about magnitude (A) and phase (φ) of the thermal wave can be obtained.

Phase data are relatively independent of local optical and infrared surface features and phase signal allows to penetrate deeper into the material than the analysis of the magnitude signal.

In the phase image, the defects appear with a different phase signal respect to the homogeneous material. Moreover, the phase of thermal wave is related directly to depth z [13]:

$$\varphi(z) = \frac{2\pi z}{\lambda} = \frac{z}{\mu}$$

(1)

with λ thermal wavelength and μ the thermal diffusion length:

$$\mu = \sqrt{\frac{2k}{\omega \rho c_p}} = \sqrt{\frac{2\alpha}{\omega}}$$

(2)

where k is the thermal conductivity, ρ is the density, c_p is the specific heat at constant pressure, ω is the modulation frequency and α is the thermal diffusivity.

Eq. (1) indicates that higher modulation frequencies restrict the analysis in a near-surface region, while low-frequency thermal waves propagate deeper but very slowly [13].

Lock-in thermography tests were performed by IR camera Flir 640 with thermal sensitivity (NETD) < 30 mK and based on a microbolometer detector with 640×512 pixels.

The set-up used is shown in Figure 5 (β = 30°, DT = 30 cm, DL = 20 cm). In particular two halogen lamps with power 500 W were controlled by MultiDES® system in order to heating specimens with a series of sinusoidal waves. Thermal data were processed by IRTA® software in order to obtain amplitude and phase images.

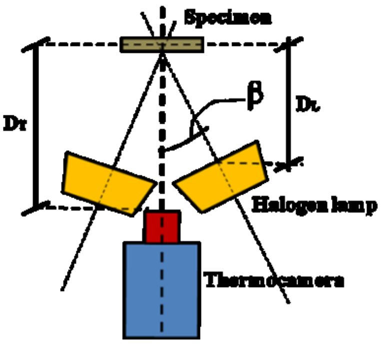

Figure 5. Top view of set-up used for lock-in thermography (β = 30°, DT = 30 cm, DL = 20 cm)

2.5 Mechanical tests

Mechanical tests were conducted according to ASTM D3039 [26]. The tests were carried out at room temperature on the electromechanical machine MTS model Alliance RT/50 available in the laboratory of mechanical tests ENEA. In mechanical testing, bonded joints are loaded to the point of breaking. The rupture of the specimens allowed to validate the results of non-destructive investigations. The broken joints have been visually inspected to locate correctly the defects highlighted with non-destructive controls. Anyway, mechanical tests, so accurately conducted, and their quantitative results will be the subject of a future work.

3. Results and discussion

3.1 Ultrasonic C-scan results

The 1 MHz probe have allowed the complete UT signal penetration of the single-lap joints and the bonded area is reliably observed in the UT images .

All UT images are obtained selecting the distance of the slice from the probe, calculated by the software using the wave propagation speed and the time of flight, corresponding to the joint adhesive layer immediately over the first interface.

C-scan images of the section of interest show, according to the scale, areas with a great amplitude of the reflected signal, and areas with low amplitude of the signal.

The first are indicative of areas in which the bonding has occurred, then the adhesive layer is present. The signal, despite having undergone reflections to the first interface adhering/ adhesive and despite having attenuated crossing the composite material, propagates to adhesive thickness reaching the second adhering/adhesive interface where it was reflected. The signals having low amplitudes indicate areas associated with defects in the adhesive layer. Indeed, in this case the signal has been completely reflected at the first interface adhering/adhesive.

The images make us appreciate significant bond defects in all investigated sample.

In Figure 6, UT images from C-scan of no aged (UT0) and aged (UT4) single-lap joint samples are reported.

Comparing the images, before and after the aging of the same sample, does not appear any variation in the bonding. The comparison suggests that the adhesives yield the same bond quality.

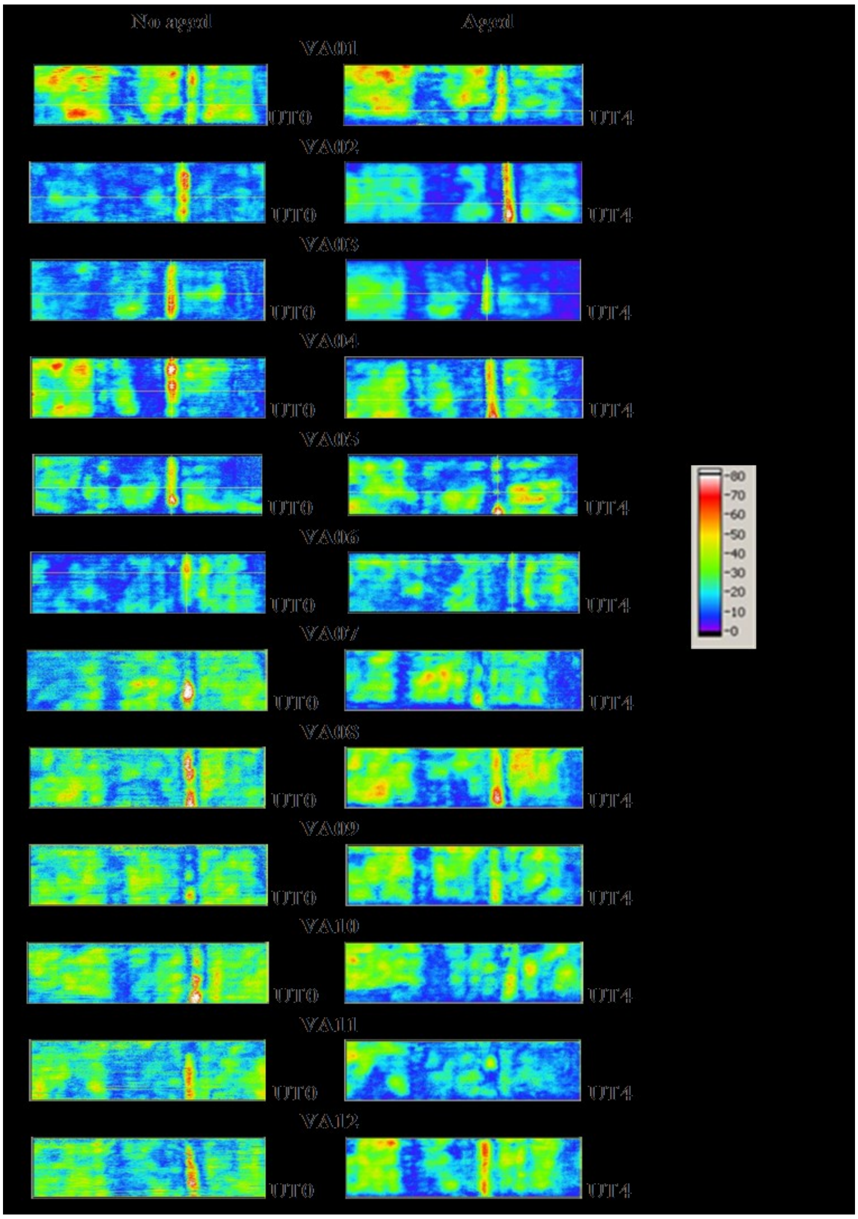

Figure 6. UT images from C-scan of no aged (UT0) and aged (UT4) single-lap joint samples

3.2 Lock-in thermography results

Lock-in tests were carried out considering only one side of specimen and then defect was detected at the first interface adhering/adhesive. Different preliminary tests were carried out on a reference sample specimen, called VA0, in order to assess the optimum value of the modulation frequency for lock-in thermography tests. Debonded area it was simulated by means of a teflon foil inserted between the adhesive and the adherent.

As example, in Figure 7 is shown the phase image obtained with a modulation frequency of 0,0125 Hz on the sample specimen VA0.

The optimum modulation frequency was chosen as the one that gave higher phase contrast $|\Delta\varphi|$ determined as follows:

$$|\Delta\varphi| = |\varphi_{mA_1} - \varphi_{mA_2}| \tag{3}$$

$$\varphi_{mA_1} = mean[A_1] \qquad\qquad \varphi_{mA_2} = mean[A_2] \tag{4}$$

where A_1 and A_2 are respectively defected and sound areas and φ_{mA1} and φ_{mA2} are the mean values of the phase on areas A_1 and A_2, Figure 7.

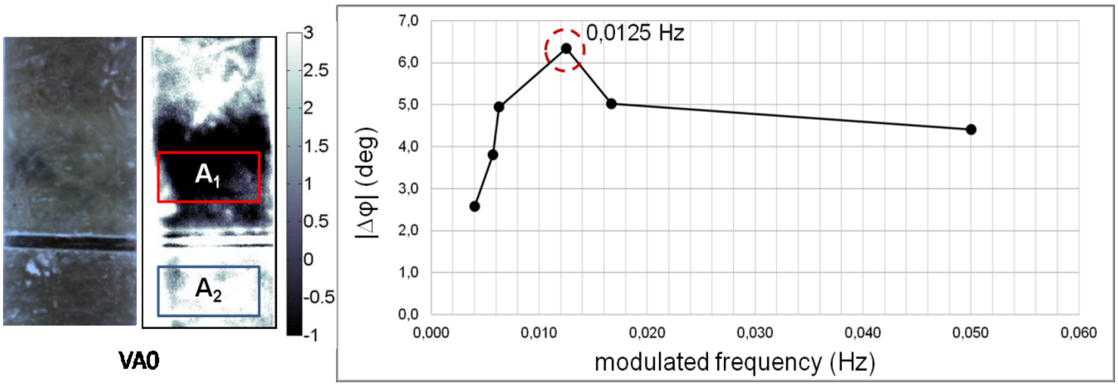

Figure 7. Evaluation of the maximum phase contrast by tests carried out on sample specimen VA0. A_1 and A_2 are respectively defected and sound areas considered for the evaluation of phase contrast.

As shown in Figure 7, 6 different modulation frequencies were used and the max value of phase contrast was obtained in correspondence of 0,0125 Hz. This frequency was then used for all lock-in thermography tests.

Figure 8 shows the phase images obtained by IRTA$^{®}$ software of all specimens before the aging. Black areas indicate the presence of bond defects while green lines delimitate the area of interest. Almost all specimens seem affected by debonding.

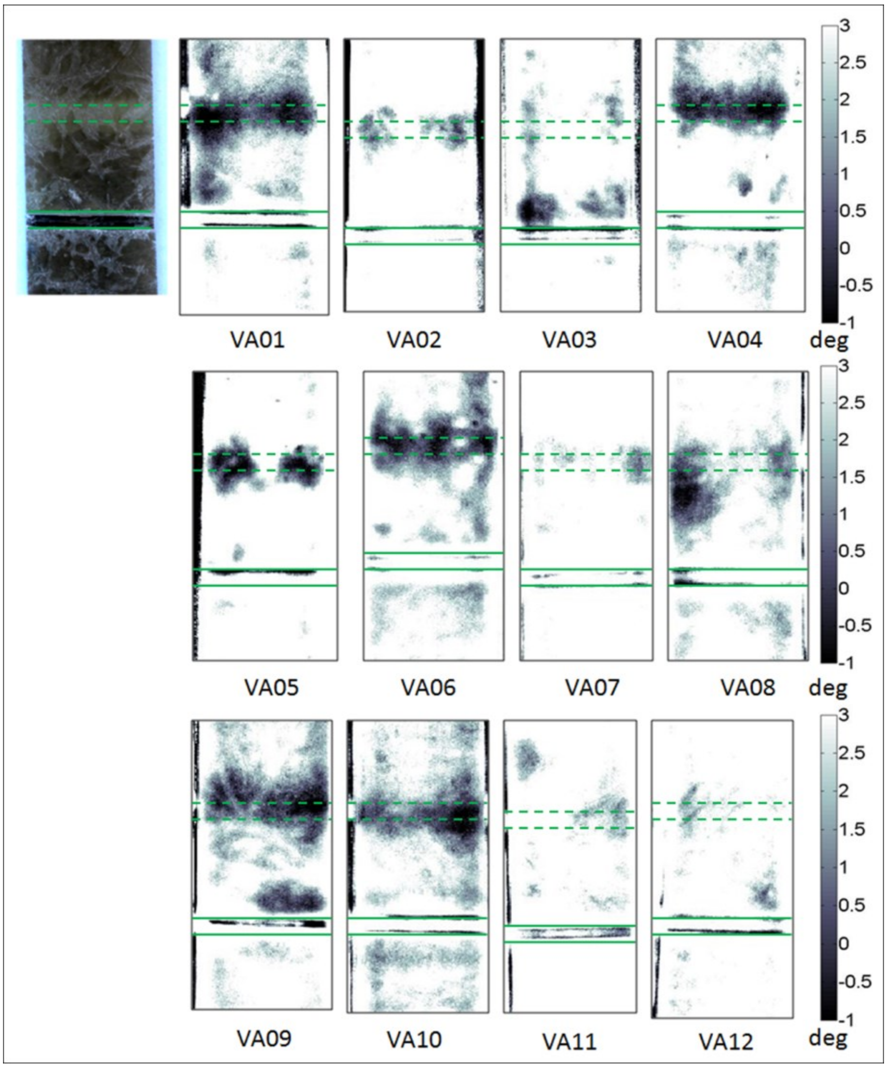

Figure 8. Phase images obtained with the modulation frequency 0,0125 Hz.

4. Discussion of results

4.1 Quantitative data analysis

The quantitative thermographic and UT data analysis was carried out in order to identify the defects using a decision threshold values criterion [27]. In this way, the detectable and undetectable defects are expressed as 1 and 0 (hit/miss data), respectively and it is possible a comparison between techniques.

In this work, the threshold value *Th* was defined through a statistical analysis of data considering the following equation [27]:

$$Th = \mu \pm n\sigma \qquad n = 1,2,........N \tag{5}$$

where μ is the average value of signal measured in the healthy area of material, σ is the standard deviation of the signal measured in the sound area of material and n is a integer number that indicates the width of the confidence intervals.

From the previous paragraphs, both techniques detect, in section of interest between the two grooves, on the specimen VA11, entirely non defected area, thus it was considered as reference for *Th* evaluation. Figure 9 shows the total area *At* used to evaluate mean value and standard deviation of phase and UT data (square dotted line). In particular, indicating with 1 the detected defect and 0 the undetectable one, the hit/miss response is obtained by the following relations:

$$\begin{cases} \varphi \le Th = \mu - n\sigma \Rightarrow 1 \\ \varphi > Th = \mu - n\sigma \Rightarrow 0 \end{cases} \text{for phase data,} \quad \begin{cases} s \le Th = \mu - n\sigma \Rightarrow 1 \\ s > Th = \mu - n\sigma \Rightarrow 0 \end{cases} \text{for UT data} \tag{6}$$

where φ is the phase signal (degree) and s is the UT signal expressed as % signal amplitude.

The area *At* was also considered to quantify the equivalent damage due to debonding defects. In fact, if different debonded areas are present within the total area *At*, an equivalent debonded area can be assessed by hit/miss phase data as follows:

$$A_d = \sum_i^N \sum_j^M \varphi(i,j) \tag{7}$$

where N and M represent the number of rows and columns of the pixel matrix related to the area *At*. In these terms, an expression of equivalent debonded area normalized with respect to *At* area can be provided:

$$A_d\% = \frac{\sum_i^N \sum_j^M \varphi(i,j)}{A_t} * 100 \tag{8}$$

while the equivalent normalized bonded area can be defined as:

$$A_b\% = \frac{\left[A_t - \sum_{i}^{N} \sum_{j}^{M} \varphi(i,j) \right]}{A_t} * 100 \tag{9}$$

Equations (7), (8), (9) can be written in similar way for UT data substituting φ with s. *At* is composed by 8064 pixels for phase data and by 12000 pixels for UT data, Figure 9. For both techniques *n* value was assessed as the smallest number that gives a null defect for the specimen VA11. The *n* values that provide an $A_b\%$ area close to 100% for phase and UT data are respectively 3 and 2.

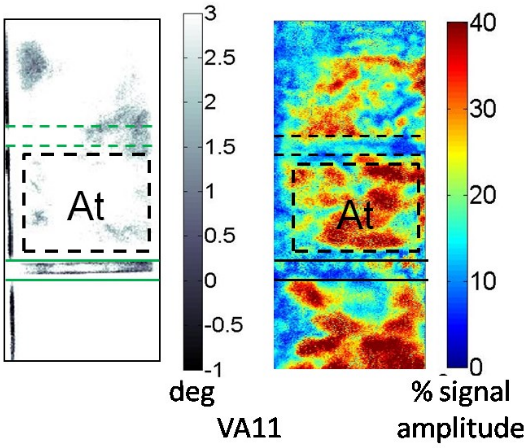

Figure 9. Area (*At*) considered to evaluate the equivalent debonded defect area on phase (left) and UT (right) data.

4.2 Comparison between Lock-in thermography and UT technique

The comparison of images of both NDT techniques, grouped in figure 6 and figure 8, shows a good visualization of defects, allowing us to know their shape and dimensions. Lock-in Thermographic results agree with the ultrasonic inspection, thus its capability to locate and identify defects into bonded joints caused by environmental exposures or manufacturing process can be qualitatively assessed.

As always in NDT, the thermographic (lock-in) technique must be quantitatively validated by a rigorous mathematical argument. Phase images and ultrasonic images processed using the chosen threshold value criterion show almost the same equivalent normalized bonded area (Figure 10).

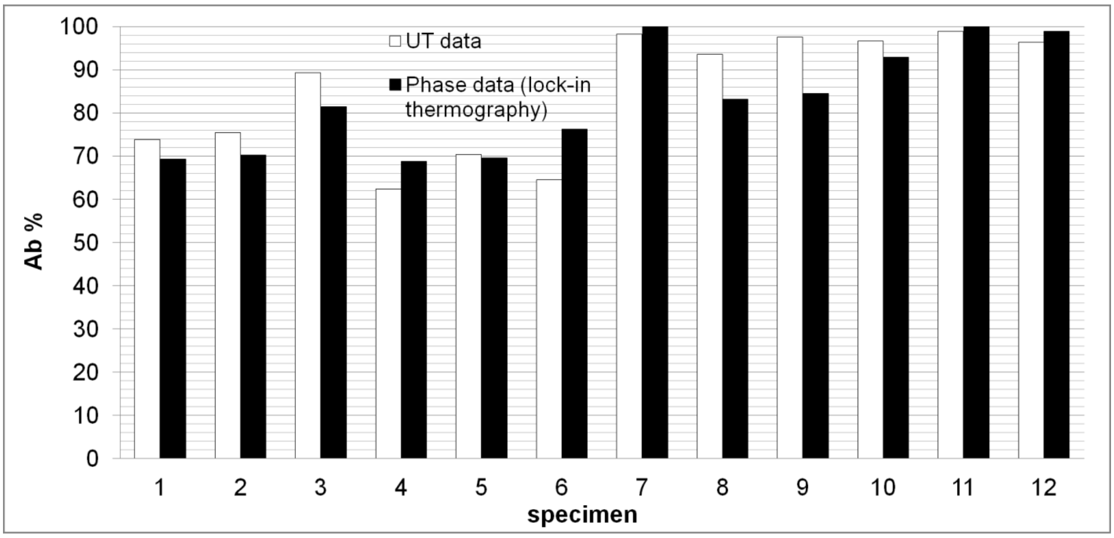

Figure 10. Comparison of equivalent normalized bonded area calculated for both techniques

A further validation of the results of both non-destructive investigation comes from visual inspection of the broken specimens. In Figure 11, pictures of the broken specimens are reported in comparison with the non-destructive results. For samples whose images give a response symptomatic of the absence of imperfections in bonding (white areas), the observation of the optical photos after the breakup confirms the goodness of the bonding, as in the case of samples that show the presence of defects (black areas), which appear located in the identified positions and with correct shapes and size. The dotted red lines, drawn in Figure 11, help to recognize the bonded/debonded area. The specimen VA01 has a large bonded area in the middle, the specimen VA07 is almost completely sound, the specimen VA08 shows a debonded area close to the edge. The small difference in percentage of equivalent normalized bonded area in Figure 10, as well the difference between the images of Figure 11, can be attributed to measurement errors, to the use, however, of different techniques and to the choice of the confidence intervals of different width (*n*) for the definition of the threshold.

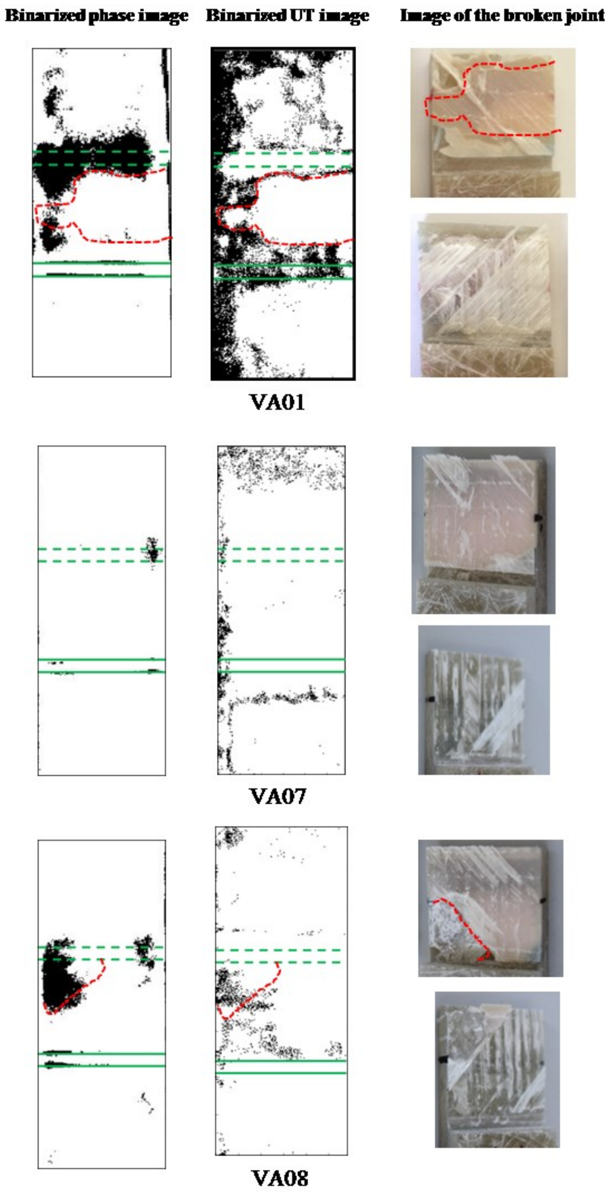

Figure 11. Binarized phase images, binarized UT images and images of the broken joints of the samples VA01, VA07, VA08

5. Conclusions

In the present work the results of an experimental activity have been presented and discussed to determine the capability and reliability of lock-in thermographic techniques as non-destructive testing for the debonding evaluation in glass-fiber reinforced plastic joints.

Different tests were carried out either with lock-in thermography and UT, on single lap adhesive joints designed according to ASTM D3165, before and after a cycle of accelerated aging. Both techniques confirm the presence of defects which were found without an appreciable change in their size and shape.

Ultrasonic C-scan tests were also used in order to validate thermographic results. In this regard, a quantitative analysis was carried out using a decision threshold values criterion. Lock-in thermography provides results in good agreement with UT C-scan inspection and besides, visual inspection, after the rupture of the sample, provides evidence of the results of non-destructive investigations.

Lock-in thermography has shown itself to be an excellent NDT tool to evaluate the condition of an initial, as-manufactured, bonded composite assembly, as well as an effective tool to follow part performance under various environmental conditions. Lock-in thermography can provide information with respect to the ‘correctness’ of the manufacturing process and can give indication of where the process might be improved.

References

[1] Galappaththi UIK, De Silva AM, Draskovic M, Macdonald M, Strategic Quality Control Measures to Reduce Defects in Composite Wind Turbine Blades. International Conference on Renewable Energies and Power Quality (ICREPQ’13), Bilbao (Spain), 2013.

[2] NENUPHAR, Wind farms designed for the offshore environment, June 2010, ABM Centre, 128 rue du Faubourg de Douai, 59000 LILLE – FRANCE.

[3] Mandell JF, Cairns DS, Samborsky DD, Morehead RB, Haugen DJ, Prediction of Delamination in Wind Turbine Blades Structural Details. J. Sol. Energy, 2003; 125(4):522-9.

[4] Adams RD, Drinkwater BW, Non destructive testing of adhesively bonded joints. NDT & E International, 1997; 30(2):93-6.

[5] Dukes WA, Kinloch AJ, Non destructive testing of bonded joints, an adhesion science viewpoint, Non-Destructive Testing, 1974; 7:324-3.

[6] Segal E, Rose JL, Non-destructive testing of adhesive bond joints. Research Techniques in Nondestructive Testing, 1980; Vol. 4, Chapter 8, Academics press, London.

[7] Adams RD, Cawley P, Defects types and non-destructive testing techniques for composites and bonded joints, Construction and Building Materials, 1989; 3:170-14.

[8] Marquez FPG, Tobias AM, Perez JMP, Papaelias M, Condition monitoring of wind turbines: Techniques and methods. Renewable Energy, 2012; 46:169-10.

[9] Gieske JH, Rumsey MA, Nondestructive evaluation (NDE) of composite/metal bond interface of a wind turbine blade using acousto-ultrasonic technique. ASME wind energy symposium, W.Musial and D.E. Berg, eds., AIAA/ASME, 1997; 249-6.

[10] Raisutis R, Jasiuniene E, Sliteris R, Vladisauskas A, The review of non destructive techniques suitable for inspection of the wind turbine blades. Ultragarsas (Ultrasound), 2008; 63.

[11] Avinash SH, Singh NG, Makarand J, Damage detection methodology using ultrasonic non-destructive testing for composites structures. Proceedings of the National Seminar & Exhibitionon Non-Destructive Evaluation, NDE 2011, 2011.

[12] Maldague X, Applications of infrared thermography in non-destructive evaluation. Universitè Laval, Quebec City (Quebec), G1K 7P4, Canada, 2000.

[13] Maldague X, Theory and practice of infrared technology for non-destructive testing. Wiley Series in microwave and optical engineering, Kai Chang, Series Editor, 2001.

[14] Galietti U, Luprano V, Nenna S, Spagnolo L, Tundo A, Non-destructive defect characterization of concrete structures reinforced by means of FRP. Infrared Physics & Technology, 2007; 49:218-6.

[15] Tashan R, Al-mahaidi R, Investigation of the parameters that influence the accuracy of bond defect detection in CFRP bonded specimens using IR thermography. Composite Structures, 2012; 94:519-133.

[16] Taillade F, Quiertant M, Benzarti K, Aubagnac C, Shearography and pulsed stimulated infrared thermography applied to a nondestructive evaluation of FRP strengthening systems bonded on concrete structures. Construction and Building Materials, 2011; 25:568-7.

[17] Omar M, Hassan M, Donohue K, Saito K, Alloo R, Infrared thermography for inspecting the adhesion integrity of plastic welded joints. NDT & E International, 2006; 39:1-7.

[18] Berglind H, Dillenz A, Detecting glue deficiency in laminated wood – a thermography method comparison. NDT & E International, 2003; 36:395-5.

[19] Genest M, Martinez M, Mrad N, Renaud G, Fahr A, Pulsed thermography for non-destructive evaluation and damage growth monitoring of bonded repairs. Composite Structures, 2009; 88:112-9.

[20] Schroeder JA, Ahmed T, Chaudhry B, Shepard S, Non-destructive testing of structural composites and adhesively bonded composite joints: pulsed thermography. Composites: Part A, 2002; 33:1511-8.

[21] Johnson S, Thermoelastic stress analysis for detecting and characterizing static damage initiation in composite lap shear joints. Composites: Part B, 2014; 56:740-9.

[22] Meola C, Carlomagno MG, Squillace A, Vitiello A, Non-destructive evaluation of aerospace materials with lock-in thermography. Engineering Failure Analysis, 2005; 13:380-9.

[23] Montanini R, Freni F, Non-destructive evaluation of thick glass fiber-reinforced composites by means of optically excited lock-in thermography. Composites: Part A, 2012; 43:2075-8.

[24] ASTM D3165: Standard Test Method for Strength Properties of Adhesives in Shear by Tension Loading of Single-Lap-Joint Laminated Assemblies, 2004.

[25] ASTM D2093: Standard Practice for Preparation of Surfaces of Plastics Prior to Adhesive Bonding, 2004.

[26] ASTM D3039: Standard Test Method for Tensile Properties of Polymer Matrix Composite Materials, 2004.

[27] Palumbo D, Ancona D, Galietti U, Quantitative damage evaluation of composite materials with microwave thermographic technique: feasibility and new data analysis. Meccanica, 2015; 50:443-17.

B Infrared thermography for the investigation of dynamic thermal behaviour of opaque building elements

Abstract

The analysis of the thermal dynamic behaviour of buildings is an important tool for reducing inefficiencies and then wasted energy. In this field, European Standards specify the procedures to obtain information about the thermal behaviour of building in terms of decrement factor and time lag. However, these procedures are based on a theoretical approach that does not take into account the real factors involved in the heat exchange phenomena such as the correct knowledge of thermo-physical parameters and the presence of non-homogeneous materials or defects in the investigated walls.

In this work, we propose an innovative experimental procedure based on the application of stimulated thermography with the aim of investigate the thermal dynamic behaviour of walls. In particular, two prototype walls were compared: an empty wall and one made with an insulating filler of vegetable nature (hemp fibre).

The results were then compared with those obtained with a numerical simulation and with the Standard procedure EN ISO 13786:2007, highlighting the differences between the three approaches.

Keywords: infrared thermography, dynamic thermal behaviour, decrement factor, time lag, hemp fibres

Nomenclature

Hereinafter the nomenclature used in this paper (alphabetic order).

c_p	specific heat at constant pressure ($J \cdot kg^{-1} \cdot K^{-1}$)
f	decrement factor
q (or Q)	specific heat flux ($W \cdot m^{-2}$)
$\hat{q}$	amplitude of the specific heat flux ($W \cdot m^{-2}$)
T	period of oscillation (h)
U	thermal transmittance ($W \cdot m^{-2} \cdot K^{-1}$)
Y	thermal admittance ($W \cdot m^{-2} \cdot K^{-1}$)
Z	heat transfer matrix

Greek symbols

δ	periodic penetration depth (m)
ε	emissivity
Δt	time shift (h)
θ	amplitude of the temperature (K)
$\hat{\theta}$	amplitude of the temperature (K)
λ	thermal conductivity ($W\cdot m^{-1}\cdot K^{-1}$)
ν	frequency (s^{-1})
ξ	ratio between the thickness of the layer and the penetration depth
ρ	density ($kg\cdot m^{-3}$)
σ	Stefan-Boltzmann constant ($W\cdot m^{-2}\cdot K^{-4}$)
φ	phase (°)
ω	angular frequency (s^{-1})

Subscripts

eb	brick
fb	filled brick
h	hemp fibre
m	mortar
1	internal wall side
2	external wall sides

1. Introduction

The energy efficiency of existing buildings plays a strategic role in achieving the objectives of "*almost zero consumption*" indicated by the European Directive 2010/31/EU [1]. For this, the analysis or the energy audit of buildings are an effective tool, and even rapid, for new building designs or to take action on the energy renovation of existing buildings, which generally are characterized by inefficiencies that lead to wasted energy. An element on which the energy audit of a building primarily focuses the attention is the wall: an adequate analysis to the adequacy of opaque elements as thermal barriers and the effectiveness of their response to the periodic variation of the temperature and humidity conditions, are mandatory.

On this aspect, the European standard EN ISO 13786:2007 [2] specifies and describes the method for the evaluation of thermal behaviour of building envelopes in dynamic regime, in particular with regard to decrement factor and time lag.

This method is based on the definition of the geometry of the investigated wall and on the knowledge of some physical parameters of the layers of which it is composed (mainly the density, the thermal conductivity and the specific heat). Unfortunately, this theoretical approach does not take into account some factors as inhomogeneous layers with anisotropic thermal properties or the presence of defects inside the wall, which will inevitably make its real behaviour deviate from the theoretical one. For this reason, over the years several theoretical studies for the evaluation of the dynamic behaviour of opaque elements [3-9] have been added to the approach of calculation according to the Standard.

Less numerous is the set of works that study the problem through an experimental approach, adopting different methodologies. Gagliano et al. [10] experimentally studied a massive historical building in Catania (Italy), in order to characterize its thermal performance under dynamic conditions. The research was developed by means of a campaign of measurement of indoor and outdoor air temperatures, inner and outer wall surface temperature, global solar irradiance and wind velocity. The problem related with experimental activities is that the evaluation of the decrement factor and time lag requires an experimental campaign of several days, during which the weather conditions may change greatly (from sunny days to cloudy or rainy days, in the presence or absence of wind), when instead it would be preferable to have a trend of the temperature next to a sine wave and with a constant wind speed.

Ulgen [11] experimentally investigated the thermal behaviours of opaque wall materials under solar energy change, in terms of decrement factor and time lag and by means of temperature sensors for measuring wall surface and environment temperatures. In the works of Pernigotto et al. [12] and Martín et al. [13] the experimental measurements were compared with values come from analytical methodology and some differences were highlighted.

In this work, the thermography technique is proposed to study the thermal behaviour of opaque walls by adopting an innovative set up based on an active/stimulated thermography. Active/Stimulated thermography (ST) is usually used for evaluating defects [14-16] or the different thermal-physical properties involved in the heat transmission phenomena such as the thermal conductivity, the specific and the density

[17]. In literature, ST was used for non-destructive evaluation of FRP strengthening system bonded on concrete structures [18], while a passive approach technique was already applied for thermal behaviour evaluation of opaque building, but exclusively with regard to thermal transmittance and not for dynamic regime analysis [19, 20].

The aim of this work is to evaluate the effectiveness of stimulated thermography on studying the dynamic behaviour of opaque elements specially made for this purpose (prototype walls), delegating to a successive work the optimization of the experimental technique for the *in situ* application. The proposed procedure is based on the application of a periodic heat source on one side of the wall in order to achieve controlled conditions to the contour, avoiding the uncertainty of the climate variability of the measurements carried out in situ. Furthermore, the developed experimental set-up aspires to shorter measurements campaigns than those already implemented in other studies (about 24 hours instead of several days as for Gagliano et al. or Pernigotto et al.). Reducing the duration of the experimental campaign is of considerable importance, particularly in Mediterranean Area, to which this work basically is referred, where temperature and relative humidity can be subject to large variations when the wind direction switches from north to south and vice versa. By reducing the experimental period, the probability to face with this issue is lower.

More specifically, two prototype walls have been compared: one made with an insulating filler of vegetable nature (hemp fibre) and one without this insulation, with the aim of evaluating the effects induced by the hemp fibres in terms of dynamic behaviour of an opaque element. In this purview, it is worthy to note that the specific heat of the hemp is higher than that of mineral wools, favouring the summer-time cooling in buildings, highly recommended in Mediterranean Area.

Numerical simulations with Comsol Multiphysics® software were used as support to the experimental analysis and for evaluating the influence of boundary conditions. In addition, the Standard EN 13786:2007 was also used to determine the main properties related to thermal dynamic transfer.

Finally, a discussion about the thermal properties obtained by adopting the experimental procedure and those suggested by Standard is proposed in order to analyse the possible relations between the thermal parameters adopted by the two methods.

2. Materials and Apparatus

Two wall prototypes were realized for the experimental investigation:

- "Wall A" composed by 16 commercial hollow bricks purchased by Wienerberger (80×250×250 mm with 10 hollows arranged in two rows and whose sizes are 40×30×250 mm) and plastered on both the sides with 10 mm of commercial mortar purchased by Kerakoll (*Biocalce® intonaco*). Its final dimensions are 100×1000×1000 mm (Figure 1).
- "Wall B" composed by 9 commercial hollow bricks purchased by Wienerberger (80×250×250 mm with 10 hollows arranged in two rows and whose sizes are 40×30×250 mm), whose hollows were filled with natural hemp cultivated in Apulia region of Italy, and plastered on both the sides with 10 mm of commercial mortar purchased by Kerakoll. Its final dimensions are 100×750×750 mm. It is important to specify that the natural hemp was heterogeneous in size and not subjected to carding treatment.

Figure 1 highlights an axonometric projection of the wall A.

The thermal conductivity of the hollow brick was measured with a guarded hot plate apparatus, model EP500e, supplied by Lambda Meßtechnik GmbH Dresden and in accordance with Standard ISO 8302 [21] and EN 12664:2001 [22]. The density of the hollow brick was calculated as the ratio between its mass and its volume. The experimental apparatus used for thermographic investigation was composed by (Figure 2):

- 1 Thermal camera Flir T620 with uncooled microbolometer detector (image resolution 640×680 pixels, spectral range from 7.8 to 14 μm, thermal sensitivity less than 0.04 °C, range of measurements from -40°C to 150 °C with an accuracy of ±2 °C and picture frequency equal to 30 Hz);
- 1 Thermal camera Flir A20 with uncooled microbolometer detector (image resolution 160×120 pixels, spectral range from 7.5 to 13 μm, thermal sensitivity less than 0.05 °C, range of measurements from -40°C to 150 °C with an accuracy of ±5 °C and picture frequency equal to 60 Hz);
- 1 thermo hygrometer for temperature and air humidity detection (Capetti Elettronica);
- 2 halogen lamps (power = 1000 W) controlled by MultiDES® (DES srl, Bari, Italy) system for the thermal stimulation of the prototype walls with a series of square waves;
- ResearchIR Max software by FLIR® used to extract the temperature values from the thermal sequences.

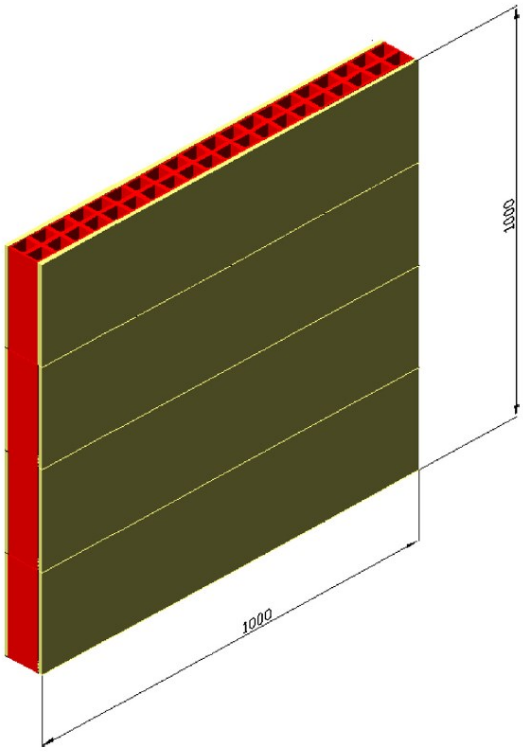

Figure 1: Axonometric view of the prototype wall A

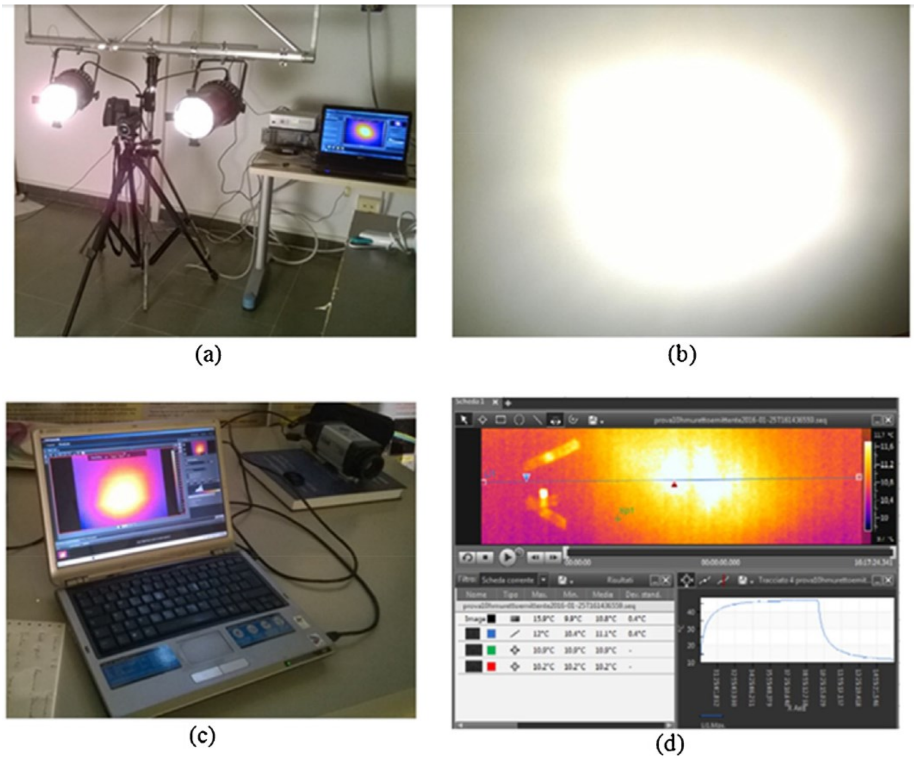

Figure 2: Halogen lamps (a), irradiated side of the wall (b), thermocamera image acquisition (c) (d) in the experimental set-up

3. Methods

3.1. Experimental procedure with the thermographic approach

An experimental procedure for the evaluation of the decrement factors and the time lags of temperatures using a thermographic approach was set up. It is fair to point out that our basic goal is to develop a simple and rapid experimental procedure for studying the thermal dynamic behaviour of prototype walls delegating to a further work the validation for the *in situ* application.

The proposed procedure is based on the application of a stimulated periodic heating by means of a heat source located in front of the investigated wall and on simultaneous acquisition of the thermal response of material in both the sides of the wall. By analysing the temperature signal acquired with the two infrared (IR) cameras, it is possible to obtain information about the main properties related to thermal dynamic heat transfer of the wall. In Figure 3, a schematic representation of the experimental procedure proposed to study the thermal behaviour of the wall is shown. $T_1(t)$ and $T_2(t)$ are the temperature signals acquired by the two IR cameras on the front and the rear face of the wall, respectively called "issuing" and "receiving" sides. These signals differ each other for different values of the amplitude (T_1, T_2) and phase (φ_1, φ_2) and are obtained by applying a modulated heating with frequency $v=\omega/2\pi$.

More deeply, the proposed procedure forecasts:

1) thermal stimulations by means of a heat source. In this case, 2 halogen lamps (1000 W power for each of them) were used and focused at the centre of the prototype wall involving an approximately circular area with diameter of 50 cm. The wall was situated at a distance of 120 mm far from the ground, to reduce the heat dispersion by thermal conduction (Figure 4);
2) conditioning of the test room for the entire duration of the test with the aim to ensure a constant indoor temperature (in this case about 20°C for "Wall A" and about 11°C for "Wall B").
3) Application of a periodic square wave signal for three cycles. In this case, the lamps were switched on for 4 hours and switched off for the subsequent 4 hours (period of 8 hours); therefore the overall duration of wall stimulation was 24 hours. A square wave shape is preferred because it allows to obtain results comparable with the sinusoidal wave by using a simple on/off control of the heat sources [14].

4) Simultaneous acquisition, on the front and rear side of the wall, of the thermal signal by means of two infrared cameras. The same frame rate of 0.033 Hz was adopted for both IR cameras.
5) Analysis of the thermographic data in order to obtain the decrement factor f_θ as the ratio between the oscillation amplitude of the temperatures realized on both sides (eq. 1) and the time lag Δt_θ as the time shift between the maximum temperature peaks (eq. 2). Indicating with θ and φ the temperature and the phase, respectively, they are:

$$f_\theta = \frac{\hat{\theta}_2}{\hat{\theta}_1} = \frac{\theta_{2\,max} - \theta_{2\,min}}{\theta_{1\,max} - \theta_{1\,min}} \quad (1)$$

$$\Delta t_\theta = \frac{\varphi_2 - \varphi_1}{\omega} = t(\theta_{2\,max}) - t(\theta_{1\,max}) \quad (2)$$

The values of the temperatures were obtained by thermal sequences by setting the object parameters on RIR Max software. In particular, the emissivity of surfaces was considered with a good approximation equal to 0.92.

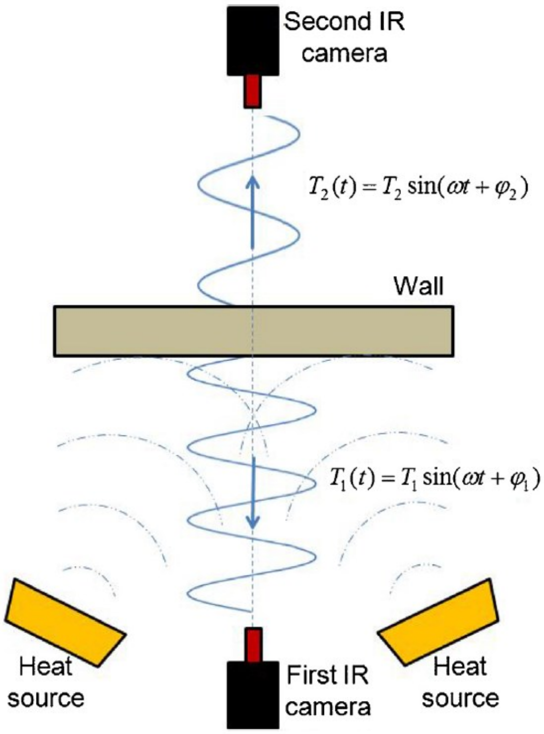

Figure 3: Schematic representation of experimental set-up proposed to study the thermal behavior of the wall

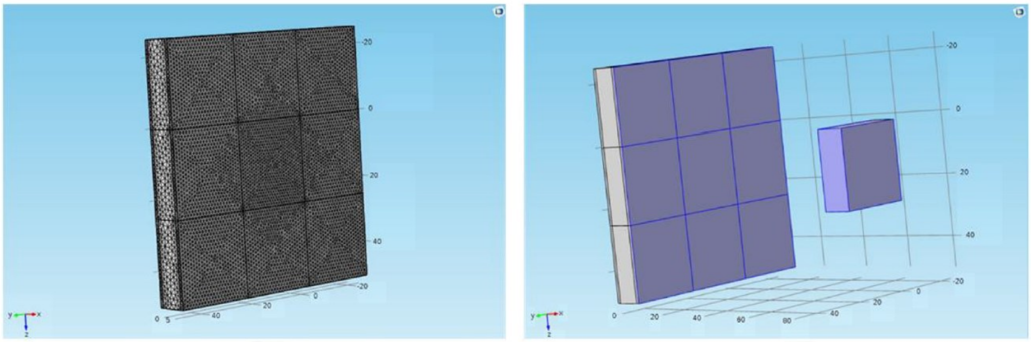

(a) (b)

Figure 4: Numerical simulation with Comsol Multiphysics®: mesh used for the analysis, surface and heat source considered for the heat transmission

3.2. Numerical simulation

A numerical simulation was carried out with the aim to obtain a term of comparison with the proposed procedure and to develop a useful tool capable to simulate in a rapid way different wall configurations.

By using Comsol Multiphysics® software a wall, with dimensions of 750x750x100 mm and schematic profile illustrated in Figure 5, has been considered in order to evaluate different parameters. The mesh used is composed by 195783 tetrahedral type elements with an element size between 0.2 and 12 mm (Figure 5a).

The equation used to simulate the dynamic behaviour of the brick is the general heat conduction Fourier equation:

$$\rho C_p \frac{\partial T}{\partial t} - \lambda \nabla^2 T = Q \tag{3}$$

where ρ is the density of material, C_p the specific heat at constant pressure, λ the thermal conductivity coefficient and Q is the external heat source. The only surfaces of the brick involved in heat transmission are the frontal ones while all the others are considered adiabatic (Figure 5b). By neglecting the convective heat transmission, the heat exchange of the two surfaces with its surrounding environment is due to the thermal irradiation, so the boundary conditions are:

$$-\boldsymbol{n} \cdot (-\lambda \nabla T) = \varepsilon \sigma (T_{amb}^4 - T^4) \tag{4}$$

where ***n*** is the versor normal to the surface, ε is the emissivity (placed in this case to 0.92), σ is the Stefan-Boltzmann constant and T_{amb} is the room temperature.

In order to reproduce the heating conditions similar to the experimental adopted set-up, a heating element has been considered and placed in front of the wall (Fig. 5b). In particular, the power of the source has been regulated until to obtain, on the front surface of the wall, the temperature amplitude measured in experimental tests by using lamps.

The results have been obtained by applying a square wave heat source for three cycles having a period of 8 hours.

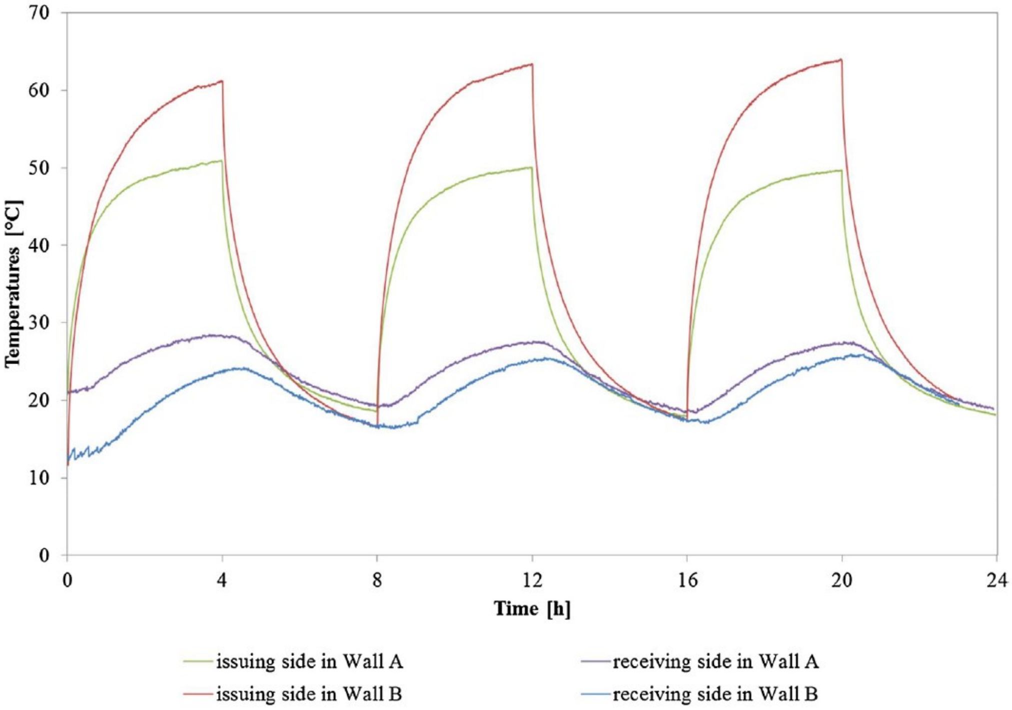

Figure 5: Experimental procedure: Comparison among temperatures for both the sides of prototype walls

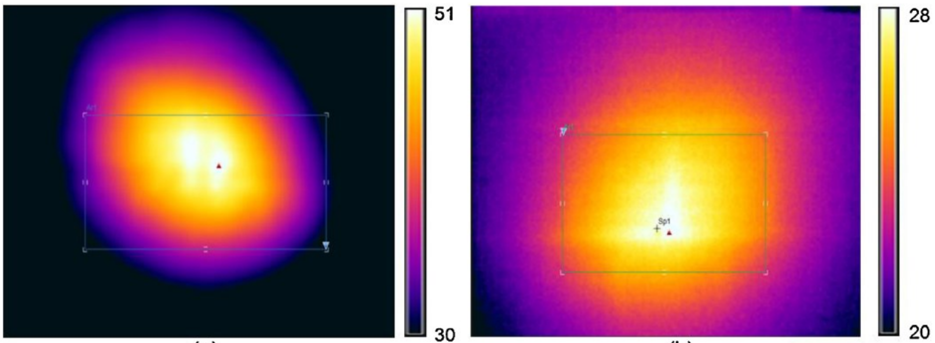

(a) (b)

Figure 6: Thermographic images of the wall (Temperatures in◦C): Temperature map on the side of input stimulation (a) and temperature map on the side of output response(b)

3.3. Calculation according to EN ISO 13786:2007

The thermal dynamic transfer properties of the prototype walls were also investigated considering the Standard EN ISO 13786:2007. This allows the calculation of the main properties related to the thermal dynamic transfer, taking into account different boundary conditions with respect to those considered for the experimental procedure. In this regard, the aim is to obtain a possible relation with the results obtained with the experimental procedure and the numerical simulation.

According to Standard, the main properties related to thermal dynamic heat transfer are basically the decrement factor f, defined as the ratio between the periodic thermal transmittance and the thermal transmittance U_0, and the time shift of periodic thermal transmittance Δt_{12}:

$$f = \frac{|Y_{12}|}{U_0} \tag{5}$$

$$\Delta t_{12} = \frac{T}{2\pi}\arg(Z_{12}) \tag{6}$$

where they are:

$$Z_{12} = -\frac{\delta}{2\lambda}\{sinh(\xi)cos(\xi) + cosh(\xi)sin(\xi) + j[cosh(\xi)sin(\xi) - sinh(\xi)cos(\xi)]\} \tag{7}$$

$$|Y_{12}| = \frac{\hat{q}_1}{\hat{\theta}_2} \tag{8}$$

in which δ and ξ are the periodic penetration depth and the ratio between the thichness of the considered layer and the periodic penetration depth, respectively.

Other important parameters, very useful in this case for comparison with the experimental results, were the temperature amplitude factor $|Z_{11}|$, i.e. the amplitude of the temperature variations on one side resulting from an amplitude of 1 K on the other side, and the time shift between temperatures on both sides Δt_{11}, determined as:

$$Z_{11} = cosh(\xi)cos(\xi) + jsinh(\xi)sin(\xi) \tag{9}$$

$$\Delta t_{11} = \frac{T}{2\pi}\arg(Z_{11}) \tag{10}$$

The data required to compute the dynamic thermal properties are the detailed drawings of the wall, and, for each material used, the thermal conductivity λ, the specific heat capacity c_p and the density ρ.

Both the wall A and Wall B were considered for the calculations performed in accordance with the Standard EN ISO 13786:2007.

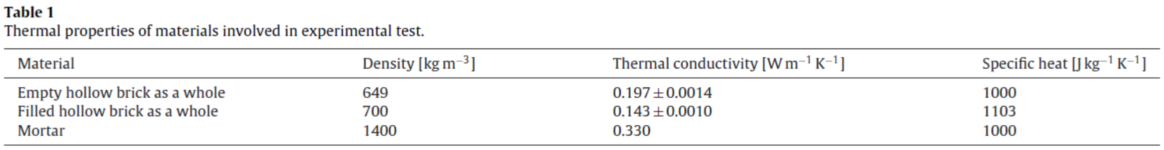

Table 1
Thermal properties of materials involved in experimental test.

Material	Density [kg m^{-3}]	Thermal conductivity [W m^{-1} K^{-1}]	Specific heat [J kg^{-1} K^{-1}]
Empty hollow brick as a whole	649	0.197 ± 0.0014	1000
Filled hollow brick as a whole	700	0.143 ± 0.0010	1103
Mortar	1400	0.330	1000

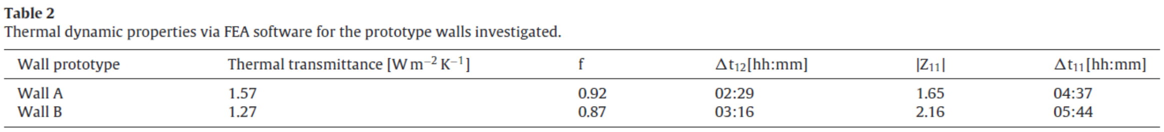

Table 2
Thermal dynamic properties via FEA software for the prototype walls investigated.

Wall prototype	Thermal transmittance [W m^{-2} K^{-1}]	f	Δt_{12}[hh:mm]	$\lvert Z_{11}\rvert$	Δt_{11}[hh:mm]
Wall A	1.57	0.92	02:29	1.65	04:37
Wall B	1.27	0.87	03:16	2.16	05:44

4. Results and discussion

In Figure 6 are shown the results obtained with the proposed experimental procedure in terms of temperature evolution in front and rear side of the two considered walls. In particular, the trend of the max value of temperature in the heating area at the centre of the wall has been considered Figure 7. It can be noticed as at least 3 cycles are necessary to reach steady-state condition and evaluate the parameters f_θ and Δt_θ. Also, it is interesting to notice as higher temperature was revealed on the front surface of the Wall B with respect to Wall A: it is clear as the presence of hemp fibres entails an increasing of f_θ and Δt_θ parameters.

Similar results were obtained by numerical simulation with Comsol® (Figure 8) although to a lesser extent. In fact, due to the thermal properties of the hemp fibres, higher temperatures were observed in the front surface of the wall and lower temperatures on the rear surface with respect to the empty wall. Moreover, as found in the experimental results, a higher phase delay of temperature signal is obtained for the Wall B.

In order to perform the calculation according to the Standard EN ISO 13786:2007, the thermal conductivity and density of hollow brick as a whole, with or without filling of hemp insulation within the hollows, was determined. Measurements resulted in λ=0.197±0.0014 $W \cdot m^{-1} \cdot K^{-1}$ and ρ=649 $kg \cdot m^{-3}$ for the empty hollow brick and λ=0.143±0.0010 $W \cdot m^{-1} \cdot K^{-1}$ and ρ=700 $kg \cdot m^{-3}$ for the brick filled with the hemp fibres. The specific heat of the brick was not measured, but we referred to data sheet of Wienerberg, from which it was c_{peb}=1000 $J \cdot kg^{-1} \cdot K^{-1}$. With regard to the thermal properties of the mortar, no measurements were carried out and we referred to values of its data sheet: λ=0.330 $W \cdot m^{-1} \cdot K^{-1}$, ρ=1400 $kg \cdot m^{-3}$ and c_{pm}=1000 $J \cdot kg^{-1} \cdot K^{-1}$. The specific heat of the hollow brick when filled with the hemp fibres (c_{pfb}) was determined by the rule of mixture as:

$$c_{pfb} = \frac{m_1}{m_1+m_2} c_{peb} + \frac{m_2}{m_1+m_2} c_{ph} \qquad (11)$$

where m_l and m_2 are the masses of the empty brick and of the hemp fibres used to fill the holes of the hollow brick, respectively. The specific heat of the hemp fibres (c_{ph}) is referred to literature data [23] and for T=20°C it is 2200 J kg^{-1} K^{-1}.

Considering that m_l=3.2 kg and m_2=0.3 kg, it was c_{pfb}= 1103 J kg^{-1} K^{-1}. Table 1 summarizes the thermal properties for all the materials involved, and starting from which the dynamic thermal properties of the walls in accordance with Standard EN ISO 13786:2007 were performed.

The calculations take into account inner and outer thermal resistances respectively set up to 0.13 and 0.04 $m^2 \cdot K \cdot W^{-1}$ and allowed to obtain the thermal transmittance U_0, and thermal dynamic transfer properties. Moreover the Standard EN ISO 13786:2007 is referred to one direction heat-flux, therefore to cases in which the heat-flux flows in x-direction and bottom and top sides of the wall, parallel to x-direction, are considered adiabatic (Figure 9). All the results are collected in Table 2.

In Table 3 a comparison among the results obtained by the three used approaches is shown. You can note that results comparable in terms of f_θ and Δt_θ parameters were obtained between experimental and numerical simulation carried out with Comsol®. In particular, in both the cases of Wall A and Wall B, the numerical simulation with Comsol® provided lower values in the decrement of temperature amplitudes and higher values in time shift between maximums of the temperature profiles. This can be explained by the consideration that the numerical simulation assumes the presence of ideal materials that are isotropic in the thermophysical characteristics and, accordingly, returns the potentially best obtainable results. On the other hand, the realistic conditions that are established during testing (possible presence of defects inside the stratigraphy, not perfect adhesion between the bricks, lack of uniformity when hemp fibres fill the holes, preferential directions of the heat flow in the stratigraphy) cause a reduction in performance of the wall, which results in an increase in temperature on the not stimulated side and a reduced delay in the thermal wave phase shift.

Moreover, it is clear that the presence of the hemp fibres determines an increasing of time shift between the temperature waves with respect to empty brick (19 minutes in the experimental test and 16 minutes in the numerical simulation) and a decreasing in the decrement factor (32% in the experimental test and 21% in the numerical simulations, defined as the difference between the decrement factors on the filled and the empty walls, with respect to the empty one), therefore improving the thermal behaviour of the wall.

On the other hand, as expected, very different values were obtained following the EN ISO 13786 Standard. The main difference between the approaches is in a different "cause and effect" relationship. In fact, the effect observed in all the approaches is the same, i.e. the change in temperature on the not stimulated side; in contrast, in the experimental measurement, as well as in the numerical simulation, the cause of the dynamic regime is the sequence of switching on and off of the halogen lamps, therefore the radiated heat-flux towards the wall. Instead, in the approach with the Standard the dynamic regime is due only to changing in temperature on a side of the wall, while no heat-flux is considered.

To this difference, a non-perfect comparability between the approaches will be added: in experimental tests we monitor a prototype wall introduced inside a uniform temperature environment, for which it cannot be excluded, without any doubt, an interdependence between the two sides of the wall, in addition to that due to the imposed stimulation; on the other hand, the standard EN ISO 13786 refers to walls which separate different environments and that, therefore, experiment different environmental conditions: in this case the only variable that correlates them, through a "cause-effect" relationship, is only the imposed solicitation.

However, an increasing of time shift between the temperature waves (67 minutes) and a decreasing in the decrement factor (23%) was observed for the Wall B with respect to the Wall A, indicating a dynamic behaviour similar to those obtained with the experimental measurement and numerical simulation in terms of improvements associated with the presence of hemp fibres.

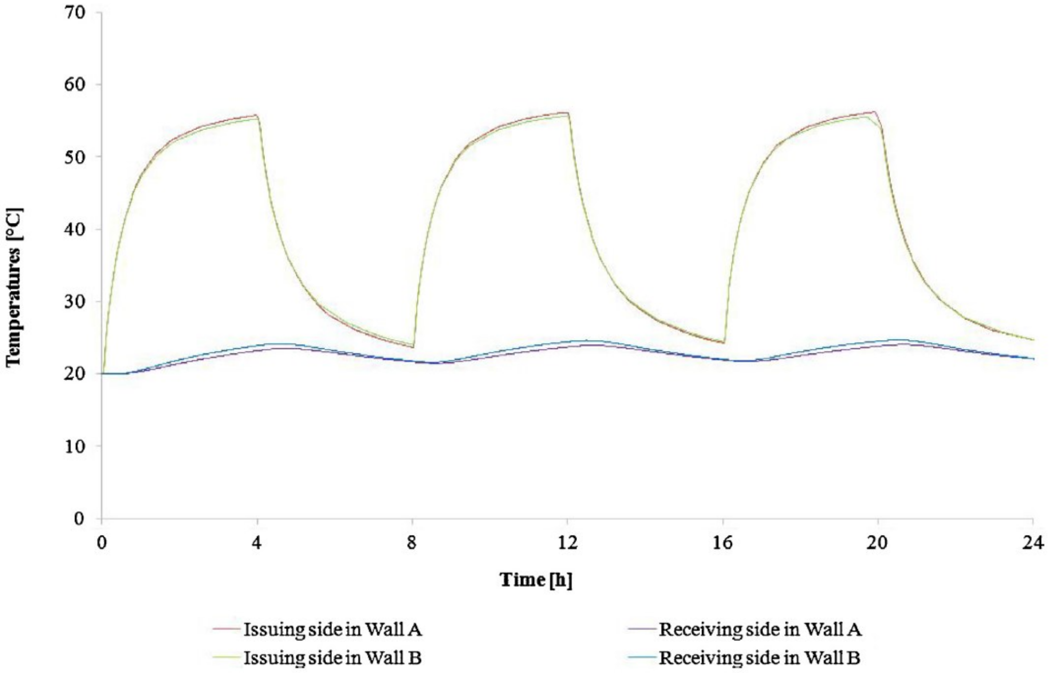

Figure 7: Numerical simulation with Comsol Multiphysics®: Comparison among temperatures for both the sides of brick

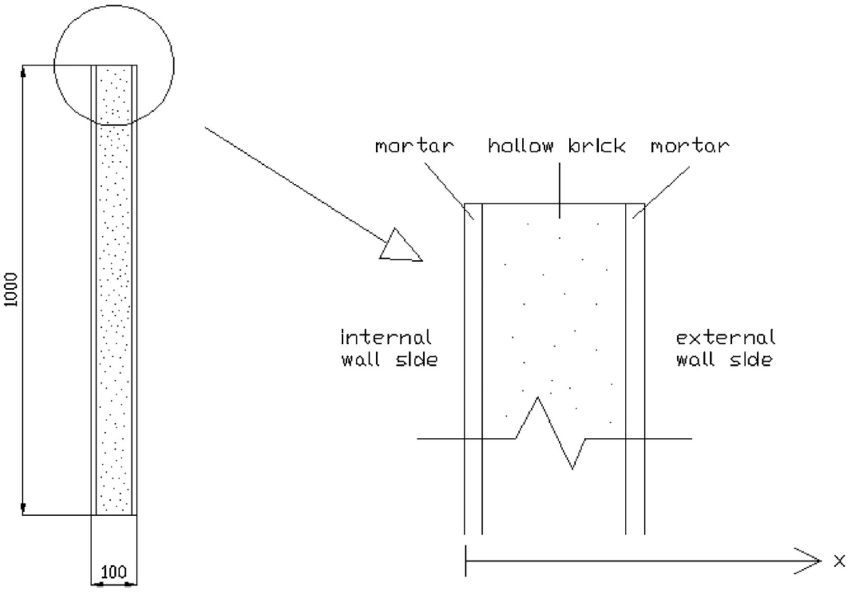

Figure 8: Schematic of the prototype wall

5. Conclusions

In this work a new experimental procedure to investigate the thermal dynamic behaviour of prototype walls has been proposed, in order to develop a procedure for studying the behaviour of materials throughout the building's life cycle. In particular, a stimulated thermographic technique has been used to heating with a periodic heat source the wall and to analyse the thermal response of the frontal and rear surface.

Two prototype walls were used for experimental tests: a wall filled with hemp fibres and an empty one. Two halogen lamps were used as heat sources controlled with an electronic system capable to generate a periodic square wave signal.

In addition, a numerical simulation with the commercial software Comsol® and calculation according to the Standard procedure EN ISO 13786:2007 were carried out in order to obtain a comparison of results in terms of decrement factor and time lag of the wall.

With regarding to comparison between experimental tests and numerical simulation, some minor differences were found, demonstrating a best result for the simulation with respect to measurements (lower decrement factor and higher time lag). This can be explained by the consideration that the numerical simulation assumes that the materials involved are uniform and with isotropic thermophysical properties: according to this, it provides the potentially best obtainable results. On the other hand, the realistic conditions that are established during the testing (possible presence of defects inside the stratigraphy, not perfect adhesion between bricks, lack of uniformity when hemp fibres fill the holes and preferential directions of the heat flow in the stratigraphy) cause a reduction in performance of the walls.

Very different results were obtained using the Standard EN ISO 13786, with respect to those obtained with experimental and numerical studies. Indeed, the decrement factors were in the orders of 0.46 and 0.60 for the former, while they were in the range 0.11 – 0.28 for the latter; even more marked is the difference between the time lags: 4 hours and 37 minutes or 5 hours and 44 minutes for the Standard and not more than 30 or 40 minutes for experimental and numerical simulation, respectively. These could be explained with different methodologies followed to stimulate a side of the wall: radiated heat-flux for experimental and numerical simulation, changing in the environment temperature for Standard. Moreover, the experimental tests were carried out on a prototype wall introduced inside a uniform temperature environment, for which it cannot be excluded, without any doubt, an interdependence between the two sides of the wall, in addition to that due to the imposed stimulation.

On the other hand, the standard EN ISO 13786 refers to walls which separate different environments and that, therefore, experiment different environmental conditions: in this case the only variable that correlates them, through a "cause-effect" relationship, is only the imposed solicitation.

However, all the results related to the three used approaches show an improving in the thermal dynamic behaviour of the wall filled with hemp fibres, with respect to the empty one. Indeed, the decrement factor reduced by about 32%, 21% and 23% for experimental, numerical simulation and according to Standard, respectively, when the wall is filled with the hemp fibres. Moreover, passing from the empty wall to filled one, the time lag increased by 19 minutes, 16 minutes and 67 minutes for experimental, numerical simulation and according to Standard, respectively.

Considering the differences in the results, the next step will be the application of the developed methodology *in situ*, on a wall which separates two different rooms and composed by homogeneous layers. This will make it possible to check whether the experimental approach, as well as numerical simulation, provides results closer to those returned from the Standard.

Acknowledgement

This work was supported by EFFEDIL Project (EFFicient Energy builDing Innovative soLutions Grant no: PON02_00323_2938699) funded by Italian Ministry of Education and Research.

The authors of the present work thank *CETMA* for the measurement of thermal conductivities of prototype walls.

References

[1] http://eur-lex.europa.eu/legal-content/EN/TXT/HTML/?uri=CELEX:32010L0031&from=IT;

[2] EN ISO 13786:2007, Thermal performance of building components – Dynamic thermal characteristics – Calculation methods, 2007.

[3] Kaska O, Yumrutas R, Arpa O. Theoretical and experimental investigation of total equivalent temperature difference (TETD) values for building walls and flat roofs in Turkey. Appl Energy 2009;86:737–747.

[4] Kontoleon KJ, Bikas DK. The effect of south wall's outdoor absorption coefficient on time lag, decrement factor and temperature variations. Energy and Buildings 2007;39:1011–1018.

[5] Al-Sanea SA, Zedan MF, Al-Hussain SN. Effect of thermal mass on performance of insulated building walls and the concept of energy savings potential. Appl Energy 2012;89:430–442.

[6] Yumrutas R, Kaska O, Yildirim E. Estimation of total equivalent temperature difference values for multilayer walls and flat roofs by using periodic solution. Building and Environment 2007;42:1878–1885.

[7] Ozel M. Effect of insulation location on dynamic heat-transfer characteristics of building external walls and optimization of insulation thickness. Energy and Building 2014;72:288–295.

[8] Asan H. Investigation of wall's optimum insulation position from maximum time lag and minimum decrement factor point of view. Energy and Buildings 2000;32 (2):197–203.

[9] Mazzeo D, Oliveti G, Arcuri N. Influence of internal and external boundary conditions on the decrement factor and time lag heat flux of building walls in steady periodic regime. Applied Energy 2016; 164: 509–531.

[10] Gagliano A, Patania F, Nocera F, Signorello C. Assessment of the dynamic thermal performance of massive buildings. Energy and Buildings 2014;72:361–370.

[11] Ulgen K, Experimental and theoretical investigation of effects of wall's thermophysical properties on time lag and decrement factor. Energy and Buildings 2002;34(3):273–278.

[12] Pernigotto G, Prada A, Patuzzi F, Baratieri M, Gasparella A, Characterization of the dynamic thermal properties of the opaque elements through experimental and numerical tests. Energy Procedia 2015; 78: 3234–3239.

[13] Martìn K, Flores I, Escudero C, Apaolaza A, Sala JM. Methodology for the calculation of response factors through experimental tests and validation with simulation. Energy Build. 2010; 42:461–467.

[14] Palumbo D, Galietti U, Damage Investigation in Composite Materials by Means of New Thermal Data Processing Procedures, Strain, 2016; 52(4):276-285.

[15] Tamborrino R, Palumbo D, Galietti U, Aversa P, Chiozzi S, Luprano VAM, Assessment of the effect of defects on mechanical properties of adhesive bonded joints by using non destructive methods. Composites Part B, 2016; 91:337-345.

[16] Palumbo D, Tamborrino R, Galietti U, Aversa P, Tatì A, Luprano VAM, Ultrasonic Analysis and lock-in thermography for debonding evaluation of composite adhesive joints. NDT & E International, 2015; 78:1-9.

[17] Maldague X, Theory and practice of infrared technology for non-destructive testing. Wiley Series in microwave and optical engineering, Kai Chang, Series Editor, 2001.

[18] Galietti U, Luprano VAM, Nenna S, Spagnolo L, Tundo A, Non-destructive defect characterization of concrete structures reinforced by means of FRP. Infrared Physics & Technology, 2007; 49:218-6.

[19] Albatici R, Tonelli A M, Infrared thermovision technique for the assessment of thermal transmittance value of opaque building elements on site. Energy and Building 2010; 42:2177–2183.

[20] Donatelli A, Aversa P, Luprano VAM, Set-up of an experimental procedure for the measurement of thermal transmittances via infrared thermography on lab-made prototype walls. Infrared Physics & Technology 2016; 79, 13 –143.

[21] ISO 8302:1991, Thermal insulation – Determination of steady-state thermal resistance and related properties – Guarded plate apparatus, 1991.

[22] EN 12664:2001, thermal performance of building materials and products. Determination of thermal resistance by means of guarded hot plate and heat flow meter methods. Dry and moist products of medium and low thermal resistance, 2001.

[23] Behzad T., Sain M., Measurement and prediction of thermal conductivity of hemp fibre reinforced composites. Polymer Engineering & Science 2007; 47:977-983.

C Coating defect evaluation based on stimulated thermography

Abstract

Thermal Barrier Coatings are used to protect the materials from severe temperature and chemical environments. In particular, these materials are used in the engineering fields where high temperatures, corrosive environments and high mechanical stress are required. Defects present between substrate material and coating, as detachments may cause the break of coating and the consequent possibility to exposure the substrate material to the environment conditions. The capability to detect the defect zones with non-destructive techniques could allow the maintenance of coated components with great advantages in terms of costs and prediction of fatigue life.

In this work, two different heat sources and two different thermographic techniques have been used to detect the adhesion defects among the base material and the coating. Moreover, an empirical thermographic method has been developed to evaluate the thickness of the thermal coating and to discriminate between an unevenness of the thickness and a defect zone.

The study has been conducted on circular steel specimens with simulated adhesion defect and on specimens prepared with different thicknesses of thermal barrier coating.

Keywords: Pulsed and stepped thermography, Thermal Barrier Coatings, Adhesion defects, Thicknesses, Cooling Analysis

1. Introduction

Thin layers of thermal barrier coatings (TBC) are applied to metallic components of heat engines to reduce their operating temperatures, increase environmental protection and extend the life of components. An engine with TBC-coated components will have a service life significantly longer than an engine with uncoated components. Currently of special interest is the use of TBC in aircraft engines.

TBC systems consist of a high-temperature oxidation/corrosion resistant metallic bondcoat (usually MCrAlY M = Ni, Co) and a ceramic topcoat which is typically yttria stabilized zirconia (YSZ), deposited either by air plasma spray or electron beam-physical vapor deposition on the bondcoat (BC) [1]. The role of the ceramic topcoat is to further decrease the temperature of the underlying substrate, while the bondcoat provides high temperature oxidation resistance as well as good adhesion between the bondcoat and the ceramic topcoat. The refractory ceramic porous layer can reduce the temperature of the base metal by 30-100°C, depending on the thickness and on specific microstructural properties of the coating.

In order to ensure the safety and reliability of the coating work, it is necessary to use nondestructive testing method to characterize and evaluate the state of TBC in both manufacturing and service. Failure of a TBC could lead to a costly unplanned outage and could lead to catastrophic events. It is therefore necessary to monitor the condition of the TBC so as to avoid such failures and, if possible, to provide pre-cursor information that would suggest whether spallation is imminent. Due to the porous nature of TBC, conventional nondestructive testing methods, such as ultrasonic [2] and X ray [3] method, are difficult to be competent.

Infrared thermal nondestructive testing method can be used for the testing of TBC [4, 5, 6], it leads to nondestructive techniques to assess the adhesion of coatings such as thermal barrier coatings (TBC). As a matter of fact, this technique is used today as a quality control technique, especially during the development of the deposition procedure for complex-shaped components or for in-field coating inspection of serviced components [7, 8]. Thermography is a rapid and effective mean to control the adhesion state of the coatings. The most efficient thermal tests are the dynamical or active ones, which can detect the presence of sub-surface detachments by monitoring the evolution of the coating temperature during a thermal transient. Marinetti et al. even proposed the thermographic inspection method to discriminate reliably between TBC thickness changes coated gas turbine blades and adhesion defects [5].

In this work, the new thermal data processing procedures developed to investigate damages in composite materials has been applied to evaluate adhesion defects of coatings. The presence of a defect can be revealed by monitoring the surface temperature decay of the specimen. In fact, the defect appears as an area of different temperature with respect to a surrounding sound area, and it produces an abnormal behavior of the temperature decay curve [9].

Moreover, an empirical thermographic method has been developed to evaluate the thickness of the thermal coating and to discriminate between an unevenness of the thickness and a defect zone.

The thermographic technique used to achieve the outcomes is the both pulsed and stepped thermography, the stimulation is obtained by flash lamps a by laser source respectively. Circular steel specimens coated with TBC, in which different drilled holes have been realized to simulate adhesion defects, have been used to identify the defects. While, using specimens with different thicknesses of TBC, the procedure able to discriminate between thickness variations and defects has been developed and a prediction model for the thickness of the coating has been proposed.

2. Materials And Methods

2.1 Specimens

The specimens used are ten discs with metallic bondcoat and a ceramic topcoat which is yttria stabilized zirconia (YSZ), deposited by High Velocity Oxy Fuel (HVOF) technique. Two of these have been realized, keeping the same thickness, with an adhesion defect. The method used for the realization of the specimens with detachment of TBC involves the following implementation phases: drilling of the basis metal specimens, insertion of a copper pin, molding and sandblasting of the surface, application of the bondcoat and topcoat, the pin removal, insertion of base material plugs (Figure 1b).

The remaining eight specimens have been realized coating the basic metallic material with different thicknesses (L) of TBC, without inserting any defect. Figure 1a shows the final appearance of the samples.

In table 1, the thickness of TBC coating and the dimension of the detachment for the defected specimens are reported, in table 2, the thicknesses of TBC coating for the specimens without defects are reported.

1a

1b

Figure 1: 1a. Picture of one of the reference-coated samples; 1b. Picture of a sample during the phase for producing the adhesion defect

Table 1: Thickness of TBC coating and dimension of the detachment for the defected specimens

Specimen	Thickness of TBC (mm)	Diameter of defect (mm)
1	0,35	2
2	0,35	5

Table 2: Thicknesses of TBC coating for sound specimens

Specimen	Thickness of TBC (mm)
$\mathbf{L_1}$	0,1
$\mathbf{L_2}$	0,2
$\mathbf{L_3}$	0,3
$\mathbf{L_4}$	0,4
$\mathbf{L_5}$	0,6
$\mathbf{L_6}$	0,7
$\mathbf{L_7}$	0,87
$\mathbf{L_8}$	0,95

2.2 Thermographic data acquisition

2.2.1 Defect investigation

A flash source (flash lamps 1500J x 2) generating a pulse of 5ms has been used for implementing the pulsed thermography and a 1064 nm wavelength Ytterbium pulsed fiber laser generating pulse of 500ms for implementing the stepped thermography. The energy and the diameter of the heating shots were fixed equal to 30W and 25mm, respectively. A cooled IR camera with an indium-antimonium detector and resolution of 640-512 pixel (Flir X6540 SC) sensitive in the range of 3-5 μm was used to monitor the temperature transient of the sample surface at frame rates of 300 Hz. The experimental set up is shown in figure 2.

Two different acquisitions for each specimen and for each source have been made.

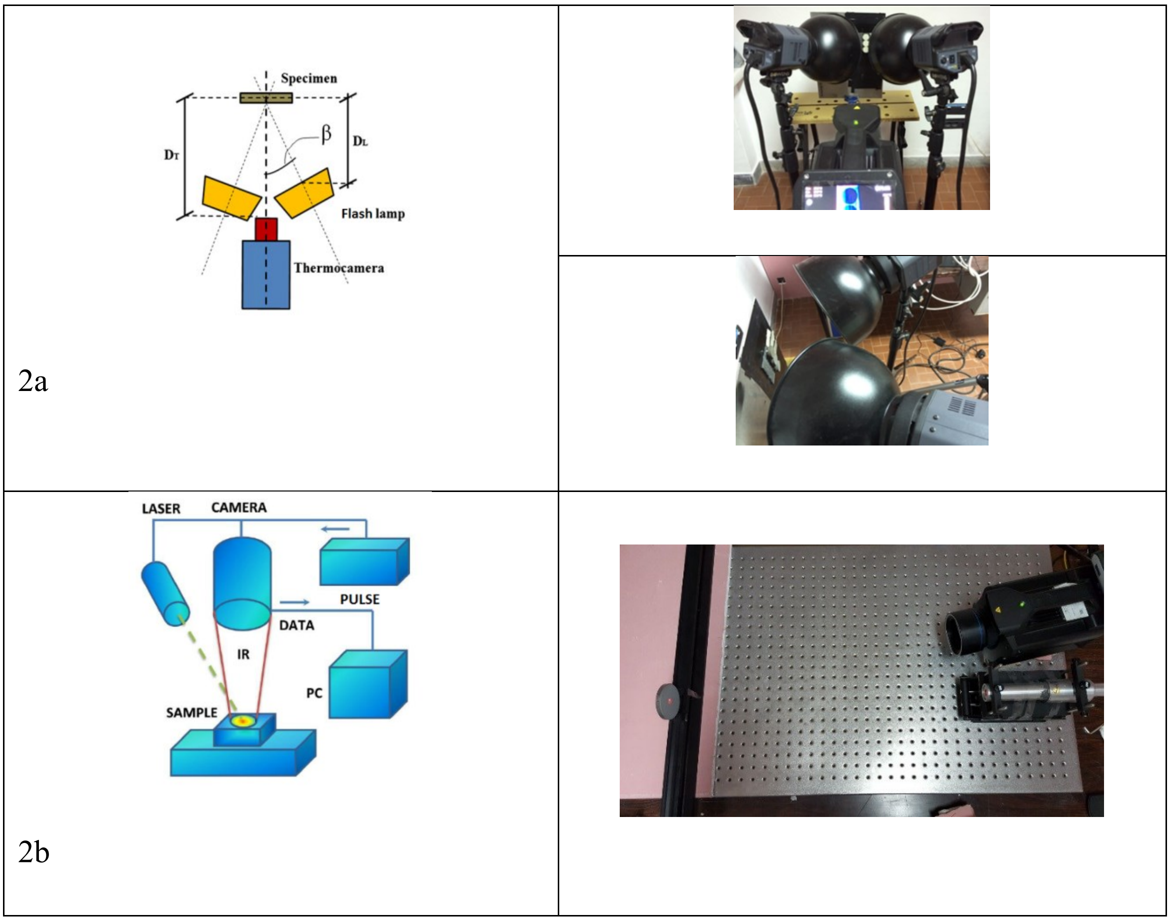

2a

2b

Figure 2: Experimental set up for thermographic data acquisition. 2a. Set up referred to flash heating source; 2b. Set up referred to laser heating source [10]

2.2.2 Thickness assessment

In order to evaluate the thickness only the stepped thermography has been implemented. A 1064 nm wavelength Ytterbium pulsed fiber laser generating pulses of 100ms, 200ms, 500ms was used as a heating source. The energy and the diameter of the heating shots were fixed equal to 7.5W and 8 mm, respectively.

A cooled IR camera with an indium-antimonium detector and resolution of 640-512 pixel (Flir X6540 SC) sensitive in the range of 3-5 μm was used to monitor the temperature transient of the sample surface at frame rates of 150 Hz. The experimental set up is shown in figure 2.

Twenty-four different points with an excitation pulse of 100ms, 200ms and 500ms have been investigated for each of the eight specimens.

3. Results And Discussion

3.1 Theoretical remarks

The proposed approach for achieving the outcomes is based on the following equations:

$$T(L,t) = \frac{W}{e_c\sqrt{\pi t}}\left(1 + 2\sum_{n=1}^{\infty}(-\Gamma)^n e^{-\frac{n^2L^2}{\alpha_c t}}\right) \tag{1}$$

where L is the coating thickness (m), t the time (s), e_c the coating effusivity (W $s^{1/2}$ m^{-2} K^{-1}), W the absorbed energy density (J m^{-2}), C the reflection coefficient and α_c the coating diffusivity (m^2 s^{-1}). $T(L,t)$ is the surface temperature of a coating layer of thickness L deposited on to a semi-infinite body, heated by a Dirac pulse and not subjected to heat exchange with the environment [11].

The main idea, in common with all other non-destructive inspection techniques, is that a defect inducing different thermophysical local properties in the material will also induce an anomaly in the thermal diffusion and subsequently a different surface temperature in the component. In fact, these techniques look for areas of differing thermal behavior that can be correlated to a defect and that are typically dependent on different thermal–physical properties involved in the heat transmission phenomena such as the thermal conductivity, the specific heat at constant pressure and the density of material [12, 13].

3.2 Data processing and results

3.2.1 Defect investigation

The presence of the defect determines a modification of thermal profile during cooling stage with a typical non-linear behavior. It can be seen in figures 3a and 3b the temperature profiles (cooling stages) for the thermographic sequences of the defective samples acquired with an excitation pulse of 5ms using a flash source and with an excitation pulse of 500ms using a laser source, respectively. In particular, the sound areas show a different behavior of the temperature decay curve respect to the defective areas, the cooling curves of the defective areas are more linear. Thermal data have been processed by IRTA® (DES srl, Bari, Italy) software in order to obtain slope and R-Square images, which describe objectively the trend of the cooling curve.

The R-Square value used in the paper is defined as R-Square = 1- (SSres/SStot), where SSres is the residual sum of squares and SStot is the total sum of squares. In the case of a simple linear regression, R-Square equals the square of the Pearson correlation coefficient between the observed and predicted data values of the dependent variable [14].

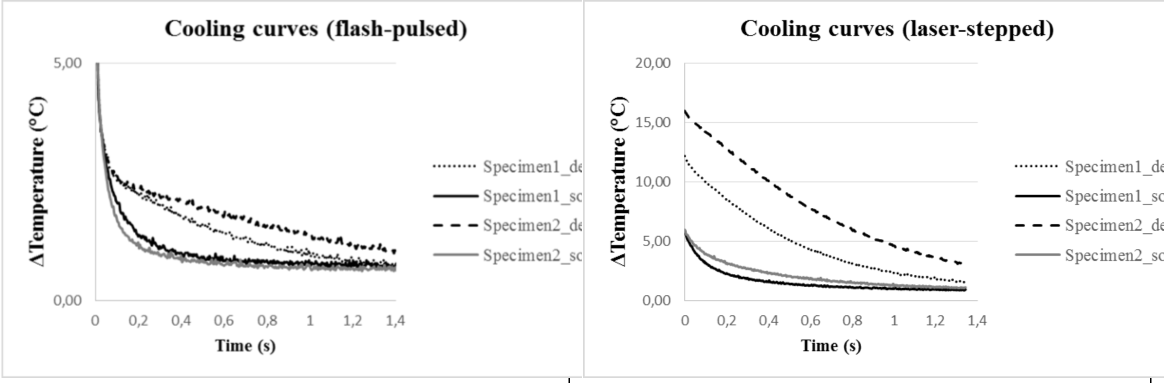

3a **3b**

Figure 3: 3a.Temperature profile for the thermographic sequences of the defective sample acquired with an excitation pulse of 5ms using a flash source and 3b. with an excitation pulse of 500ms using a laser source. The sound areas show a different behavior of the temperature decay curve respect to the defective areas. The cooling curves of the defective areas are more linear.

Table 3: Quantitative analysis results

Flash-pulsed

Nominal diameter of the defect (mm)	Nominal area of the defect (mm^2)	Algorithm	α	DA (mm^2)	E (%)
2	3,14	Slope	0,98	3,09	1,59
2	3,14	R-Square	0,95	3,19	1,59
5	19,63	Slope	0,93	19,60	0,13
5	19,63	R-Square	0,86	19,26	1,86

Laser-stepped					
Nominal diameter of the defect (mm)	Nominal area of the defect (mm^2)	Algorithm	α	DA (mm^2)	E (%)
2	3,14	Slope	0,99	3,73	18,79
2	3,14	R-Square	0,96	3,54	12,74
5	19,63	Slope	0,42	19,49	0,69
5	19,63	R-Square	0,87	19,16	2,37

Figure 4 shows the maps of slope and R-Square, that are the values of the slope and R-Square of the temperature profile (cooling stage) for each pixel, obtained by thermographic data coming from flash-pulsed investigation as described in Material and Methods, using IRTA®, for the two defected sample (diameter of defects 2mm and 5mm). As expected, in the defect zones high R-Square values are indicator of the linearity of the cooling stage curves, while the slope presents lower values than the sound material.

Figure 5 shows the results obtained for the same samples by processing thermographic data coming from laser-stepped investigation.

The figures contains also the binarized imagines obtained in order to carrying out the quantitative evaluation of the defects applying the following criterion.

The detectable and undetectable area of defects are expressed as 1 and 0 (hit/miss data), respectively. Threshold value *Th* has been defined through a statistical analysis of data considering the following equation:

$$Th = \alpha[mean(A_d) - mean(A_s)] + mean(A_s) \tag{2}$$

where the parameter α has values between 0.3 and 1 with step 0.01 and A_d and A_s, indicated in figure 4, are those with continuous line and dotted line, respectively. The application of eq. (2) to all maps of R-Square and slope for both techniques, allows for obtaining binary images. The defected area (DA) has been obtained by counting the binary pixels with value equals to one. The percentage error E (%) has been obtained following the equation below:

$$\mathrm{E}\ (\%) = \frac{DA-NA}{NA} * 100 \tag{3}$$

where NA is the nominal area of the defect. The α value reported in table 3 has been obtained in correspondence of the minimum value of the E(%). The error obtained by this procedure indicates that the flash-pulsed technique is better than the laser-stepped technique for evaluating the defected dimension. It seems that this kind of thermographic data analysis, not based on thermal contrast but on the slope and R-Square, is able to identify clearly the defect.

Slope (Diameter of defect 2mm)	Slope (Diameter of defect 5mm)
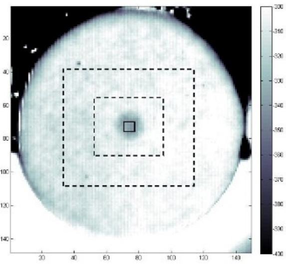	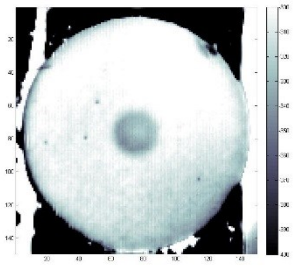
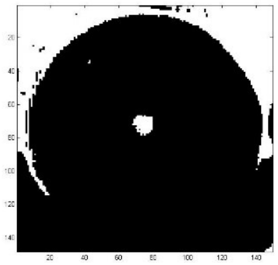	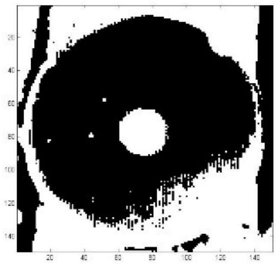
R- Square (Diameter of defect 2mm)	R- Square (Diameter of defect 5mm)
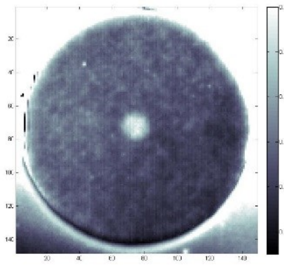	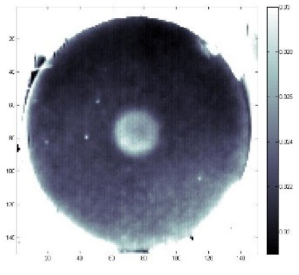
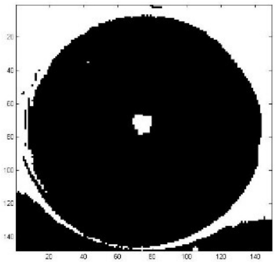	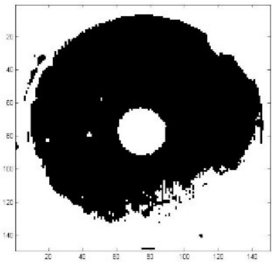

Figure 4: Maps of slope and R-Square obtained by thermographic data coming from flash-pulsed investigation for the two defected sample (diameter of defects 2mm and 5mm).

Slope (Diameter of defect 2mm)	Slope (Diameter of defect 5mm)
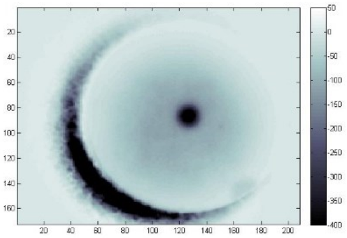	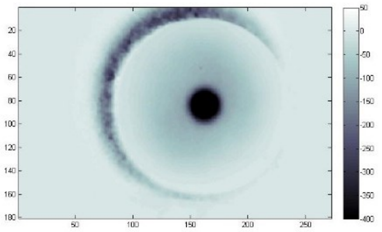
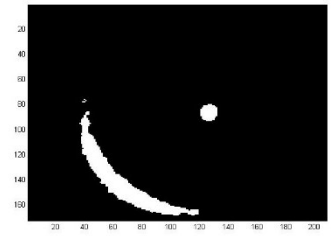	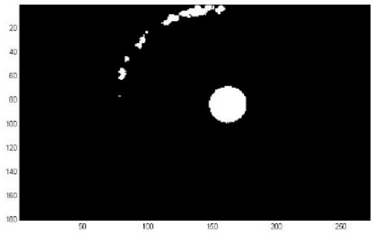
R-Square (Diameter of defect 2mm)	R-Square (Diameter of defect 5mm)
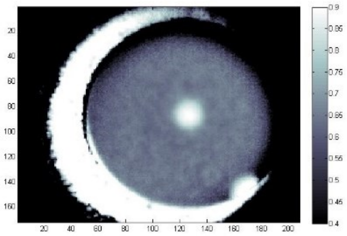	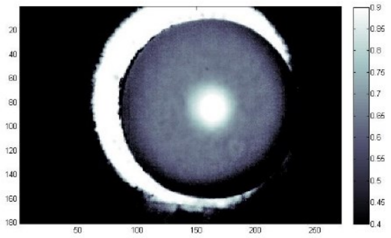
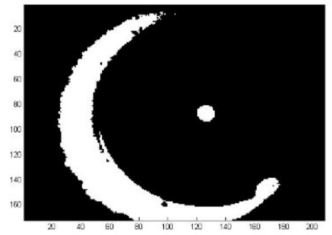	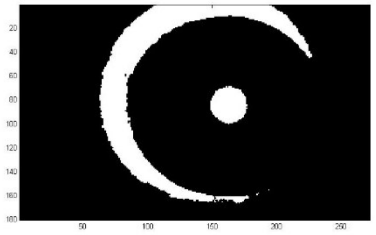

Figure 5: Maps of slope and R-Square obtained by thermographic data coming from laser-stepped investigation for the two defected sample (diameter of defects 2mm and 5mm).

3.2.2 Thickness assessment

According to eq (1) the surface temperature of the eight homogeneous specimens with different thickness has been plotted versus time. The temperature profile for the thermographic sequences acquired with an excitation pulse of 500ms, starting from the maximum temperature reached and considering only the cooling behavior in the same time interval, have been plotted. The plots have been obtained choosing the pixel with the maximum temperature. In Figure 6 and in figure 3b, the described profile are represented respectively for the homogeneous sample for each thickness of TBC coating and for the defective ones. The thermal data processed coming from the defective samples have been those acquired using laser-stepped thermography (Figure 3b).

Plotting linearly the surface temperatures, measured in the same time interval, versus time, it can be noted that the thickness variation results in different curves each of one characterized by a change of the cooling rate of the material (Figure 6).

It is noteworthy that the same remarks are valid for the data acquired with the other pulse durations (100ms, 200ms), for brevity only the results related to 500ms are reported.

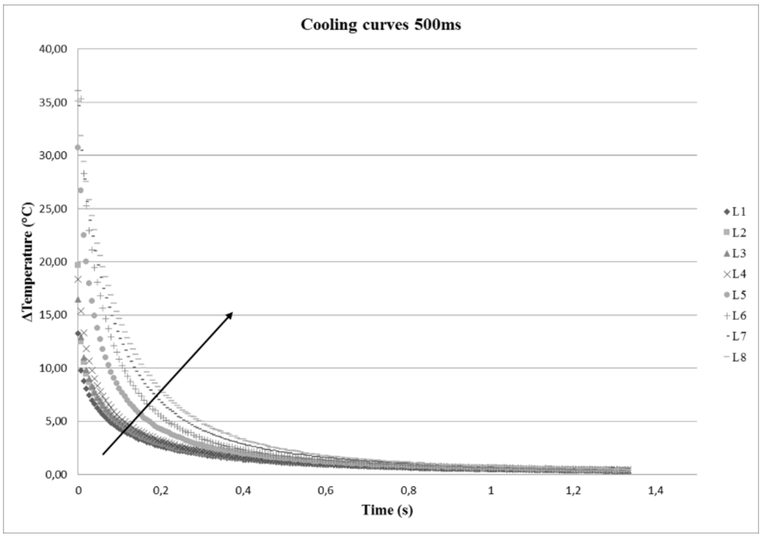

Figure 6: Temperature profile for the thermographic sequences of the homogeneous sample acquired with an excitation pulse of 500ms

Each thermographic sequences has been processed using the software IRTA® in order to evaluate the slope and the R-square value of each temperature profile, in the chosen time interval, for every pixel. The same processing have been applied to all the specimens (sound and defective).

The maps of these two parameters have been obtained. Figure 7 shows the map of the slope. The trend of the slope along the drawn fixed line is also shown.

Figure 8 shows the map of the R-Square.The trend of the R-Square along the drawn fixed line is also shown. The maps and the trends refer to one of the eight sound samples.

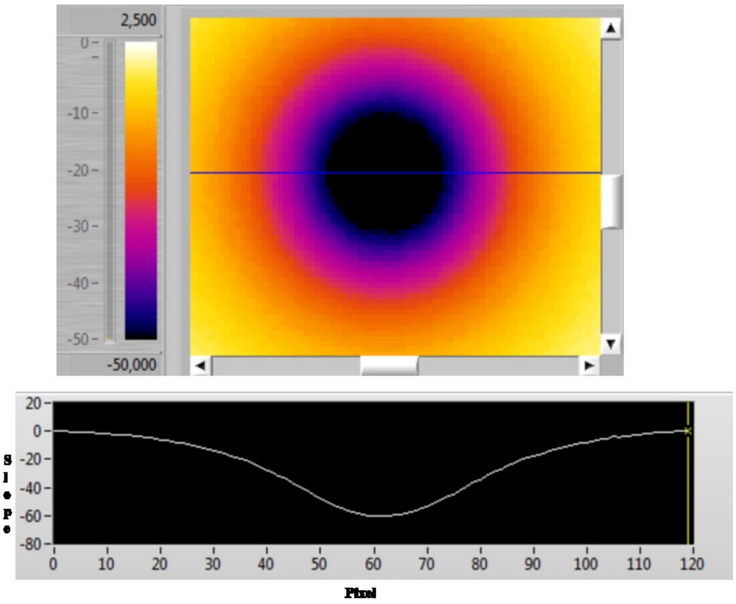

Figure 7: Map of the slope, that is the value of the slope of the temperature profile (cooling stage) for each pixel (top). Trend of the slope along the drawn fixed line on the map (bottom). The map refers to one of the eight sound sample

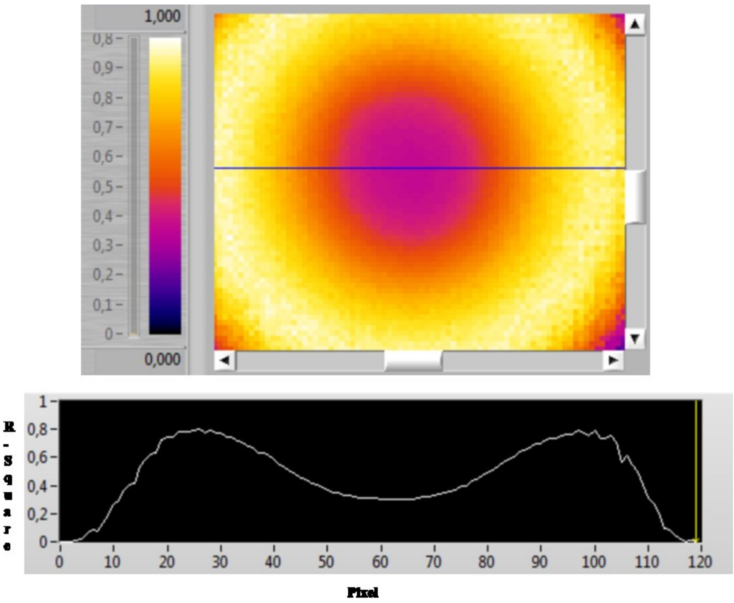

Figure 8: Map of the R-Square, that is the value of R-Square of the temperature profile (cooling stage) for each pixel (top). Trend of the R-Square along the drawn fixed line on the map (bottom). The map refers to one of the eight sound sample

The trend of the slope and of the R-Square along the same fixed line for all the eight thicknesses have been plotted (Figure 9,10).

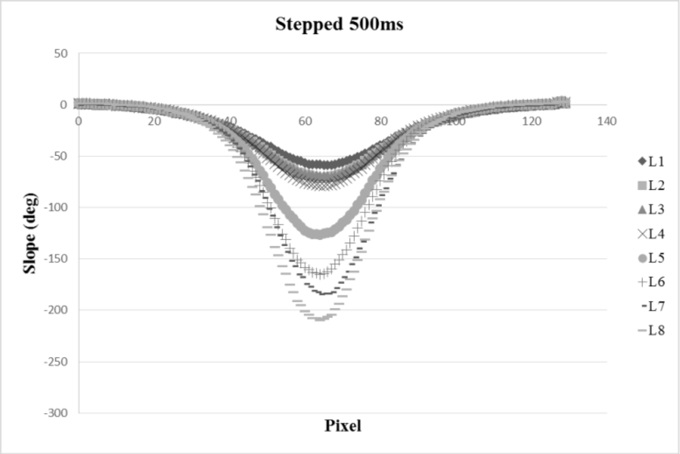

Figure 9: Trend of the slope along the same fixed line for all the eight thicknesses

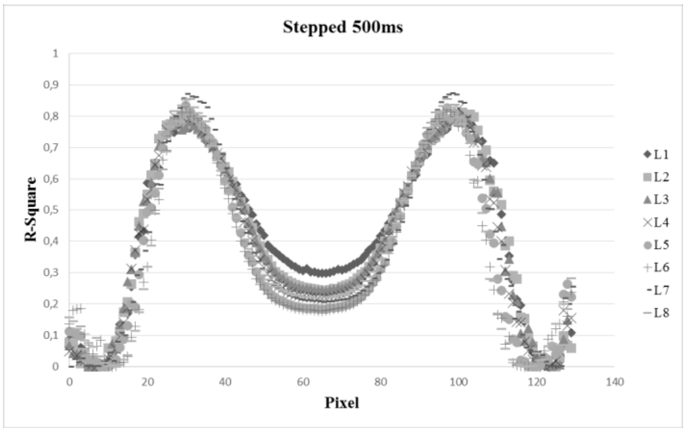

Figure 10: Trend of the R-Square along the same fixed line for all the eight thicknesses

Figure 11 shows the map of the slope for the two specimens with defects and the trend along a line drawn in a defect zone and in a sound zone.

Figure 12 shows the map of the R-Square for the two specimens with defects and trend of the R-Square along the drawn fixed line which involves both sound and defect zone.

As deduced above, the presence of the defect determines a modification of thermal profile during cooling with a typical non-linear behavior, that is the presence of an adhesion defect causes a variation of cooling rate (Figure 3) which can be wrongly interpreted as a variation in thickness. But the way in which the temperature decreases in the defective zone results more linearly with respect to that of the sound material. This is confirmed by the evaluation of the parameter R-Square in the sound zone and those in the defective one. In fact, in the defect zone the R-Square values show a high linearity of the cooling stage curves (high values of R-Square) (Figure 3), while the low R-Square is an indication of the linearity of the cooling stage curves in the sound zone (Figure 10).

Such a trend to linearity could be assumed as the discriminating parameter that allows to distinguish adhesion anomalies from coating variations of the thickness avoiding false alarms.

This simple procedure results independent on the heating pulse duration, since the same results have been obtained by processing the data coming from different exciting period. So, if also all the other parameters remain untouched during thermographic data acquisition, it can be very useful in practise.

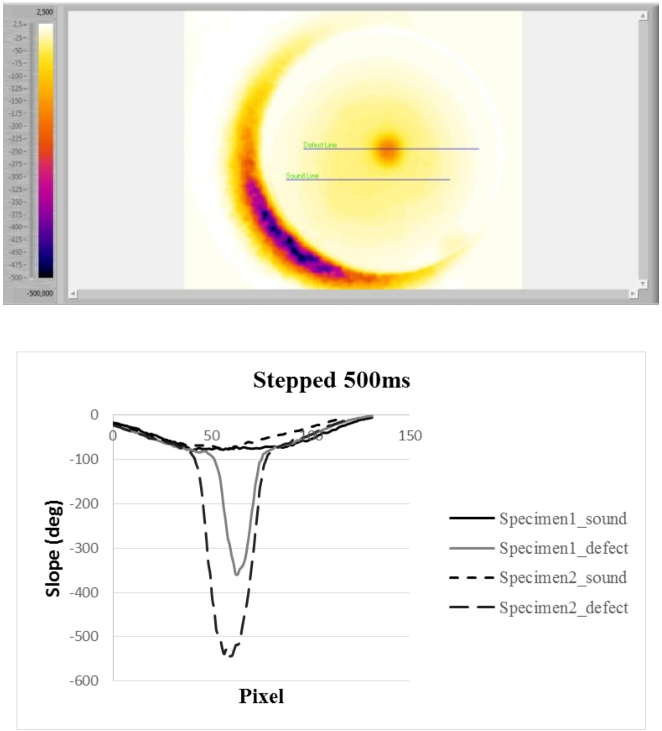

Figure 11: Map of the slope of the temperature profile (cooling stage) for each pixel of one of the two defective sample (top). Trend of the slope along the drawn fixed lines on the map (bottom). The trends refer to both the defective sample (1,2).

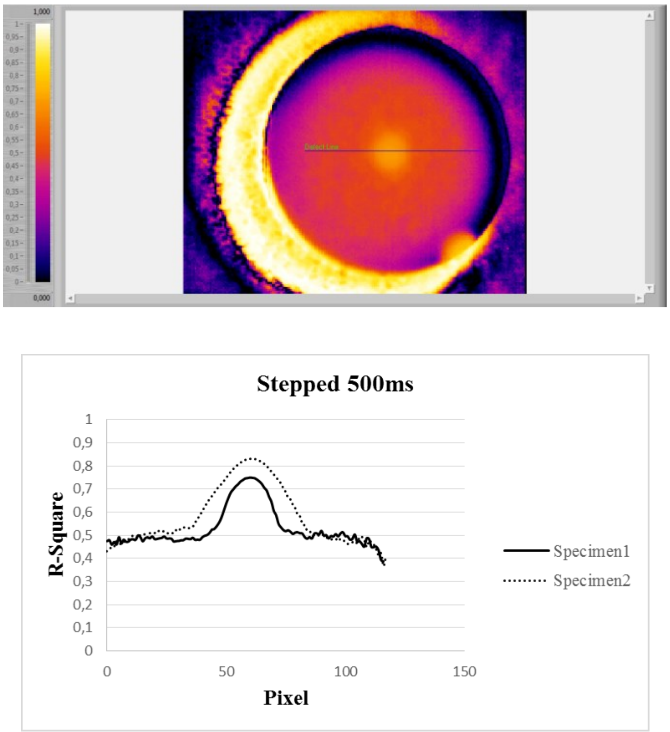

Figure 12: Map of the R-Square of the temperature profile (cooling stage) for each pixel of one of the two defective sample (top). Trend of the R-Square along the drawn fixed line on the map (bottom). The trends refer to both the defective sample (1,2).

3.2 Models

It can be noted (Figure 9) that the minimum of the slope values depends on the thickness of the coating, in particular, the minimum of the slope values decreases with the increasing of thickness.

An attempt to create possible mathematical models to describe the behaviour of coating thickness depending on the slope values of the temperature cooling profiles has been made.

The models have been obtained by considering the TBC thickness as a function of the slope values. In order to extrapolate the models, sixteen values of those related to the homogeneous specimens have been used as training data set, while the remaining eight values have been used as validation data set. Two different models seem to explain the behaviour observed: a linear model and a second order polynomial model (Figure 13).

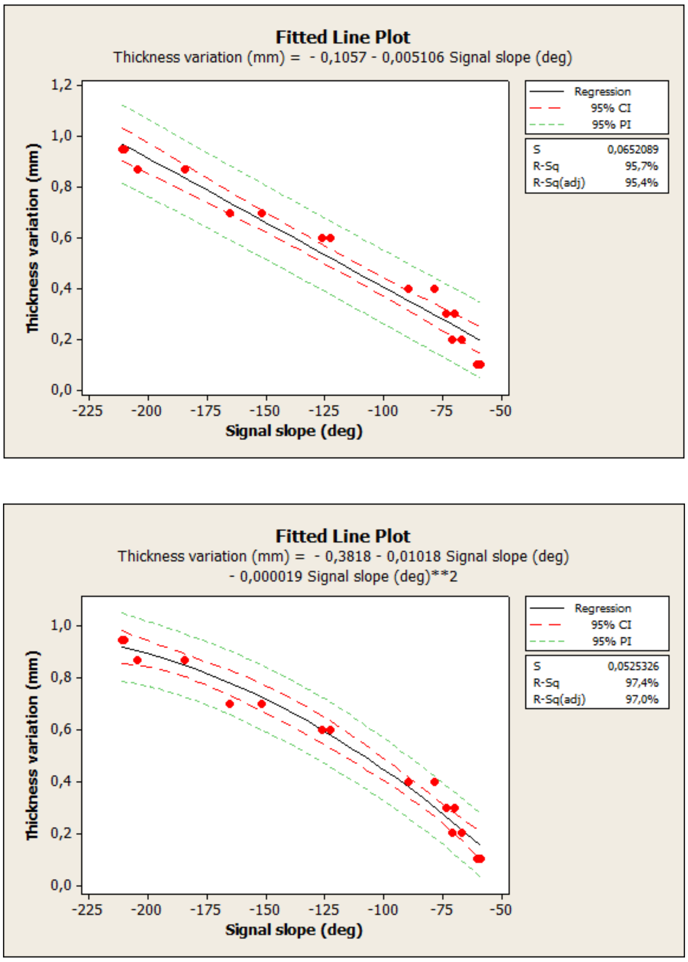

Figure 13: The linear model and the second order polynomial model of the TBC thickness as a function of the slope values.

The result of fitting is good for both models, however the error committed, in the evaluation of thickness, by choosing the linear model is greater than the error made with the polynomial model, especially for small thickness values. The errors have been calculated using the validation data set and compared with those expected by the models [14]. The errors are reported in table 4.

A further validation of the resulting models has been obtained by the evaluation of the TBC thickness for the defected samples. The models indicates a value of about 0.3mm, very close to the nominal value of 0.35mm, of thickness for both specimens corresponding to measured values of the slope of about -70 degrees (Table 5).

Table 4: Comparison between the predicted values of the thicknes by the models and the nominal values

Nominal Thickness of TBC (mm)	**Linear model expectation**	**Error**	**Polynomial model expectation**	**Error**
0.10	0.18	-0.81	0.15	-0.49
0.20	0.31	-0.54	0.24	-0.22
0.30	0.33	-0.11	0.26	0.13
0.40	0.43	-0.07	0.33	0.17
0.60	0.80	-0.34	0.58	0,03
0,70	1.05	-0.50	0.73	-0.05
0.87	1.59	-0.83	1.02	-0.18
0.95	1.65	-0.73	1.05	-0.10

Table 5: Validation of the resulting models

	Specimen 1	Specimen 2
Slope (deg)	-74.88	-70.90
TBC predicted thickness (mm)	0.30	0.27
TBC nominal thickness (mm)	0.35	0.35

4. Conclusion

In this work, a new thermal data processing procedure has been proposed for analysing thermal data based on the analysis of surface temperature dacay. In particular, two parameters, the slope and the R-Square of the cooling curve, were taken into account to characterise the defect behaviour onTBC, to assess the thickness of the coating and to discriminate between thickness variations and adhesion defects. Different tests have been carried out on samples coating with TBC layers with imposed defects and with different thicknesses. Two different heating source and two thermographic techniques, pulsed and stepped different for the heating pulse duration, has been implemented to identify the defects. The stepped thermography has been used to evaluate the thickness of the coating and to obtain a prediction model and to propose a method for the discriminating between signals originated by coating thickness variations and adhesion defects.

Both the thermographic techniques seem able to identify, using the same thermographic sequences processing and evaluating the slope and R-Square of the cooling curves, the adhesion defects in TBC with the addition that the cooling analysis can be performed in a very short time and can provide information about the dimension of defects.

As regard as the simple procedure adopted to evaluate the thickness of the coating, it results independent on the heating pulse duration, the same results, in fact, have been obtained by processing the data coming from different exciting period. So, if all the other parameters remain untouched during thermographic data acquisition, it can be very useful in practise.

The models developed to predict the effective thickness of the layers of TBC fit very well the dependence of the slope of the cooling curves by the thicknesses.
Furthermore, the same parameters can be used for predicting the coating thickness with the assurance that it is not a defect because they are able to recognize it.

Aknowledgments

This work is part of a large-scale research project (PON-SMATI) aimed at identifying innovative steels for turbo machinery used in extreme environmental conditions. The authors would like to thank GE oil & gas (Nuovo Pignone S.r.l.) for the support and collaboration provided in the experimental tests.

Bibliography

[1] Swaminathan V.P., Cheruvu N.S., “Advanced Materials and Coatings for Combustion Turbines,” V.P. Swaminathan and N.S. Cheruvu, Ed., ASM International, Materials Park (OH), 1994.

[2] Chen H.L.R., Zhang B., Alvin M.A., et al., “Ultrasonic Detection of Delamination and Material Characterization of Thermal Barrier Coatings,” J. Therm. Spray Technol. 21(6) 1184-1194 (2012).

[3] Buschinelli M., Huang X., Chen W., et al., “TGO Evolution and Coating Property Changes for EB-PVD TBC Coatings Under Cyclic Oxidation Condition,” ASME Turbo Expo 2010, Power for Land, Sea, and Air American Society of Mechanical Engineers, 2010.

[4] Tang Q., Liu J., Dai J., Yu Z., “Theoretical and experimental study on thermal barrier coating (TBC) uneven thickness detection using pulsed infrared thermography technology”, Applied Thermal Engineering, 114(5) 770-775 (2017).

[5] Marinetti S., Robba D., Cernuschi F., Bison P.G., Grinzato E., “Thermographic inspection of TBC coated gas turbine blades: Discrimination between coating over-thicknesses and adhesion defects,” Infrared Physics & Technology, 49 (3) 281-285 (2007).

[6] Tang Q., Dai J., Bu C., Qi L., Li D., “Experimental study on debonding defects detection in thermal barrier coating structure using infrared lock-in thermographic technique,” Applied Thermal Engineering, 107(25) 463-468 (2016).

[7] Vavilov V., Bison P., Grinzato E., Marinetti S., Cernuschi F., “Quantitative infrared thermographic nondestructive testing of thermal barrier coatings,” Mater. Eval., 61(6) 773-780 (2003).

[8] Rinaldi C., De Maria L., Antonelli G., Cernuschi F., “An Integrated Approach With Innovative NDTS for Thermal Barrier Coating Assessment: Optical and Frequency Scanning Eddy Current Testing (F-SECT) Combination With Pulsed Thermography,” Proc. ESDA 95555, 903-911 (2006).

[9] Palumbo D., Galietti U., “Damage Investigation in Composite Materials by Means of New Thermal Data Processing Procedures,” Strain 52 276-285(2016).

[10] Strzałkowski K., Streza M., Pawlak M.,” Lock-in thermography versus PPE calorimetry for accurate measurements of thermophysical properties of solid samples:A comparative study,” Measurement, 64 64–70 (2015).

[11] Maldague X., [Nondestructive Testing Handbook, Infrared and Thermal Testing], ASNT, Columbus (USA), vol. 3, 62 (2001).

[12] Palumbo D., Ancona F., and Galietti U., “Quantitative damage evaluation of composite materials with microwave thermographic technique: feasibility and new data analysis.” Mech. Mater. 50, 443-460 (2015).

[13] Palumbo D., Tamborrino R., Galietti U., Aversa P., Tati A., Luprano V. A. M., Ultrasonic analysis and lock-in thermography for debonding evaluation of composite adhesive joints,” NDT&E Int. 78 1-9 (2015).

[14] Montgomery D. C., and Runger G. C., [Applied Statistics and Probability for Engineers], John Wiley & Sons, Inc USA, 318-323 (2003).

D A thermographic procedure for the measurement of the tungsten carbide coating thickness

Abstract

Mechanical components subjected to severe environments are usually coat with cermet based WC–Co–Cr thermally sprayed coating. The coating plays a very important role in improving a component's survivability and operational performance. The coatings thickness is not only a parameter of the geometrical property of the coatings itself, but also an important indicator for evaluating the coatings' quality, performance and service life. The coating thickness needs to be controlled and mastered because it has a great influence on the final product performance. Non-destructive measuring techniques are indicated for coating thickness evaluation.

In this paper, a thermographic procedure based on the "long pulse" thermographic approach for the measurement of the tungsten carbide coating thickness has been proposed and a comparison has been made with the performance of the traditional flash excitation technique. A calibration has been performed to evaluate the thickness of the coating and a prediction model has been proposed.

Keywords: Coating thickness, thermographic procedure, non-destructive inspection, high-velocity oxy fuel (HVOF)

1. Introduction

Mechanical components are subjected to severe abrasive wear in a number of industrial fields, such as shipping, metallurgy, energy, and construction industry, and it is one of the most serious issues for equipment failure. Because wear only occurs on the surface of components, surface engineering techniques have become the most effective solutions for the wear problems [1-3].

Cermet based WC–Co–Cr thermally sprayed coating is considered to be potential wear resistant coating material since can offer a combination of high hardness and excellent toughness. The hard WC particles in the coatings lead to high coating hardness and high wear resistance, while the metal binder Co–Cr supplies the necessary coating toughness [4].

The tungsten carbide cermet powder can be sprayed using different spray processes such as conventional flame spraying, plasma spraying and High velocity oxy-fuel (HVOF) spraying process. The coating properties are influenced not only by the properties of the used powders but also significantly by the used spray process and spray parameters [5]. HVOF spraying, in which oxygen and fuel are combusted to accelerate feed stock powder towards the substrate building up the coating, the temperatures are moderate and the gas velocities are high, is the most common process for producing high quality carbide cermet coatings. HVOF flame spraying has been an industrially established process since the mid 1980s [6].

HVOF-sprayed WC-based cermet (e.g. WC–Co, WC–CoCr) have been shown to possess excellent tribological properties; indeed, they combine very high hardness with satisfactory toughness, as Co-based metal matrixes possesses ductility and excellent wettability toward the carbide grains [7-9].

One very important aspect, which has not been explicitly considered yet in literature, is the effect of the coating thickness on its properties, in particular on the tribological performance: this issue is particularly critical when dealing with soft substrates, as Al alloys are. Generally speaking, if a coating is very thin, a significant share of the stress distribution produced by the contact with a rigid counter body has to be borne by the substrate [10,11]: in these conditions, light alloys could deform plastically due to their high ductility. If the coating is much harder and less ductile, premature failure of the coating itself or of the coating–substrate interface becomes possible. On the other hand, however, the production of a thinner coating is clearly more economical: as the torch has to perform fewer scans in front of the substrate, the processing time is decreased, and lower amounts of gas and powder are consumed. The best compromise should therefore be sought for. Anyway, the coating plays a very important role in improving a component's survivability and operational performance. The coatings thickness is not only a parameter of the geometrical property of the coatings itself, but also an important indicator for evaluating the coatings' quality, performance and service life. Therefore, effective non-destructive testing of the coatings thickness is of great significance for the performance of the components.

The coating thickness needs to be controlled and mastered because it has a great influence on the final product performance (weight, friction, corrosion, aspect, etc.). Commercially available thickness meters, including cross-section microscopy or gravimetric (mass) measurement [12], might be destructive by inducing surface damage and are limited in spatial sampling resolution. These methods are used when non-destructive methods are not possible, or as a way of confirming non-destructive results [13].

Non-destructive measuring techniques are also used for coating thickness evaluation. Magnetic gauges [14, 15] are based on magnetic flux measurement through the layer of sample. The inadequacy of this method is the determination of thickness for multilayered coating layer.

Eddy current methods [16] use the interaction between a magnetic field source (i.e. coil probe) and the testing material to determine the thickness of the coating. It's a comparative measure between the signal collected from sample and the reference one [17]. However, this method can be used only on conductive materials and sensitivity decreases with depth depending on the conductivity and permeability of the substrate. Ultrasound testing, which can be used to estimate the paint thickness on nonmetal substrates, is based on the control of the velocity of ultrasonic waves in the coating layer [18].

Terahertz methods measure the time delay of a terahertz waveform using different analyzing techniques such as terahertz imaging [19], terahertz sensor [20] or time-domain spectroscopy [21], but they require the knowledge of the refractive index of each layer of the sample for calculating the coating thickness.

The choice among these measurement methods depends on the coating thickness, the cost of instrumentation and the accuracy required.

The infrared thermography technique is an interesting alternative nondestructive evaluation method. The test material is excited by a flow of heat, resulting in a change in local thermal conditions. The thermal variations of the material to this excitation is captured by a thermal infrared camera. The acquired thermal response depends on different parameters of the material such as thermal conductivity, diffusivity, emissivity, and specific heat as well as the excitation used at the input [22]. More specifically, the above properties manifest themselves in the thermal response depending upon different factors including the coating heterogeneities [23]. Infrared thermography based measurement presents several benefits: remote sensing, two-dimensional data acquisition, rapid response, non-contact, high resolution, large temperature range, post-processing versatility and portability [24].

The well established thermographic technique is the pulsed technique, although, it has only been used for the evaluation of thermal barrier coating thickness [25, 26, 27]. To the knowledge of the authors this technique has been never used for the evaluation of thickness for metal/metal configuration.

The aim of this paper is to propose a specific thermographic procedure based on the "long pulse" thermographic approach for the measurement of the tungsten carbide coating thickness.

Moreover, the authors have tested the application of the well known pulsed thermography tecnique in analyzing the thickness of WC-Co-Cr coatings on steel substrates and its potential and limits have been highlighted. A comparison has been made with the performance of the traditional flash excitation technique and the long pulse excitation one. More satisfactory results have been obtained by applying the thermographic "long pulse" technique, as the parameters extracted from acquired thermal responses have the ability of identifying the different coating thicknesses investigated. A calibration has been performed to evaluate the thickness of the coating and a prediction model has been proposed.

2. Materials And Methods

2.1. Theoretical Remarks

The pulsed Infrared thermography protocol consists of pulse heating the specimen and recording the temperature decay with an infrared camera. The short thermal stimulation pulse has a duration of few milliseconds. According to thermal wave theory, the pulse heating of a specimen corresponds to the simultaneous launching into the specimen of thermal waves of various amplitudes and frequencies, in a transient mode. The reflected thermal waves, depending on thermal–physical properties of the investigated material, come back on the specimen surface where the resulting oscillating temperature field can be remotely detected through its thermal infrared emission.

The pulsed thermographic approach is based on the following equations:

$$T(L,t) = \frac{W}{e_c\sqrt{\pi t}}\left(1 + 2\sum_{n=1}^{+\infty}(-\Gamma)\, e^{-\frac{n^2L^2}{\alpha_c t}}\right) \tag{1}$$

$$e_{app}(L,t) = \frac{1}{T(L,t)\sqrt{t}} \tag{2}$$

where L is the coating thickness (m), t the time (s), e_c the coating effusivity (W $s^{1/2}$ m^{-2} K^{-1}), W the absorbed energy density (J m^{-2}), *Γ* the reflection coefficient (the ratio

$\frac{e_{app}(coating)-e_{app}(substrate)}{e_{app}(coating)+e_{app}(substrate)}$) and α_c the coating diffusivity (m^2 s^{-1}). T(L, t) is the surface temperature of a coating layer of thickness L deposited onto a semi-infinite body, heated by a Dirac pulse and not subjected to heat exchange with the environment [29]. The function e_{app}(L, t) is hereafter referred to as the apparent effusivity [29]. Eq. (3) shows how a thickness variation ΔL, being all the other parameters untouched, results in a dilation or compression of the time axis according to the scale factor $a = 1/(1 + \Delta L/L)^2$.

$$e_{app}(L + \Delta L, t) = e_{app}(L, at) \tag{3}$$

For the sake of clarity, in the following discussion the log–log representation will be adopted. As shown in Eq. (4), where the log operator indicates the natural logarithm, in this representation the effect of ΔL is a simple translation along the log (t) axis.

$$log\big(e_{app}(L + \Delta L, \log(t))\big) = log\left(e_{app}(L, \log(a) + \log(t))\right) \tag{4}$$

The effect of ΔL does not change the monotonic nature of e_{app} [26].

The second thermographic approach, that is the “long pulse” Infrared thermography, consists of a heating of the specimen using a thermal stimulation for some seconds. It must be distinguish between “long pulse” thermography and step heating thermography. In “long pulsed” thermography, heating is applied for the selected period of time and then thermal images are collected as the test piece cools down. In step heating thermography, thermal images are collected whilst the test piece is heated up.

In this approach, the premise of heating by a Dirac pulse falls and the role that the thermo-physical properties (thermal conductivity, density, specific heat capacity) of the whole sample have in determining the capabilities of the technique in estimating the coating thickness becomes notable. The propagation of the front of heat into the test-piece is governed by the thermal properties of the entire test-piece because the long heat excitation involved both the materials constituting the sample (coating and substrate). In this regard, the thickness variation of coating has to result in a change of the cooling rate of the material and can be evaluated when the thickness of the substrate does not change.

2.2. Samples

The nine samples considered in this study are disks composed by a steel substrate with 9.75 mm thickness coated with WC 86% - Co10% - Cr 4%. The tungsten carbide has been deposited by HVOF process. The specimens have been realized by coating the basic metallic material with different thicknesses varying between 1,00E-01mm and 10,10E-01mm. In Table 1, the thicknesses of WC 86% - Co10% - Cr 4% coating are reported.

The thermophysical properties [30, 31] of the analyzed coating and the steel substrate are indicated in Table 2.

Table 1: Thicknesses of WC-Co-Cr coatings

Specimen	Thickness of WC-Co-Cr coating (mm)
TH1	1,00E-01
TH2	2,00E-01
TH3	3,00E-01
TH4	4,00E-01
TH5	6,00E-01
TH6	7,00E-01
TH7	8,70E-01
TH8	9,50E-01
TH9	10,10E-01

Table 2: Thermophysical data of WC-Co-Cr coatings and steel substrate

	Density, kg/m3	Specific heat capacity, J/(kg K)	Thermal diffusivity, $m^2/s*10^{-7}$	Thermal conductivity, W/(m K)
WC-Co-Cr coating	13640	239	89.2	29.2
Steel substrate	8055	480	39	15.1

2.3. Experimental Setup and Data Acquisition

The technique applied are the pulsed Infrared thermography and the "long pulse" Infrared thermography.

Two different setup have been realized, as shown in figure 1 and 3.

The first test bench for implementing the pulsed Infrared thermography consists of a flash source (flash lamps 1500J/s x 2) generating a pulse excitation of duration 5ms and a cooled IR camera (Flir X6540 SC) with an indium-antimonium detector and resolution of 640-512 pixel sensitive in the range of 3-5 µm with Noise equivalent temperature difference (NETD) <25mK (Figure 1). The distance between the camera and the sample is 70 cm. The lamps have been placed as proximal as possible to the sample. The camera has been used with a lens of 50mm to reach a small spatial target and hence to obtain sufficient spatial resolution.

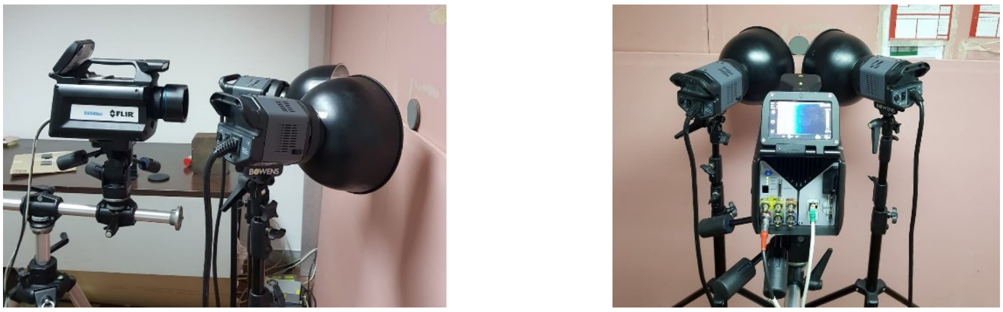

Figure **1**: Pulsed Infrared thermography setup

The use of such a high performance thermal imaging camera has made it possible to obtain a reduced window (64x80 pixels) for the observation of the phenomenon (Figure 2), achieving a mm/pixel ratio of 0.19. The windowing is necessary to reduce the acquired data and allow the use of a higher frame rate.

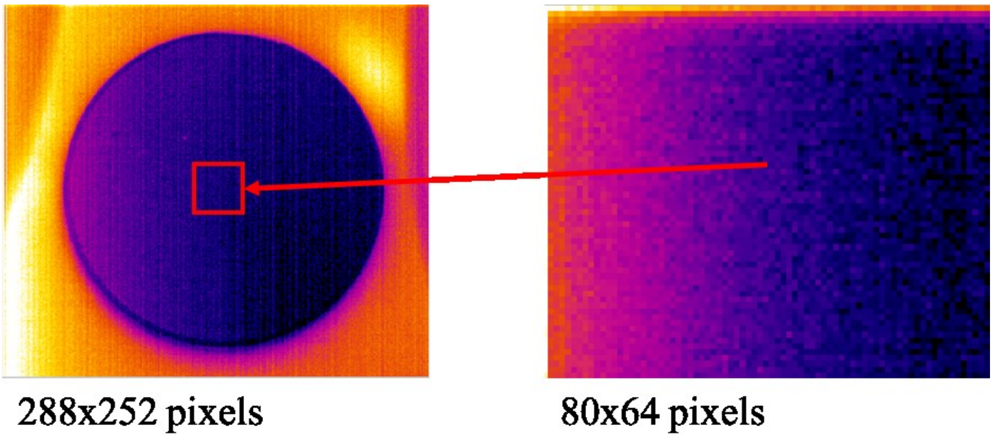

Figure 2: Full frame thermogram on the left and windowed thermogram on the right acquired with the cooled infrared camera

The temperature decay has been registered and stored as Infrared image sequences that is a 3D matrix composed by N thermograms (64x80 pixel), where x and y are the spatial coordinates, and t is the time.

Infrared image sequences, representative of the surface temperature, have been captured by the cooled camera at a frame rate of 980Hz. The observation time of the thermal cooling has been of two seconds.

The other test bench for implementing the "long pulse" Infrared thermography consists of a 1064 nm wavelength Ytterbium pulsed fiber laser generating a pulse excitation of duration 500ms, the collimated laser spot has a diameter of about 8 mm. The acquisition system of the equipment is an A655 FLIR ''long waves" (7.5–14 µm spectral range) infrared camera has been selected for its good ratio price/performance. This camera uses an uncooled micro-bolometer detector and records the infrared thermal images that have a size of 640 × 480 pixel. Its NETD equals about 30mK (Figure 3). The distance between the camera and the sample is 100cm. The laser source has been placed at a distance of 15cm from the sample and the laser beam strikes the sample perpendicularly. The camera has been used with a lens of 13.1mm to reach a spatial resolution of 0.37 mm/pixel.

Figure 3: “Long pulse” Infrared thermography setup

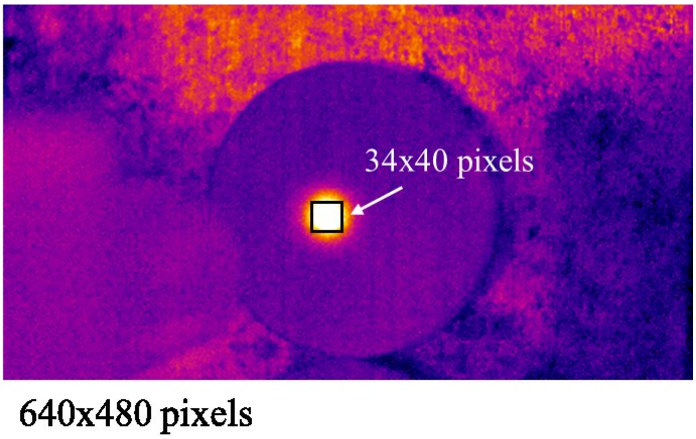

Figure 4: Selected area inside the thermogram acquired with the uncooled infrared camera

Though the used camera allow to reduce the window of observation, it has been and forced to acquire the thermal sequences at a frame rate of 50Hz, avoiding the windowing (Figure 4). The aim has been to acquire at the most slow frame rate. In Figure 4, it is also marked the little area in which the phenomenon is studied.

In this case, infrared image sequences have been acquired five times for each sample, five repetitions of the measure operation under identical condition have been carried out. The observation time of the thermal transient has been of 5 seconds.

In the wavelength intervals in which both the infrared cameras work, the spectral emissivity of the samples can be considered constant.

2.4. Data Processing

2.4.1. Apparent thermal effusivity method based on pulsed thermography

The apparent thermal effusivity algorithm, based on the above theoretical remarks, has been applied to the thermal sequences obtained by implementing the pulsed thermographic technique on all the nine samples. The thermal sequences are those acquired for each thickness of the coating.

A pre-processing procedure has been implemented before the application of the effusivity algorithm. The steps of this procedure can be summarized as follows:

- Importing of the thermographic sequence (3D matrix) in Matlab ®;

- Subtracting of the average of the first ten cold frames to the whole sequence to obtain the ΔT values over time;

- Adding an offset ΔT value to avoid ΔT values close to zero; this step is applied pixel by pixel to each temperature decay curve and allows to avoid negative values in the logarithmic scale;

The mean temperature decay trend observed for the first 700 frames of the cooling stage are plotted in Figure 5. The choice of the frame number is due to the certainty that in this time interval the thermal cooling phenomenon can be considered terminated. The trends refer to each one of the nine different thickness of the coating. Each trend represents the average of the temperature behavior of the surface in the windowed area (80x64 pixels).

The apparent effusivity profiles extracted for the nine thickness are plotted in Figure 6, the influence of a thickness variation of the coating (from 1,00E-01mm to 10,10E-01 mm) on the apparent effusivity profiles is shown.

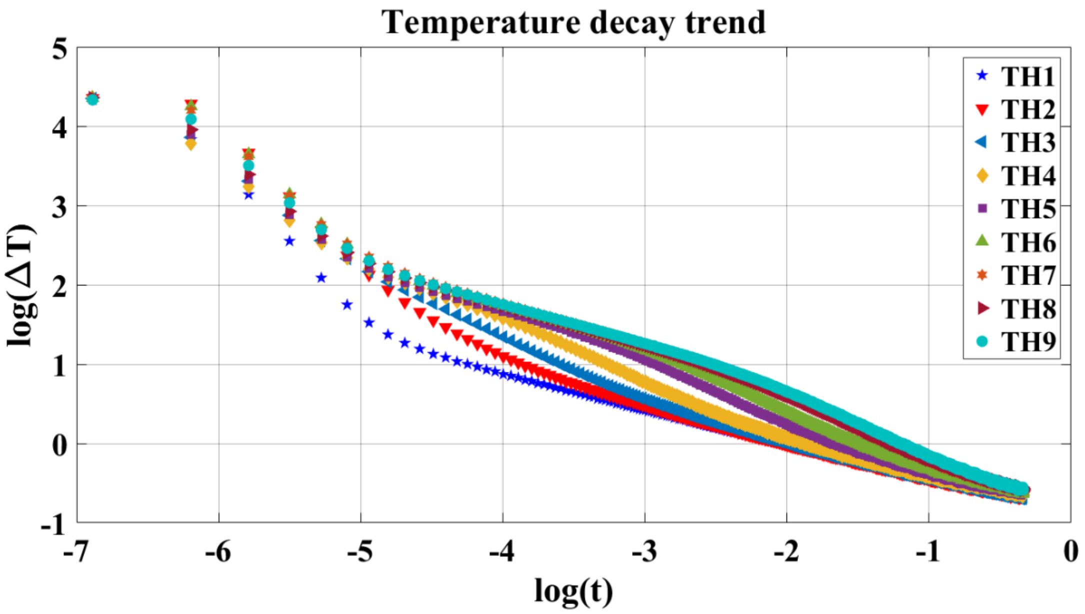

Figure 5: Mean temperature decay trends observed for the first 700 frame of the cooling stage for all the specimens

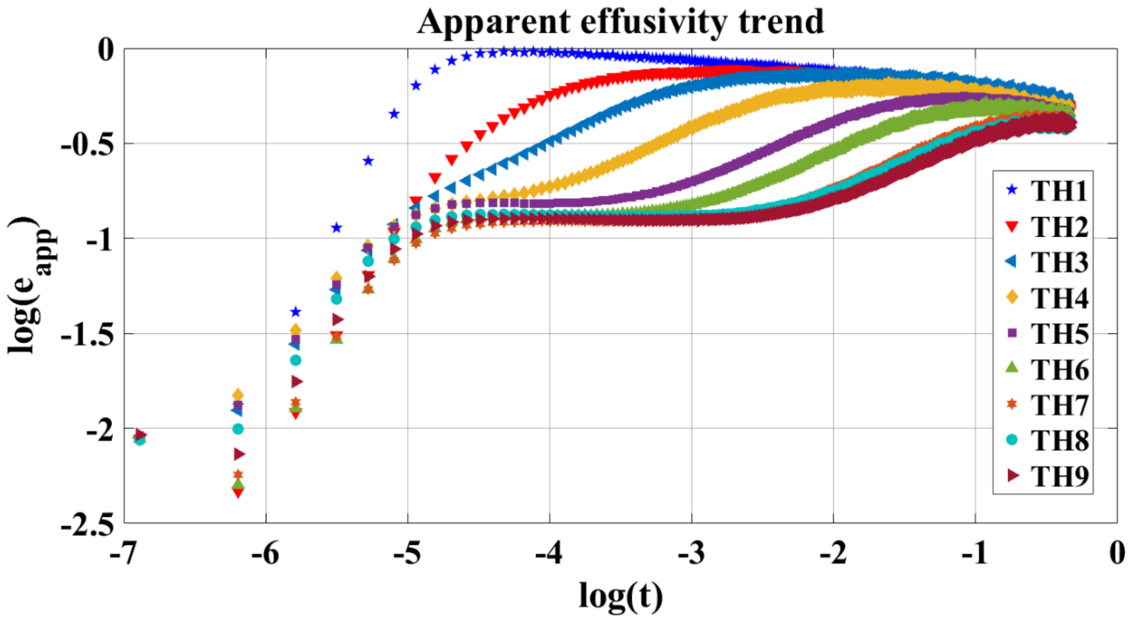

Figure 6: Influence of a thickness variation of the coating (from 1,00E-01mm to 10,10E-01mm) on the apparent effusivity profiles.

2.4.2. Procedure based on "long pulse" thermography

The thermal sequences obtained by implementing the "long pulse" thermographic technique have been pre-processed using the same procedure summarized in the previous paragraph.

In order to achieve the goal of proposing a prediction model, only seven specimens have been used as training data set, while the remaining two specimens have been used as validation data set. The validation set consists of the specimens having the coating thickness of 3,00E-01mm and that having the coating thickness of 8,70E-01mm.

The mean temperature decay trends observed on the seven sample for the first 250 frame (5 seconds) of the cooling steady are plotted using a log-log scale in Figure 7. The choice of the observation time has come by observing that the physical phenomenon of cooling was exhausted, anyway studies are in progress to indicate the best final frame for improving the procedure. The plots have been obtained choosing the pixel with the maximum temperature into an area inside the spot of the laser (34x40 pixels) on the surface of the sample, as indicated in figure 4. Each value of temperature reported in any plotted trend is the mean of the five repetition carried out, so they are represented accompanied by the error bars to show the variability of data. The error bars show the uncertainty of the mean due to random effects. [32]. The reported uncertainty provides a level of confidence of approximately 95%.

The analysis of the temperature plots relative to the samples with seven different thicknesses allows to notice that the thickness variation results in a change of the cooling rate of the material (Figure 7). On this logarithmic scale graphic, it can be notice that the central portion of the temperature decay follows a line. The value of the slope of the different lines has a correspondence with the different coating thickness.

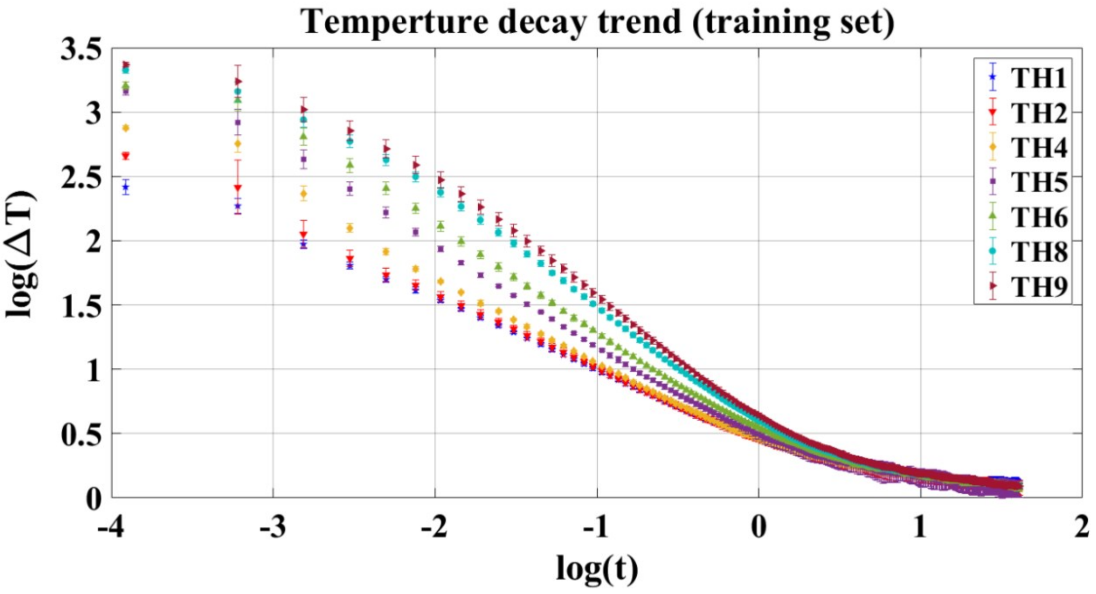

Figure 7: Mean temperature decay referred to the pixel with maximum temperature of the training samples

The evaluation of the slope has been obtained by processing the thermal sequences using in Matlab ® the commands for fitting a polynomial of degree 1 to data and for evaluating the polynomial coefficients performing an ordinary least squares calculation. The fitting has been applied to all data set acquired avoiding the previous calculation of the mean.

The least squares process solves for the slope and intercept of the best fit line. The slope obtained has been chosen as the indicator to explain the variation of thickness. In particular, the slope values decrease with the increasing of thickness. The evaluated slope values related to each thickness are reported in table 3. The 95% confidence bounds on the coefficients associated with fit are also indicated in table 3.

Table 3: Slope values related to each thickness and 95% confidence bounds on them

Specimen	Slope	Upper bound, 95% CI on mean	Lower bound, 95% CI on mean
TH1	-3,82E-01	-3,76E-01	-3,88E-01
TH2	-4,04E-01	-3,97E-01	-4,10E-01
TH4	-4,34E-01	-4,27E-01	-4,42E-01
TH5	-4,97E-01	-4,88E-01	-5,05E-01
TH6	-5,30E-01	-5,21E-01	-5,39E-01
TH8	-5,88E-01	-5,78E-01	-5,97E-01
TH9	-6,14E-01	-6,04E-01	-6,23E-01

An attempt to create possible mathematical models to describe the behavior of coating thickness depending on the slope values of the temperature cooling profiles has been made.

The models (calibration curve) have been obtained by considering the WC-Co-Cr thickness as a function of the slope values. The models have been extrapolated using data provided by the training set. Two different models seem to explain the behavior observed: a linear model and a second order polynomial model (Figure 8 and Figure 9), the goodness of fit is very high. The two models are reported with their confidence bounds and their prediction bounds. This last are larger than the confidence bounds because take into account not only the error for the estimation of the model, but also the error associated to future observations [33].

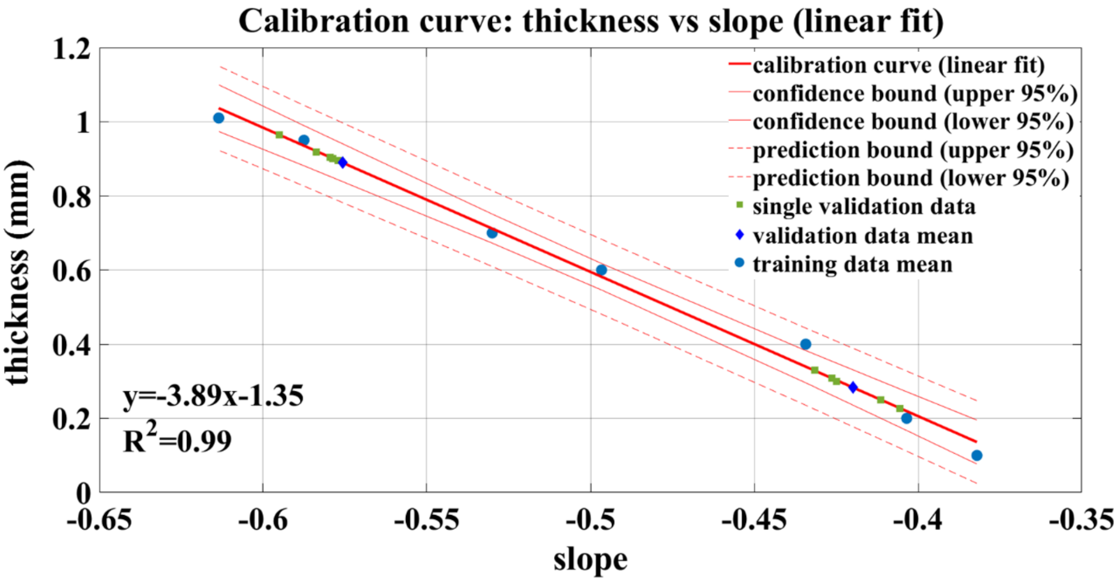

Figure 8: Data dispersion plot (thickness vs slope) with the estimated regression line (linear model), the prediction bounds (external curves) and the 95% confidence bounds

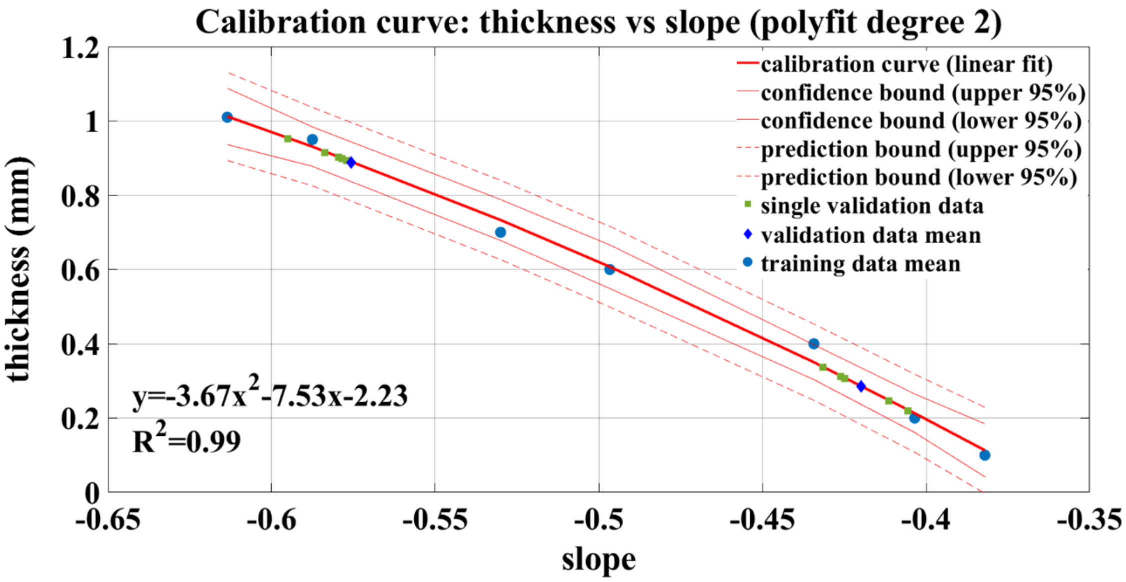

Figure 9: Data dispersion plot (thickness vs slope) with the estimated regression line (second order polynomial model), the prediction bounds (external curves) and the 95% confidence bounds

3. RESULTS AND DISCUSSION

Figure 6 shows in logarithmic representation the experimental e_{app} curves as a function of time for the considered areas (80x64pixels) corresponding to all the nine thickness, respectively. Each curve refers to the apparent effusivity value averaged on 5376 pixels. As expected, e_{app} curves do not show any minimum but only a shift caused by the different coating thickness. Anyway, a limitation has to be taken into account that is that the thermal effusivity doesn't allow to evaluate the too thin (1,00E-01mm-3,00E-01mm) coating and the too thick coating (9,50E-01mm-10,10E-01mm): in the first case, the thermal excitation is too high and the calculated effusivity is not referred to the coating, but it is an expression of both the involved materials; in the second case, two reason can contribute, the thermal excitation is too weak and the pulse doesn't reach the interface between the coating and the substrate returning the same effusivity or the reflection coefficient Γ results too small. In both cases, it is impossible resolve the difference among the different thickness. The technique remains valid for the coating whose thickness varies from 3,00E-01mm to 7,00E-010mm. In addition, another crucial issue has to be reported, this approach based on the analysis of the apparent effusivity in the time domain needs a thermographic acquisition with an elevate frame rate, of about 1000Hz, in order to capture the cooling behavior of the material. This is possible only by using a high performance and so expensive IR camera. A force point of the effusivity method is to directly calculate the value of the thickness, provided that the thermophysical properties of the coating and the substrate are known.

The real capabilities of the new proposed procedure to evaluate the thickness coating have been assessed by testing the seven metallic sample coated with a WC-Co-Cr coating. Then, the validation samples have been investigated by adopting the procedure in all its step and by using the same experimental parameters. The temperature decay trends, calculated for five repetitions, for the validation samples are reported in figure 10. The evaluated slope values related to the validation specimens are reported in table 4, accompanied with the associated confidence bounds. There is a good resolution in solving two adjacent thickness. The result of fitting is good for both the obtained models, however the error committed, in the evaluation of thickness, by choosing the linear model is a little bit greater than the error made with the polynomial model for small thickness values. The errors have been calculated using the validation data set (two samples) and compared with the nominal thickness. The difference between the mean of the measurements and the reference value (accuracy of the measurement procedure), expressed as percentage, and the precision of the models are reported in table 5. The obtained results return errors lower than 6%.

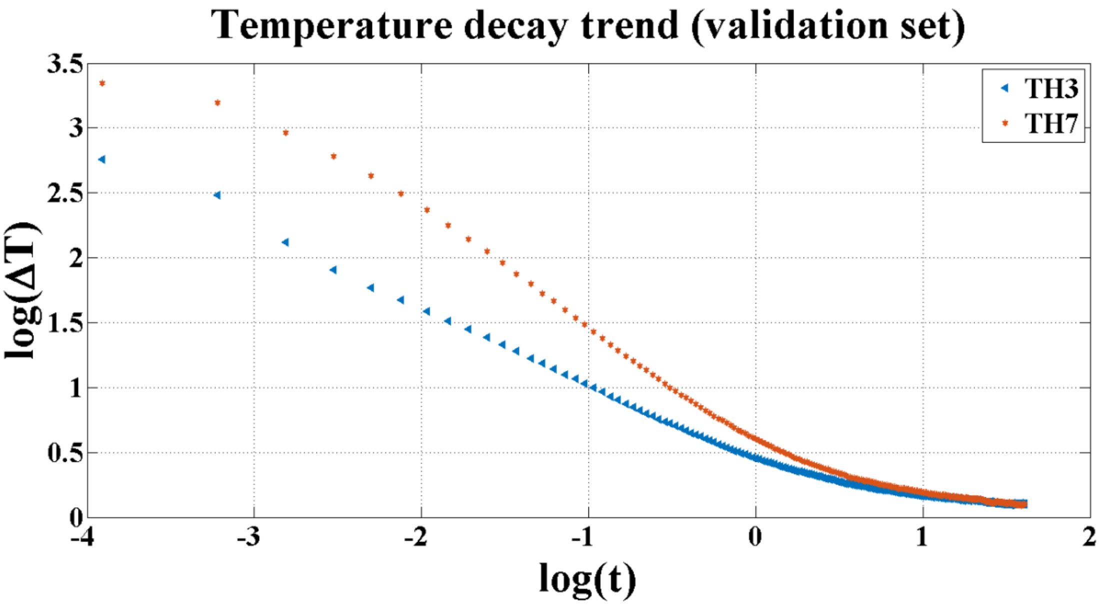

Figure 10: Mean temperature decay referred to the pixel with maximum temperature of the validation samples

Table 4: Slope values related to validation samples and 95% confidence bounds on them

Specimen	Slope	Upper bound, 95% CI on mean	Lower bound, 95% CI on mean
TH3	-4,20E-01	-4,13E-01	-4,27E-01
TH7	-5,76E-01	-5,66E-01	-5,86E-01

Table 5: Expected values of the thickness by using the models accompanied by their accuracy and precision with respect to the nominal values

Specimen	Nominal thickness (mm)	Polynomial model expectation (mm) value and 95% confidence bounds		Percentage error (%)	Linear model expectation (mm) value and 95% confidence bounds		Percentage error (%)
TH3	3,00E-01	2,87E-01	3,40E-01 2,26E-01	4,33	2,83E-01	3,32E-01 2,35E-01	5.56
TH7	8,70E-01	8,92E-01	9,50E-01 8,28E-01	2.52	8,89E-01	9,40E-01 8,39E-01	2.21

The results reported in table 4 and in table 5 have been obtained using the data of the five repetition performed in the experimental acquisition. Anyway, if it is impossible to perform the five measurements, the error that occurs, in the case in which only a measurement is performed and the same calibration model is used, has been evaluated. The percentage errors, reported in table 6, are higher if the linear model is used, while they results lower if the polynomial model is used. The accuracy worsens also for the thin thickness. It is graphically shown in figure 8 and 9.

Table 6: Expected values of the thickness by using the models accompanied by their accuracy with respect to the nominal values if single measurements are carried out

Specimen	Nominal thickness (mm)	Polynomial model expectation (mm)	Percentage error (%)	Linear model expectation (mm)	Percentage error (%)
TH3	3,00E-01	3,07E-01	2,33	3,03E-01	1,00
		2,86E-01	4,67	3,29E-01	9,67
		3,03E-01	1,00	3,08E-01	2,67
		3,66E-01	22,00	2,27E-01	24,33
		3,48E-01	16.00	2,50E-01	16,67
TH7	8,70E-01	9,51E-01	9,31	9,65E-01	10,9
		9,14E-01	5,06	9,19E-01	5.63
		9,02E-01	3,68	9,05E-01	4,02
		8,98E-01	3,22	9,01E-01	3,56
		8,94E-01	2,76	8,95E-01	2,87

This new and simple procedure based on the evaluation of the slope of the linearized temperature profile, as previously shown, needs a calibration model to be useful, but the provided results show the capability of the method in measuring the real thickness of an unknown coating. A further condition to ensure the good functioning of the developed model based on “long pulse” thermography is the thickness of the substrate whose value has to be the same for all the investigated samples.

It is noteworthy that this approach, on the contrary of the other one, doesn’t require an elevate frame rate for data acquisition, so a cheap IR camera is sufficient to implement the procedure if the accuracy requested is comparable with the obtained results. A chance to improve the accuracy and the precision of the model is given by using a more performant camera.

4. CONCLUSIONS

This paper presents a procedure to estimate WC-Co-Cr coating thickness over a metallic substrate. The used technique is the “long pulse” infrared thermography. The methodology consists in measuring the changes in slope of the line that describe the cooling behavior, in a double logarithmic scale, of the surface of the sample after a laser heating. The temperature monitoring has been carried out by using an uncooled infrared camera with basic performance.

A linear and a second degree polynomial dependency of the coating thickness with respect to the evaluated slope is demonstrated. An experimental analysis has been conducted on samples constituted by a steel substrate and WC-Co-Cr different coating thickness. The results obtained for the measured thickness return values with a precision of one hundredth of a millimeter. This achievement demonstrates the high potential of the method to estimate in a simple, fast and robust way the WC-Co-Cr coating thickness over metallic substrates. Besides, the procedure has a significant advantage over the alternative pulsed technique that doesn’t work well in the case of thin and thick coatings and very similar thermosphysical properties between coating and substrate with the aggravating factor of needing a very performing and expensive infrared camera.

REFERENCES

[1] Kamdi Z, Shipwaya PH, Voiseya KT, Sturgeon AJ (2011) Abrasive wear behavior of conventional and large-particle tungsten carbide based cermet coatings as a function of abrasive size and type. Wear 271:1264–1272–3.

[2] Wang Q, Chen ZH, Ding ZX (2009) Performance of abrasive wear ofWC-12Co coatings sprayed by HVOF. Tribol Int 42:1046–1051.

[3] Stewart DA, Shipway PH, and McCartney DG (1999) Abrasive wear behaviour of conventional and nanocomposite HVOF sprayed WC-Co coatings. Wear 225–229:789–798.

[4] L. Zhao, M. Maurer, F. Fischer, R. Dicks, E. Lugscheider, Wear 257 (1–2) (2003) 41.

[5] Bernecki, T & Science, S & Davis, J.R.. (2004). Handbook of Thermal Spray Technology. ASM International, Materials Park, OH. 14-35.

[6] J.A.R. Wesmann, N. Espallargas, Tribol. Int. 101, 301 (2016).

[7] C.C. Berndt, in: J.R.Davis (Ed.), Material Categories for Thermal Sprayed Coatings Handbook of Thermal Spray Technology,ASMInternational, Materials Park,OH, USA, 2004, pp. 142–168.

[8] A.Wank, B.Wielage, H. Pokhmurska, E. Friesen, G. Reisel, Comparison of hardmetal and hard chromiumcoatings under different tribological conditions, Surf. Coat. Technol. 201 (2006) 1975–1980.

[9] G. Bolelli, V. Cannillo, L. Lusvarghi, S. Riccò, Mechanical and tribological properties of electrolytic hard chrome and HVOF-sprayed coatings, Surf. Coat. Technol. 200 (2006) 2995–3009.

[10] A.C. Fisher-Cripps, B.R. Lawn, A. Pajares, L.Wei, Stress analysis of elastic–plastic contact damage in ceramic coatings on metal substrates, J. Am. Ceram. Soc. 79 (1996) 2619–2625.

[11] K. Holmberg, A. Laukkanen, H. Ronkainen, K.Wallin, S. Varjus, J. Koskinen, Tribological contact analysis of a rigid ball sliding on a hard coated surface Part II:

Material deformations, influence of coating thickness and Young's modulus, Surf. Coat. Technol. 200 (2006) 3810–3823.

[12] G. Stenberg, M. Boman, Thickness measurement of light elemental films, Diam. Relat. Mater. 5 (12) (1996) 1444–1449, http://dx.doi.org/10.1016/S0925-9635 (96)00563-8.

[13] Bolelli, G., Lusvarghi, L., & Barletta, M. (2009). HVOF-sprayed WC-CoCr coatings on Al alloy: Effect of the coating thickness on the tribological properties. Wear, 267(5–8), 944–953. https://doi.org/10.1016/j.wear.2008.12.066.

[14] K. Chandler, R.E. Mansford, Measurement of thickness of sprayed metal coating on steel, ICE Proc. 30 (1) (1965) 131–146, http://dx.doi.org/10.1680/ iicep.1965.9569.

[15] J.V. Koleske, Paint and Coating Testing Manual: 15th edition of the Gardner-Sward Handbook, ASTM International, Bridgeport, 1995. ISBN: 978-0-8031-7017-9.

[16] [C.V. Dodd, W.A. Simpson, Thickness measurements using eddy-current techniques, in: Proc. Spring Conference of the American Society for Nondestructive Testing, Los Angeles, 1972.

[17] PJ. Shull, Nondestructive Evaluation: Theory, Techniques, and Applications, Marcel Dekker Ed. (2002) 848.

[18] L. Ming-Xuan, W. Xiao-Min, M. Jie, Thickness measurement of a film on a substrate by low-frequency ultrasound, Chin. Phys. Lett. 21 (5) (2004) 870, http://dx.doi.org/10.1088/0256-307X/21/5/030.

[19] T. Kurabayashi, S. Yodokawa, S. Kosaka, Terahertz imaging through paint layers, in: 37th International Conference on Infrared Millimeter and Terahertz Waves, 2012, pp. 1–2. http://dx.doi.org/10.1109/IRMMW-THz.2012.6380425.

[20] K. Su, R.K. May, I.S. Gregory, P.F. Taday, Y.C. Shen, J.A. Zeitler, Terahertz sensor for non-contact thickness measurement of car paints, in: 38th International Conference on Infrared Millimeter and Terahertz Waves (IRMMW-THz), 2013, pp. 1–2. http://dx.doi.org/10.1109/IRMMW-THz.2013.6665831

[21] Y. Izutani, M. Akagi, K. Kitagishi, Measurements of paint thickness of automobiles by using THz time-domain spectroscopy, in: 37th InternationalConference

on Infrared Millimeter and Terahertz Waves (IRMMW-THz), 2012, pp. 1–2. http://dx.doi.org/10.1109/IRMMW-THz.2012.6380482.

[22] S. Bagavathiappan, B.B. Lahiri, T. Saravanan, J. Philip, T. Jayakumar, Infrared thermography for condition monitoring – a review, Infrared Phys. Technol. 60 (2003) 35–55, http://dx.doi.org/10.1016/j.infrared.2013.03.006.

[23] Mezghani, S., Perrin, E., Vrabie, V., Bodnar, J. L., Marthe, J., & Cauwe, B. (2016). Evaluation of paint coating thickness variations based on pulsed Infrared thermography laser technique. Infrared Physics and Technology, 76, 393–401. https://doi.org/10.1016/j.infrared.2016.03.018.

[24] E. D'Accardi, D. Palumbo, R. Tamborrino, U. Galietti, Quantitative analysis of thermographic data through different algorithms, Procedia Structural Integrity,Volume 8, 2018, Pages 354-367, ISSN 2452-3216, https://doi.org/10.1016/j.prostr.2017.12.036.

[25] Tang Q., Liu J., Dai J., Yu Z., "Theoretical and experimental study on thermal barrier coating (TBC) uneven thickness detection using pulsed infrared thermography technology", Applied Thermal Engineering, 114(5) 770-775 (2017).

[26] Marinetti S., Robba D., Cernuschi F., Bison P.G., Grinzato E., "Thermographic inspection of TBC coated gas turbine blades: Discrimination between coating over-thicknesses and adhesion defects," Infrared Physics & Technology, 49 (3) 281-285 (2007).

[27] D. Palumbo, R. Tamborrino, U. Galietti, "Coating defect evaluation based on stimulated thermography," Proc. SPIE 10214, Thermosense: Thermal Infrared Applications XXXIX, 102140X (5 May 2017);

[28] X. Maldague (Technical Ed.), P. O. Moore (Ed.), Nondestructive Testing Handbook, Infrared and Thermal Testing, vol. 3, ASNT, Columbus (USA), 2001, pp. 62.

[29] D.L. Balageas, J.C. Krapez, P. Cielo, Pulsed photothermal modeling of layered materials, Journal of Applied Physics 59 (2) (1986) 348–357.

[30] Thiele, S., Sempf, K., Jaenicke-Roessler, K., Berger, L. M., & Spatzier, J. (2011). Thermophysical and microstructural studies on thermally sprayed tungsten carbide-

cobalt coatings. In Journal of Thermal Spray Technology (Vol. 20, pp. 358–365). https://doi.org/10.1007/s11666-010-9558-0.

[31] Ibarra-Castanedo C., Bendada A. and Maldague X. (2005). “Image and signal processing techniques in pulsed thermography”. GESTS Int'l Trans. Computer Science and Engr., 22(1): 89-100.

[32] JCGM 100:2008 (E), Guide to the expression of uncertainty in measurement

[33] D. C. Montgomery and G. C. Runger (2011) Applied Statistics and Probability for Engineers, 5th edition (Wiley, New York).

E Automatic Defect Detection from thermographic Non Destructive Testing

1. Introduction

In recent years, thermography has appeared particularly attractive among the nondestructive testing (NDT) methods for the detection of defects in materials. It offers the advantages of low cost, easy operation, high speed, and wide area coverage.

The most widely used form of thermographic NDT is the pulsed thermography in which the surface of a tested part is heated with a brief pulse of light usually from a high power source. The time-dependent surface temperature response is captured as a series of thermal images by an infrared camera. [1]

The temperature contrast between the defective and non-defective regions enables defect detection based on thermographic data. However, thermal images usually involve significant measurement noise and non-uniform backgrounds caused by uneven heating. [2]. Hence, different types of thermographic image analysis methods have been proposed for signal enhancement [3-8].

Along with pulsed thermography, step heating thermography has received attention. It is implemented by applying a thermal stimulation to a surface for more than few milliseconds [9].Many workers in the field are aware that this long pulse excitation technique can be effective for some favorable applications [10 -12].

Balageas et al. and Palumbo et al. have shown how the processing tools, commonly used for pulse-heating, can be applied to step-heating, less popular than pulse-heating [8, 13].

2. Experimental Setup

In this paper, the authors introduce a new processing technique of the thermographic data for the detection of possible defects. The technique includes a series of enhancements of the linear fit of the log-log cooling time history of the specimen surface temperature. Basically, the algorithm is directly applied to the thermographic images indicating the temperature trend of each pixel. The slope (m) of the linear fit of the log-log of the surface temperature time history is going to be used as a primary indicator of the location and size of the defects. The idea inspiring this work is to significantly enhance the fit, adopting optimization techniques to better utilize the spatial information coming from thermographic data. Besides, additional rigorous parameters will be proposed to accurately evaluate a defect.

The study will be conducted using experimental data from a campaign of measurements carried out on thermal barrier coatings (TBCs). The defect on which it has been focused the attention is the debonding between the coating and the substrate which is one of the common structural defects of TBCs [14].

The specimens used are discs with metallic bondcoat and a ceramic topcoat which is Yttria Stabilized Zirconia (YSZ), deposited by High Velocity Oxy Fuel (HVOF) technique. They have been realized with an adhesion defect (Figure 1).

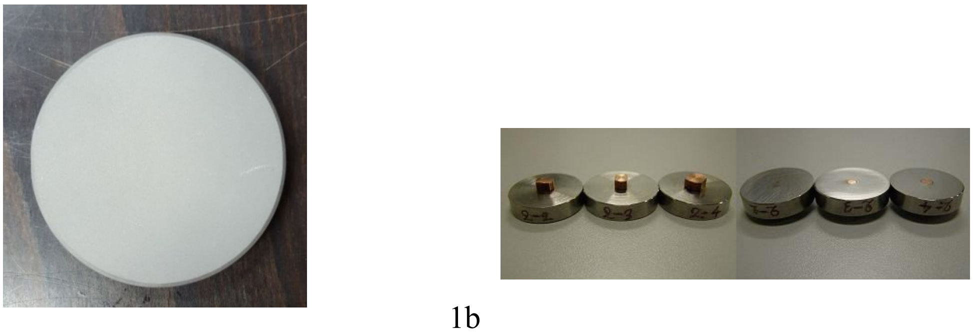

1b

1a

Figure 1: 1a. Picture of one of the reference-coated samples; 1b. Picture of a sample during the phase for producing the adhesion defect

A 1064 nm wavelength Ytterbium pulsed fiber laser generating pulse of 500ms for implementing the stepped thermography. The energy and the diameter of the heating shots were fixed equal to 30W and 8mm, respectively. A cooled IR camera with an Indium-Antimonium detector and resolution of 640-512 pixel (Flir X6540 SC) sensitive in the range of 3-5 µm was used to monitor the temperature transient of the sample surface at frame rates of 500 Hz. The experimental set up is shown in Figure .

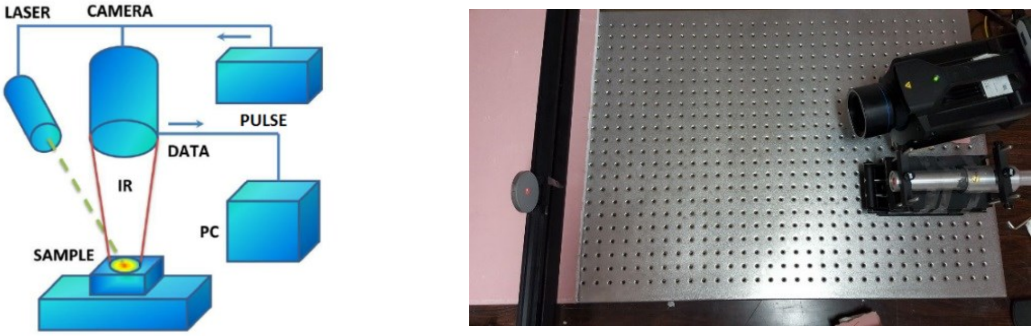

Figure 2: Experimental set up for thermographic data acquisition [15]

3. Proposed Algorithm Description And Preliminary Results

In order to describe and exploit the features of the proposed post-processing algorithm, three different samples are tested. Three identical primary specimens are characterized by a circular defect (emulating a partial detachment of the thermal coating) of varying diameter: 2mm (specimen A), 3mm (specimen D), and 5mm (specimen E).

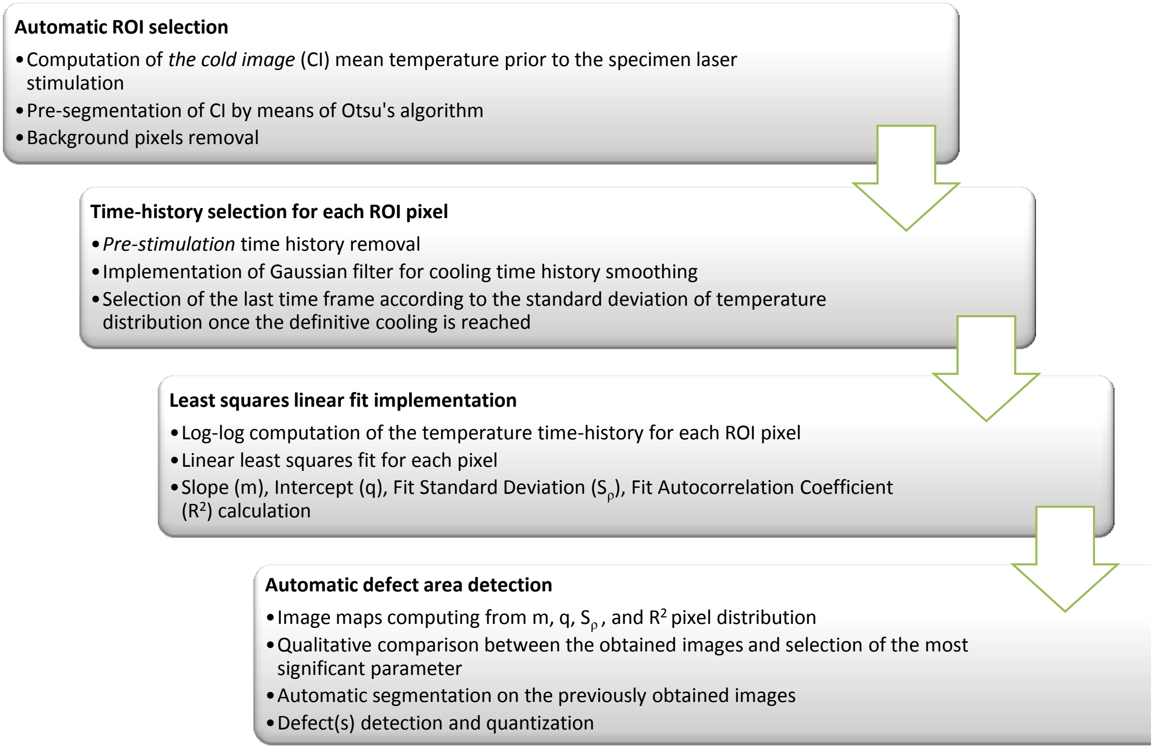

Automatic ROI selection

- Computation of *the cold image* (CI) mean temperature prior to the specimen laser stimulation
- Pre-segmentation of CI by means of Otsu's algorithm
- Background pixels removal

Time-history selection for each ROI pixel

- *Pre-stimulation* time history removal
- Implementation of Gaussian filter for cooling time history smoothing
- Selection of the last time frame according to the standard deviation of temperature distribution once the definitive cooling is reached

Least squares linear fit implementation

- Log-log computation of the temperature time-history for each ROI pixel
- Linear least squares fit for each pixel
- Slope (m), Intercept (q), Fit Standard Deviation (S_ρ), Fit Autocorrelation Coefficient (R^2) calculation

Automatic defect area detection

- Image maps computing from m, q, S_ρ, and R^2 pixel distribution
- Qualitative comparison between the obtained images and selection of the most significant parameter
- Automatic segmentation on the previously obtained images
- Defect(s) detection and quantization

Figure 3 Flowchart of the proposed algorithm

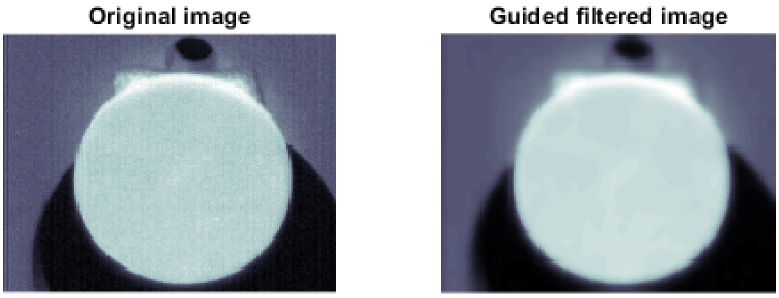

Figure 4 Original and filtered images of pre-stimulation mean temperature, for specimen A

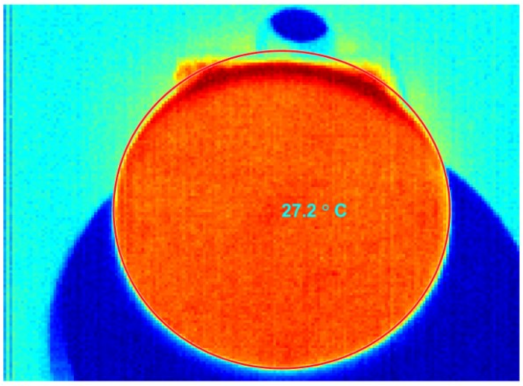

Figure 5 Pre-stimulation mean temperature image pre-segmentation for ROI selection based on region mean temperature selection, for specimen A

Figure illustrates the flowchart of the proposed algorithm. It consists of a series of enhancements of the linear fit of the cooling curve (in log-log scale). The most significant improvements introduced allow, in first instance, for an automatic detection of the ROI region (i.e. the region representing the effective specimen to analyze, with the chance of removing the background region). Such a distinction is based on the specimen mean temperature prior to the laser excitation, allowing for the computation of the so called *Cold Image* (CI).

The computation of the CI is performed by means an adaptive Otsu's segmentation, [16], performed on the image relative to the mean temperature distribution prior to the thermal excitation.

An additional improvement to mention, is the automatic selection of the effective cooling time history of each pixel (within the ROI region). An example is provided by Figure .

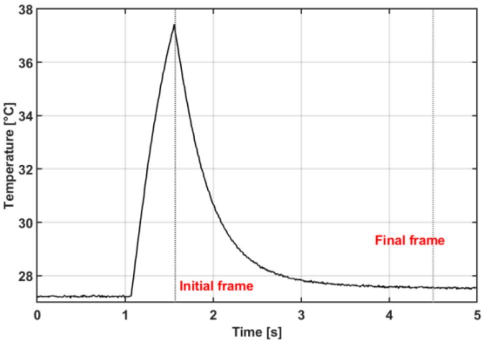

Figure 6 Selection initial and final frames for an arbitrary pixel (specimen A)

The significant parameters deriving from the linear least squares fit performed on each pixel are the slope (m) and the fit autocorrelation coefficient (R^2). These parameters, as pointed out in [8], provide qualitative information about any possible defect location and size. Additionally, the authors of this paper introduce the fit standard deviation (S_ρ) and fit intercept (q). The obtained results have been compared with those deriving from the *Thermographic Signal Reconstruction* algorithm, TSR [3-5]. Figure and Figure show the TSR coefficient maps and the linear fit parameter (as proposed in this paper) for specimen A. Figure and Figure are relative to specimen D, while Figure and refer to specimen E.

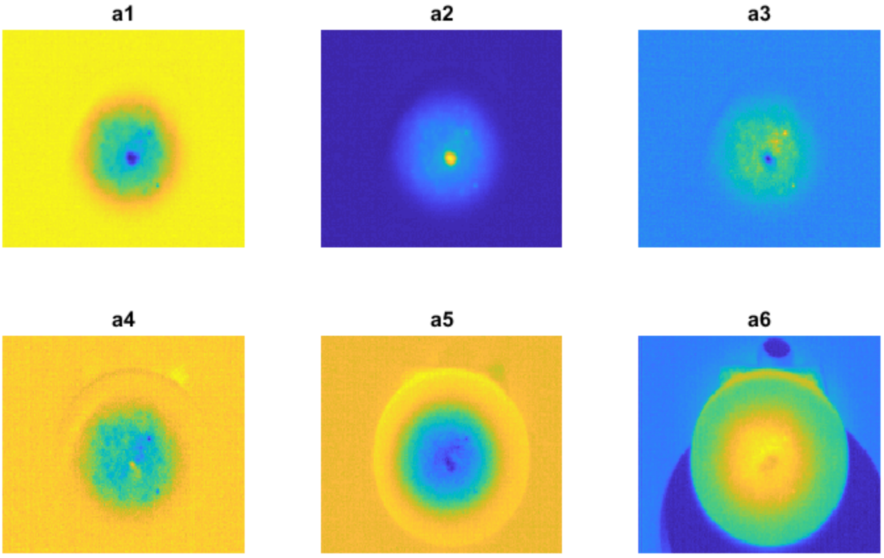

Figure 7 Coefficient maps from TRS algorithm, specimen A

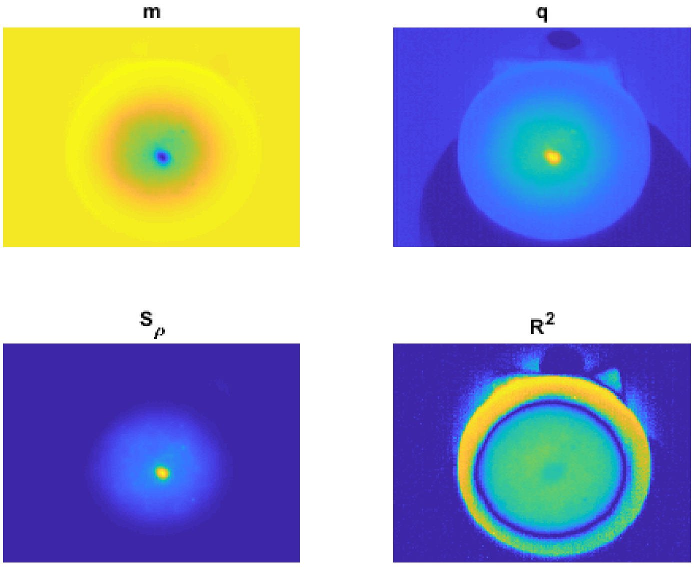

Figure 8 Linear fit coefficients, according to the proposed technique, for specimen A

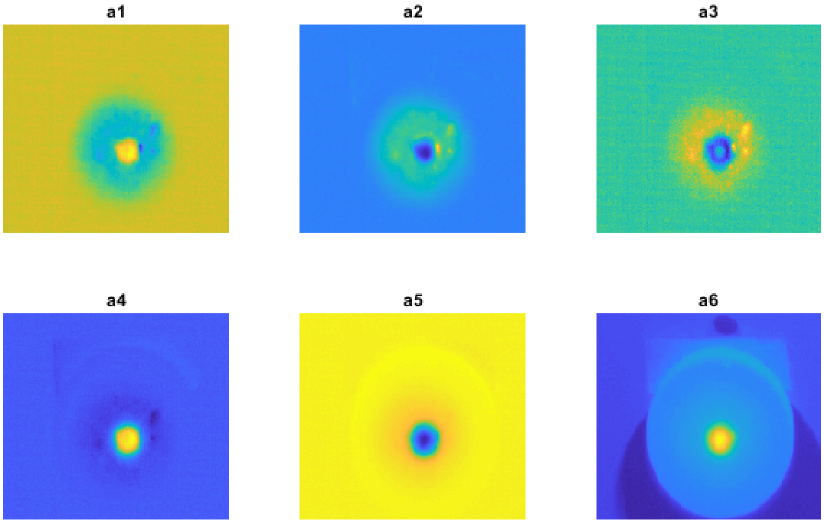

Figure 9 Coefficient maps from TRS algorithm, specimen D

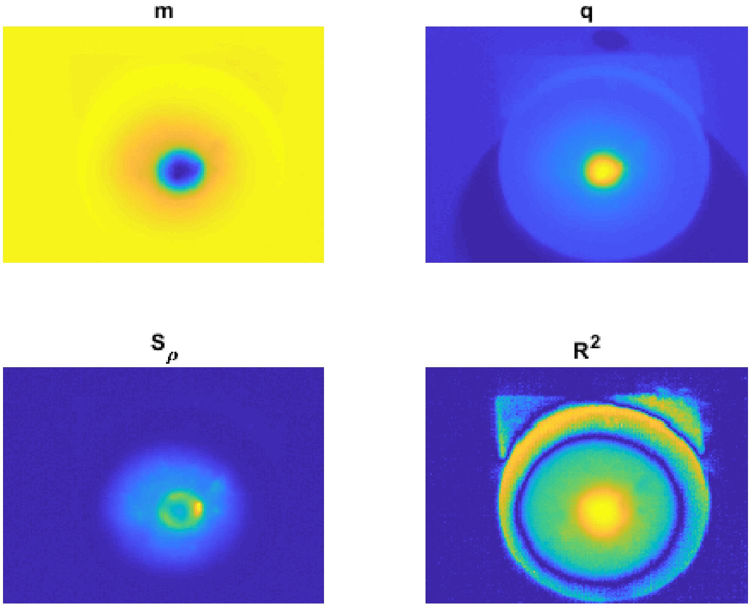

Figure 10 Linear fit coefficients, according to the proposed technique, for specimen D

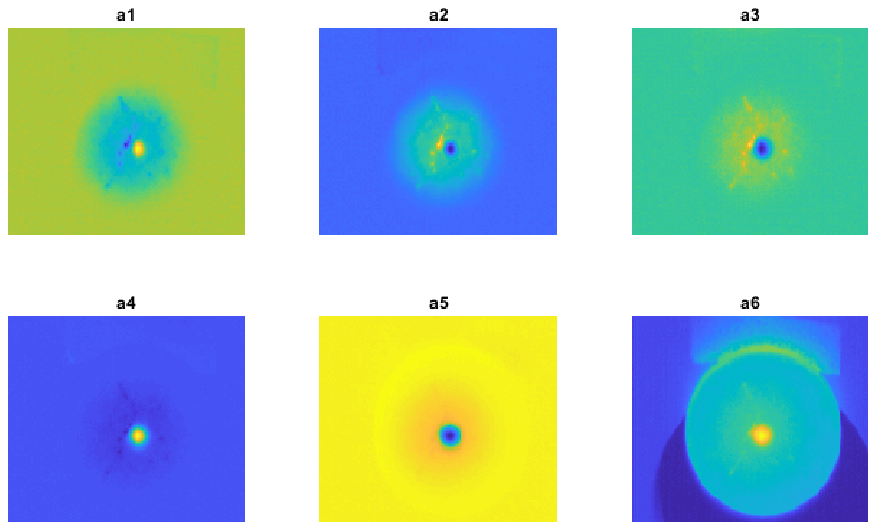

Figure 11 Coefficient maps from TRS algorithm, specimen E

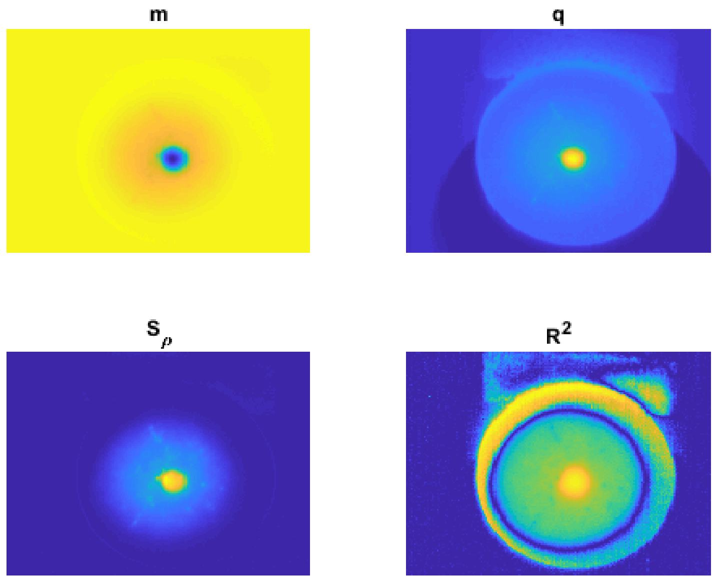

Figure 12 Linear fit coefficients, according to the proposed technique, for specimen E

The outcome of the algorithm consists of a series of images indicating the amount of the fit parameters for each pixel (see Figure , Figure and Figure). The fit slope and autocorrelation coefficients provide a qualitative indication of defect location and size (tough R^2 does not perform properly for specimen A). Additionally, images for fit standard deviation and intercept have been provided.

A further segmentation is, then, implemented on the achieved images. This step allows for the detection of the damaged pixels and, therefore, a quantitative defect characterization is possible.

References

[1] Vavilov VP, Burleigh DD. Review of pulsed thermal NDT: physical principles, theory and data processing. NDTE Int 2015;73:28–52

[2] Kaiyi Zheng, Yu-Sung, Chang YuanYao. Defect detection in CFRP structures using pulsed thermographic data enhanced by penalized least squares methods. Composite Part B: Engineering 2015; 79: 351-358

[3] S.M. Shepard. Advances in pulsed thermography Proceedings of the SPIE (2001), pp. 511-515,

[4] S.M. Shepard, J.R. Lhota, B.A. Rubadeux, T. Ahmed, D. Wang. Enhancement and reconstruction of thermographic NDT data Proceedings of the SPIE (2002), pp. 531-535

[5] X. Maldague, F. Galmiche, A. Ziadi Advances in pulsed phase thermography Infrared Phys Technol, 43 (2002), pp. 175-181

[6]- C. Ibarra-Castanedo, X. Maldague Pulsed phase thermography reviewed Quant InfraRed Thermogr J, 1 (2004), pp. 47-70

[7] N. Rajic, Principal component thermography for flaw contrast enhancement and flaw depth characterisation in composite structures Compos Struct, 58 (2002), pp. 521-528

[8] Palumbo D., Galietti U., “Damage Investigation in Composite Materials by Means of New Thermal Data Processing Procedures,” Strain 52 276-285(2016)

[9] Roche J–M, Balageas D. Common tools for quantitative pulse and step-heating thermography-Parts l and ll. QIRT Conference, Bordeaux, France, 1-28; 2014

[10] Valivov VP. Infrared NDT of bonded structures. Brit J Ndt 1981:175–83.

[11] Vavilov VP, Taylor R. Theoretical and practical aspects of the thermal nondestructive testing of bonded structures. Research Techniques in Nondestructive testing, 5. London: Academic Press; 1982. p. 239–79.

[12] Almond DP, Delpech P, Peng Wang, Behesty M. Quantitative determination of impact damage and other defects in carbon fiber composites by transient thermography. Proc SPIE 1996;2944:256–64

[13] D. Balageas, J.M. Roche. Common tools for quantitative pulse and step-heating thermography - Part I: theoretical basis. The 12th International Conference on Quantitative InfraRed Thermography (QIRT 2014), Jul 2014, BORDEAUX, France.

[14] Davide Palumbo, Rosanna Tamborrino, Umberto Galietti, "Coating defect evaluation based on stimulated thermography", Proc. SPIE 10214, Thermosense: Thermal Infrared Applications XXXIX, 102140X (5 May 2017)

[15] Strzałkowski K., Streza M., Pawlak M.,” Lock-in thermography versus PPE calorimetry for accurate measurements of thermophysical properties of solid samples:A comparative study,” Measurement, 64 64–70

[16] Otsu, N., "A Threshold Selection Method from Gray-Level Histograms," IEEE Transactions on Systems, Man, and Cybernetics, Vol. 9, No. 1, 1979, pp. 62-66